Designing the Four Rod Crab Cavity for the High-Luminosity LHC upgrade.

Hall, Ben (ULAN)

01 September 2012

The EuCARD-2 Enhanced European Coordination for Accelerator Research & Development project is co-funded by the partners and the European Commission under Capacities 7th Framework Programme, Grant Agreement 312453.

This work is part of EuCARD-2 Work Package **1: Management and Communication (MANCOM)**.

Designing the Four Rod Crab Cavity for the High-Luminosity LHC upgrade.

Ben Hall

This thesis is submitted in partial fulfilment of the requirements
for the degree of Doctor of Philosophy

September 2012

Abstract

This thesis presents the design for a novel compact crab cavity for the HL-LHC upgrade at CERN, Geneva. The LHC requires 400MHz RF cavities that can provide up to 10MV transverse gradient across two to three cavities with suitably low surface fields for continual operation. As a result, a cavity design was required that would be optimised to these new parameters. From initial design studies based on Jefferson Laboratory's CEBAF deflector, extensive optimization was carried out to design a superconducting crab cavity, dubbed the Four Rod Crab Cavity (4RCC). The design underwent several iterations throughout the course of the project due to changing requirements from CERN, particularly space requirements inside the LHC. In addition, it was decided that a focus on field flatness was required. An aluminium prototype was then constructed from the finalised and computer-simulated design to confirm the designed field flatness. Additional computer simulation studies using CST were performed to ensure that multipacting and higher order modes were at tolerable levels. Design considerations were made to ensure a niobium prototype could be constructed for cold testing, the results of which are presented along with discussion of future plans for continuing to further the design of the cavity.

Acknowledgements

I would like to acknowledge the help of and thank the following for their work, help and support throughout my PhD: my supervisor Graeme Burt, Praveen Ambattu, Rama Calaga, Jean Delayen, Amos Dexter, Philippe Goudket, Erk Jensen, and Chris Lingwood.

I would also like to thank my parents, Chris and Liz Hall, as well as my girlfriend Heather Thornton, for their help and support.

Contents

List of Figures

List of Tables

Nomenclature

Cavity Properties

f Frequency

ω Angular frequency

k Wave number

c Speed of light

d Cavity length

R_0 Cavity radius

λ Wavelength

$\hat{\mathbf{z}}$ Direction of the beam in Cartesian coordinates

$\hat{x}$ Direction of deflection within the cavity

$\hat{y}$ Direction normal to beam deflection

$\mathbf{V}$ Voltage

$\mathbf{V}_\perp$ General transverse voltage perpendicular to the $\hat{\hat{z}}$ direction

$\mathbf{V}_t$ Transverse voltage

$\mathbf{V}_z$ Longitudinal voltage in the $\hat{\mathbf{z}}$direction

$\mathbf{V}_x$ Transverse voltage in the $\hat{x}$direction

$\mathbf{V}_y$ Transverse voltage in the $\hat{y}$direction

v Scalar velocity of the bunch

$\mathbf{v}$ Vector velocity of the bunch

q Charge on an electron

x X coordinate

y Y coordinate

ρ Radial coordinate $\left(\sqrt{x^2+y^2}\right)$

θ Angular coordinate

Electromagnetic Properties

$\mathbf{E}$ Electric Field

$\mathbf{B}$ Magnetic Field

$\mathbf{A}$ Magnetic vector potential

ϵ_0 Permittivity of free-space

Mathematical definitions

ζ_{11} First root of the first J Bessel function

R Geometric loss factor

Φ Piwinski factor

θ_c Crossing angle

σ_z Longitudinal bunch size

σ_t Transverse bunch size *CST Microwave studio* *CST Particle studio*

$< SEY >$average sey for multipacting

Chapter 1

Introduction

1.1 The LHC

The Large Hadron Collider (LHC) is the world's largest circular collider, at 27 Km, located on the border of Switzerland and France. The LHC beams consist of 2808 bunches of $1.15 \cdot 10^{11}$ protons, each bunch is 7.55 cm long, circulating at 7 TeV. This corresponds to a beam current of 0.58 A with the bunches 25 ns apart travelling at 0.999999991 c. Each beam when fully ramped up contains $\sim$ 360 MJ of energy. This allows the LHC to have the highest luminosity in the world and the largest integrated luminosity of any particle accelerator ever built [1, 2].

The LHC generates its bunches through a complex chain that accelerates protons from freshly-ionised hydrogen atoms to the multiple TeV of the main LHC synchrotron. The protons begin life at the LINAC-2 proton source, where they are accelerated to 50 MeV. They are passed to the Proton Synchrotron Booster (PS Booster), where they are accelerated to 1.4 GeV. This then goes into the Proton Synchrotron, where they are accelerated to 25 GeV. They are then fed into the Super Proton Synchrotron (SPS), where it is accelerated to 450 GeV. The bunches are then split into the two contra-rotating rings of the LHC, where they are further accelerated to their maximum energy. This is currently 3.5 TeV, but this number is expected to reach its design specification of 7 TeV after the

2013 shut-down [3].

The main synchrotron ring of the LHC includes 12,302 super-conducting dipole magnets that are approximately 15 m long and nominally operate at 8.36 Tesla and at 1.9 K. These dipoles bend the beam around the 27 km ring. Numerous quadrupole and sextupole magnets focus the beam as it circulates. The acceleration of each beam is provided by eight 400 MHz super-conducting cavities, each delivering 2 Mv[4].

The LHC aims to understand the fundamental physics of the universe. Its recent discovery of a Higgs-like particle is one step in its journey [5]. The LHC is also looking to study the following - the existence of super symmetry (a possible extension to the Standard Model [6]), Dark Matter (which appears to account for a large portion of the universe's mass-energy [7]) and some aspects of String Theory [8]. The experiments that will carry out this research are located at four interaction points [IP's] spread around the ring where the beams cross shown in Figure 1.1. ATLAS and CMS are two general purpose experiments. ALICE is dedicated to the study of heavy ions, and LHC-B is dedicated to the study of CP-violation and other rare phenomenon [9].

The number of collisions that have happened in the LHC is represented by the integrated luminosity. As they are trying to increase the number of collisions, the LHC is aiming to maximize this value. Luminosity is the number of particles per unit area, per unit time, times the opacity of the target, in units $\mathrm{cm}^{-2}\mathrm{s}^{-1}$. This is usually denoted in inverse femto barns per second, $\mathrm{fb}^{-1}s^{-1}$, where $\mathrm{fb}^{-1}s^{-1} = 1 \times 10^{39}\,\mathrm{cm}^{-2}\mathrm{s}^{-1}$. The integrated luminosity, with regards to time, is thus expressed in inverse femto barns, fb^{-1}.

The LHC is aiming to meet its design luminosity of $1 \cdot 10^{34}\,\mathrm{cm}^{-2}\mathrm{s}^{-1}$by the end of 2014. This will provide approximately $40\,\mathrm{fb}^{-1}$of luminosity per year. However as the experiment continues to run, the statistical significance of gaining more data begins to diminish and it starts to take several years to halve any statistical errors. Thus the LHC must be upgraded to run at a higher luminosity

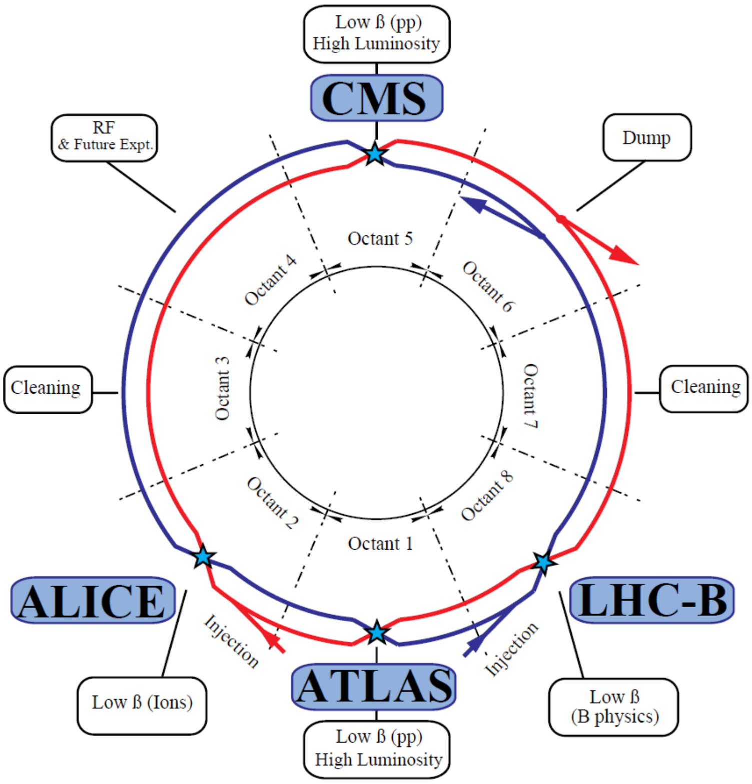

Figure 1.1: Layout of the main experiments of the LHC [9].

if it wishes to continue to provide scientific merit.

1.2 LHC Upgrades

There are three main programs of upgrade for the LHC. These are the High Luminosity (HL-LHC) upgrade, the High Energy upgrade (HE-LHC) and the Electron upgrade (LHeC). For our purposes, we will be focusing mostly on the HL-LHC upgrade, however, the other upgrades are briefly outlined below. All three of the upgrades assume that the main injector complex will be upgraded. This upgrade will begin with the construction of LINAC4, a linear accelerator that aims to provide protons of 160MeV. These will then be injected into the PS Booster [10]. This upgrade allows the space-charge limitations of the PS Booster to be overcome. The current energy of 800 MeV is not large enough to suppress the electrons desire to repel each other due to their charge. The upgrade aims to increase the energy to 1400 MeV. This can help improve the brightness and luminosity of the LHC beam [11].

The LHeC proposes to use an electron beam to collide simultaneously with the normal LHC collisions. The electron beam allows for high precision, deep inelastic scattering measurements. These will enable investigation of strong and electro-weak interactions. The LHeC may consist of either a specially-built LINAC or an additional ring inside the LHC beam line [12].

The HE-LHC is dependent on the HL-LHC upgrade, which will be described in further detail below. After the HL-LHC upgrade, the HE-LHC intends to extend the energy regime from the current 14TeV centre of mass energy to a higher energy of 33TeV. This would extend the possibilities for further experimentation into unknown areas of physics [13].

The aim of the HL-LHC upgrade is to drastically increase the luminosity of the LHC and thus the rate at which data can be acquired [14, 15].

The instantaneous luminosity is given as:

$$L = \frac{f_{rev} \cdot n_b \cdot N_1 \cdot N_2}{2\pi\sqrt{\left(\sigma_{x,1}^2 + \sigma_{x,2}^2\right) \cdot \left(\sigma_{y,1}^2 + \sigma_{y,2}^2\right)}} \tag{1.1}$$

where f_{rev} is the revolution frequency, n_b the number of bunches colliding at the Interaction Point (IP), N_1 and N_2 are the particles per bunch. $\sigma_{x,1}^2$ and $\sigma_{x,2}^2$are the horizontal beam size and $\sigma_{y,1}^2$ and $\sigma_{y,2}^2$are the vertical beam size of the two colliding beams.

This provides three main ways to increase the luminosity: increase the number of bunches, increase the number of particles in a bunch and decrease the beam size at IP. The increase in luminosity is however limited by the performance of the hardware. The LHC will primarily focus on decreasing the beam size at the IP. This will result in the β^* being reduced from 0.55 m to 0.15 m [16][17]. β^* is the value of β at the point (IP).

The position (x) and momentum (x') of a particle obey Liouville's theorem as they circulate, allowing them to oscillate around the bunch as the bunch moves around the accelerator. Liouville's theorem conserves the bunch's x and x' within a phase space area, usually an ellipse. The maximum position on the x axis is given by $\sqrt{\epsilon\beta}$, the square root of the beta function (β) and the emittance (ϵ). The emittance is the average spread of the particles in phase space and the beta function is the amplitude function that relates the emittance to the beam size. The maximum position on the x' axis is given by $\sqrt{\frac{\epsilon}{\beta}}$, as shown in Figure1.2.

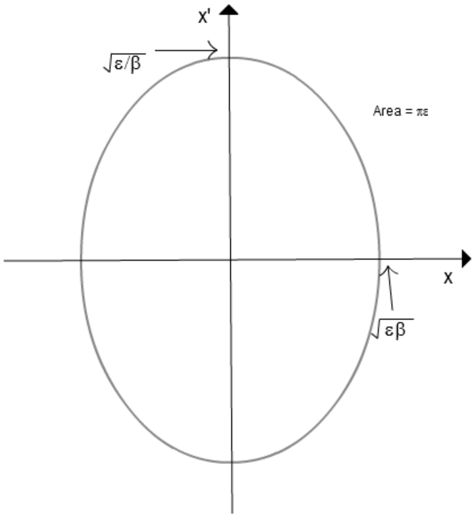

Figure 1.2: Liouville's theorem ellipse.

By decreasing β^* or increasing N_1 and N_2, instabilities within the machine will increase. The hardware can only mitigate a fixed amount of instabilities. Beam-beam interactions are also a major source of limiting instability. Here, as the number of particles within each bunch increases, the interaction between opposing beams increases. To reduce the effect of the long range beam-beam interaction, the angle at which the beams cross can be increased.

However, there is also an additional parameter to consider - the geometric loss factor (R) due to the angle at which the bunches cross.

$$R = \frac{1}{\sqrt{1+\Phi^2}} \tag{1.2}$$

Φ is the Piwinski factor calculated as [18]:

$$\Phi = \frac{\theta_c \sigma_z}{2\sigma_t} \tag{1.3}$$

Where θ_c is the crossing angle, σ_z is the longitudinal bunch size and σ_t is the transverse bunch size. The variation of the geometric loss factor is shown in Figure 1.3 as the Piwinski factor is varied.

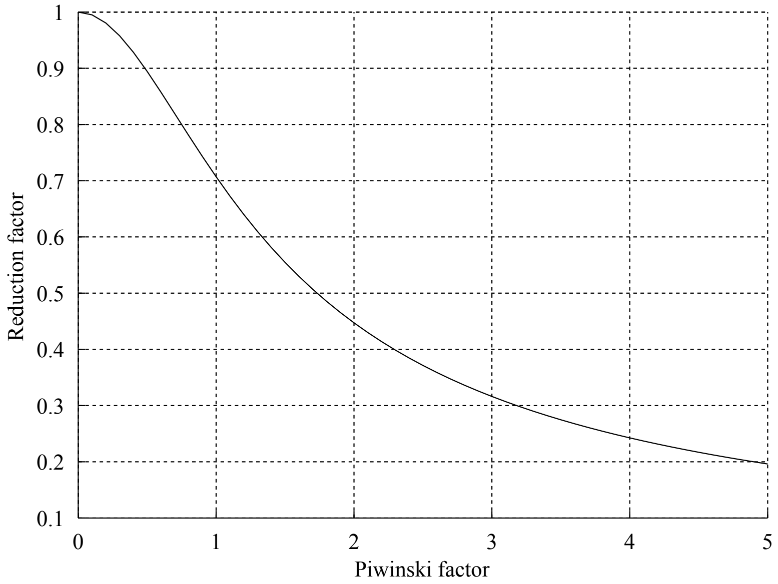

Figure 1.3: Reduction factor vs Piwinski factor.

The nominal LHC runs with a a Piwinski factor of 0.68 which corresponds to a geometric loss factor of 0.83. However during the upgrade this factor is likely to increase, possibly up to as high as 2.6, which would correspond to a geometric loss factor of 0.46. This is a significant loss in luminosity that will need to be mitigated.

To increase the beam performance, reduce the β^*, and increase the number of particles per bunch, the LHC must undergo several updates in hardware. The entire upgrade is referred to as the HL-LHC upgrade. The magnet systems will be overhauled with new separation dipoles (that provide a larger beam aperture up to 180 mm and higher magnetic fields up to 8.46 T, to allow for increased crossing angles [19]) and new inner triplets that allow for better focusing that result in a decreased β^* [20]. Numerous collimators will also be replaced due to the radiation damage they have received and to provide additional protection for the new systems [21]. To help mitigate the beam-beam effects, wire compensators may be installed near the IP [22]. As the luminosity will increase during the upgrade, the pile up caused by events is above the ability of the detector to handle currently. The detectors will have been damaged over many years of radiation bombardment and will also possibly need replacing. Thus the detectors will undergo some hardware updates to enable them to cope with the expected increased pile up and replace damaged hardware [23, 24, 25].

During operation, the collisions remove particles from the beam and the luminosity drops. However, there is a maximum number of events taking place at the IP's that the detectors can cope with, referred to as event pile up, and any events above this limit are lost. This results in the initial luminosity being higher than the experiments can cope with due to pile up, but lower than desired at the end of the run as the beam is used up. The experimentalists desire a constant luminosity rather than high pile up at the start of a run, and low luminosity at the end [26]. Using the initial geometric loss factor of $\sim \frac{1}{2}$ the luminosity can be artificially lowered therefore increasing beam lifetime. Over time the geometric loss factor can be removed and effective head on collision is achieved thus increasing luminosity. This allows for a higher average luminosity and is referred to as luminosity leveling. This can also be achieved by varying β^* however this was not considered viable at the time as it had not been experimentally confirmed. More recent tests in the LHC before the 2013 shutdown showed that β^* variation would be possible and a combination of both crab cavities and β^* variation would be the most likely scenario [27].

There are several upgrade scenarios based on optimizing and improving the main three beam parameters available, with the aim of reaching a levelled luminosity of $5 \cdot 10^{34}$ cm$^{-2}s^{-1}$ and the potential to reach a peak of $2.5 \cdot 10^{35}$ cm^{-2}s^{-1}. Due to the necessity for an increased crossing angle over the current 300 μrad to $420 - 590$ μrad, only those scenarios that include crab cavities are able to reach this target.

The main beam parameters being upgraded are shown in Table 1.1. The two scenarios shown correspond to different bunch spacings.

Parameter	Nominal	25 ns	50 ns
$N_b[10^{11}]$	1.15	2	3.3
n_b	2808	2808	1404
X-ing [μrad]	300	420	520
$\beta^*[m]$	0.55	0.15	0.15
$\sigma_z[cm]$	7.55	7.55	7.55
Piwinski factor	0.65	5.57	5.08
R	0.839	0.177	.193
Peak Luminosity [cm$^{-2}s^{-1}$]	$1 \cdot 10^{34}$	$24 \cdot 10^{34}$	$25 \cdot 10^{34}$
Leveled Luminosity [cm$^{-2}s^{-1}$]	$1 \cdot 10^{34}$	$5 \cdot 10^{34}$	$2.5 \cdot 10^{34}$

Table 1.1: Upgrade parameters for the LHC[17].

1.3 Crab Cavity Upgrade

The upgrade scenario for the LHC requires an increase in crossing angle to avoid detrimental effects of beam-beam interactions. This increase in crossing angle leads to a geometric loss in luminosity as the beam profile is much longer than it is wide. The crossing angle results in significant drop off in luminosity as there is not a good overlap between the beams. To mitigate this loss, the beams can be rotated prior to crossing such that, as they collide they are head-on. This effectively simulates head-on collision and the loss can be almost entirely recovered. This rotation of the beam to allow effective head-on colliding is referred to as crabbing and will be discussed fully in Chapter 2. To rotate the beam for crabbing, the cavity provides a transverse kick that gives the bunch momentum. By giving the front of the bunch momentum in one direction, and the back the opposite direction, as the beam travels towards the IP, the bunch rotates. The removal of the crabbing by additional cavities after collision, eliminates this transverse momentum at a time when the bunch has zero rotation relative to the beam direction [28].

The comparison between head-on, non-crabbed and crabbed collisions is shown in Figure 1.4. The head-on collision is desired but unfeasible with a recirculating machine. Thus, collisions at an angle are needed. By using crab cavities, the bunch can be rotated such that at the IP the bunches are effectively head-on and maximum overlap is achieved.

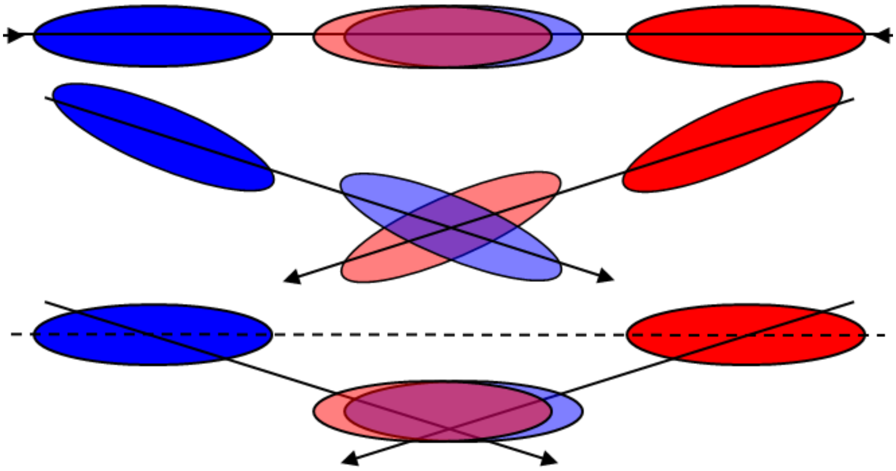

Figure 1.4: Top: Head-on collision. Middle: Normal collision at an angle. Bottom: Collision with crab cavity at an angle.

The principle of using crab cavities this way - 'crab crossing' - was first proposed by R.B. Palmer [29] for use in linear colliders but was not used in any practical accelerators until a crab cavity was used in the KEKB experiment [30]. The KEKB experiment successfully used crab cavities to remove a geometric loss from a 22 mrad crossing angle. Initially each beam would have two crab cavities, one to induce the rotation of the beam and one to remove it. This was later abandoned in favour of a single crab cavity per beam as it was cheaper and having two cavities would require an upgrade to the existing cryogenic system.

The KEKB crab cavity was designed to preform two tasks. Firstly, eliminate the geometric luminosity loss due to a crossing angle at low current. The second was to increase the beam-beam tune shift, which is proportional to the luminosity of the KEKB setup at high current. The beam-beam effects are the electromagnetic interactions between incoming and outgoing bunches in a machine. The electromagnetic forces between the separate bunches induce dipole like and higher order perturbations. The beam beam tune shift can be used to measure particle interaction in the bunch and hence luminosity.

These interaction can result in defocusing, transverse deflection and an increase in halo size [31][32].

The KEKB experiment was able to confirm bunch rotation though the use of streak cameras, and that the lost specific luminosity at low current was regained. However, the crab cavity was unable to provide increased luminosity at high current, due to lack of understanding of the beam-beam effects and how they relate to luminosity [33]. Due to this, it was widely misunderstood that crab cavities do not provide luminosity recovery. This is now known to not be the case, the specific luminosity did reach the desired maximum due to geometric recovery at low current, however at higher currents there was no gain. In the case of the LHC, the crossing angle is the main concern and the beam-beam effects are less of an impact, thus the geometric gains are desirable.

Two scenarios present themselves for operation of the crab cavities in the LHC - global and local.

In the case of a global scheme, the cavities induce a rotation in the bunch at a suitable location on the ring. The bunch rotation oscillates around the entire ring as it is kicked by various focus magnets. The cavities can then be used to top up or remove the rotation as needed.

In the case of a local scheme, the crabbing is induced shortly before an interaction region and removed soon after. Each IP that requires crabbing would need both crab cavities to induce the rotation and anti-crab cavities to remove it again after.

The global scheme would call for 800 MHz cavities that would fit between the opposing beam lines, in a region where the beam lines have enough separation [34] .

The local scheme calls for 400 MHz cavities. Due to the relatively close nature of the IP's in the local scheme, the beam pipes are very close together - situated 194 mm centre to centre apart. Each beam pipe has an inner radius of 42 mm. This requires the cavity to have a maximum outer radius of 152 mm, not including the wall thickness of the opposing beam line. The outer radius of a typical elliptical cavity is related to its frequency of operation. For a 400 MHz elliptical cavity, an outer radius of 375 mm would not be unexpected. As this is considerably greater than the space available, a novel design is needed that will fit within the limited space. There was no option to use 800 MHz cavities in the local scheme as they would result in the bunches taking on a 'snake' like shape due to the non linearity of the sinusoidal deflecting wave. This is shown in Figure 1.5. The limited space would also be less than required for a normal 800 MHz cavity and as such would have to be compact anyway.

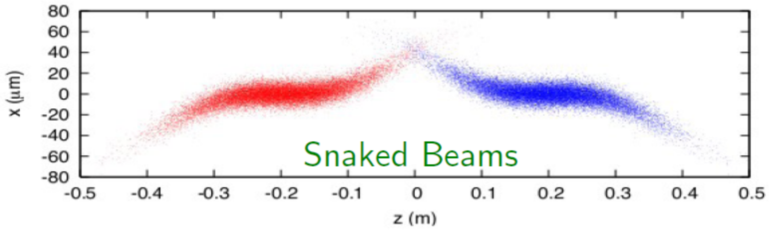

Figure 1.5: Profile of the snaked bunches [35].

Of the two scenarios it was deemed that the local scheme provided the most promise. The global scheme required the bunches to oscillate around a large proportion, if not all, of the ring. This oscillation was deemed unacceptable as the collimators would be subjected to an unacceptable level of beam. Thus the decision was made to use more compact crab cavities close to the interaction region where minimal impact would be made on the main operation of the LHC.

As the crab cavities would be expected to run continually, providing a total transverse kick of up to10 MV, they must be superconducting. A normal conducting cavity providing this transverse voltage would not be able to support this level of ohmic heating in constant wave (CW) operation.

1.4 Summary

The LHC currently provides some of the best and most interesting experimental scientific output in the field of physics in the world. This can be seen in the recent discoveries regarding the Higgs particle, its impact on the scientific community and its understanding of fundamental forces. So that the LHC can continue to provide world-leading physics, an upgrade to some of its major components is required. This upgrade will enable it to effectively operate for a further 15-20 years. Although the Higgs like particle has been discovered, it still requires study and more data to confirm that was was recorded is the Higgs particle. The upgrade will enable the 14Tev collision energy, which is the highest in the world currently, to have a higher data output. The upgrade will primarily focus on the injection setup, for example LINAC4, and the interaction region, for example the final focus triplets. As the interaction points are upgraded, the crossing angle of the beams will be increased to reduce beam-beam effects. This increase in crossing angle must be mitigated as it would result in a large loss of luminosity if not corrected for. Crab cavities provide the necessary luminosity recuperation by creating effective head-on collisions. However, the space available for the crab cavities is extremely limited. Thus a compact superconducting crab cavity is required for the HL-LHC upgrade.

Chapter 2

Crab Cavities

A crab cavity is a type of radio frequency (RF) cavity used for bunch rotation because of its transverse electric and magnetic fields[29]. This chapter will discuss the fundamental properties of cavities and how the transverse deflection is calculated using Panofsky Wenzel theorem. It will also discuss beam dynamics in brief, some fundamental properties of Superconducting RF (SRF), a brief history of prominent previous deflectors and the KEK-B crab cavity, and options for the LHC compact crab cavity.

2.1 Radio Frequency Basics

Within an RF cavity there are multiple mode configurations that can exist. For a pillbox cavity of length $\frac{\lambda}{2}$ the fundamental mode is TM_{010}, where the electric field is maximum in the centre of the cavity and parallel to the beampipe . The next field configuration is the TM_{110}, where there is an azimuthal variation in the electric field of the cavity. This second mode is often referred to as a dipole mode. This dipole mode in an accelerating cavity can act like a time-varying dipole magnet if it is excited. The mode can be used for one of two main variations, depending on the phase of the cavity. In one phase, the beam is 'deflected' giving the whole bunch transverse momentum which can be used to separate bunches. Ninety degrees out of phase from this, the bunch is rotated or 'crabbed'. This is where the front of the bunch is given momentum in an opposite direction to the rear of the bunch, with the centre remaining unperturbed. This results in the bunch rotating as it travels. Both of these rely on the potential gradient that exists between the opposing directions of electric field to impart momentum to the bunch.

In order to rotate the bunches, a time-varying force is required. The force on a charged particle is given by the Lorentz force:

$$\mathbf{F} = q(\mathbf{E} + \mathbf{v} \times \mathbf{B}) \tag{2.1}$$

thus a a time-varying electric or magnetic field can be used to produce a transverse kick. For a particle travelling in the z direction, if deflection in the x direction is desired, the electric field must also be in the x direction, and/or the magnetic field in the y.

$$F_x = q(E_x + v_z \times B_y) \tag{2.2}$$

As the bunch length in the LHC is only 1.06 ns, the field must vary very quickly as the bunch passes through the cavity, so that the head and tail of the bunch receive equal and opposite kicks. For these kicks to be of sufficient magnitude and duration, an RF cavity must be used.

A pillbox cavity is the simplest form of a cavity consisting of a cylindrical can with flat end plates. The solution to the wave equation can be easily calculated for a pillbox cavity, and the mode structure that is present holds true for other cavities.

The wave equation in cylindrical polar co-ordinates is;

$$\left[\frac{1}{r}\frac{\delta}{\delta r}\left(r\frac{\delta}{\delta r}\right) + \frac{1}{r^2}\frac{\delta}{\delta\phi^2} + \mu\epsilon\omega^2 - k_z^2\right]\psi = 0 \tag{2.3}$$

where r is the radius, ϕ is the angular position, μ is the permeability, ϵ is the permittivity, ω is the angular frequency, k_z is the longitudinal wave-number and ψ is the solution.

The solution takes the form;

$$\psi = A_1 J_m(k_t r) e^{\pm im\theta} \tag{2.4}$$

where J_m is the m^{th} Bessel function and ψ is the the longitudinal componant of the field, either E_z or H_z depending on which orientation is chosen.

The first four Bessel functions are shown in Figure 2.1.

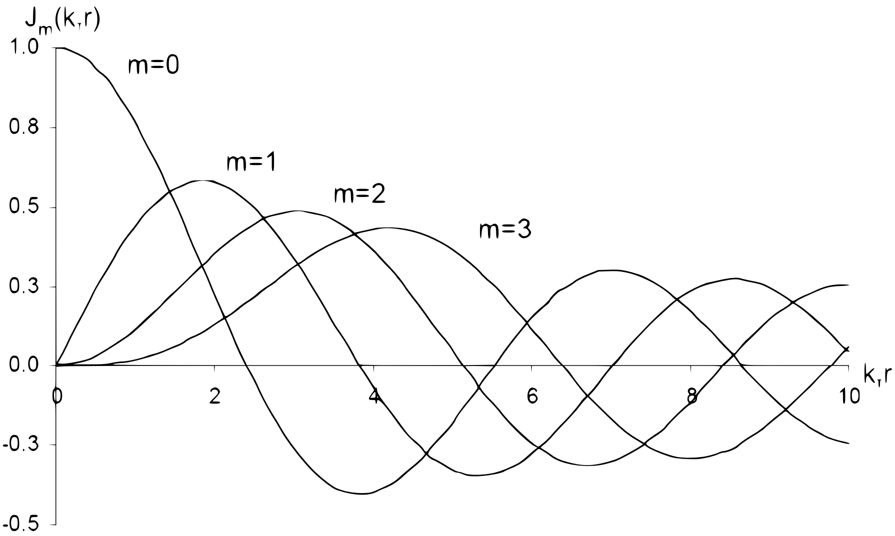

Figure 2.1: The first four Bessel functions.

In a pill box cavity, all modes supported therein will be of either the $\text{TE}_{m\,n\,p}$ or $\text{TM}_{m\,n\,p}$ form. A $\text{TE}_{m\,n\,p}$ is defined by the absence of an electric field in the longitudinal direction; it does still support a magnetic field longitudinally. A $\text{TM}_{m\,n\,p}$ is similarly defined as the absence of a magnetic field in the longitudinal direction; a longitudinal electric field is supported. The solutions to the above wave equation take on the following form;

for TE modes;

$$\begin{aligned} H_z(r,\phi) &= A_1 J_m\left(\frac{\xi'_{m,n} r}{a}\right) e^{\pm im\phi} && (2.5)\\ H_\perp &= \frac{ik_z a^2}{\xi'^2_{m,n}} \nabla_\perp H_z && (2.6)\\ E_\perp &= -\frac{i\epsilon\omega a^2}{\xi'^2_{m,n}} (\hat{z} \times \nabla_\perp H_z) && (2.7) \end{aligned}$$

for TM modes;

$$\begin{aligned} E_z(r,\phi) &= A_1 J_m\left(\frac{\xi_{m,n} r}{a}\right) e^{\pm im\phi} && (2.8)\\ E_\perp &= \frac{ik_z a^2}{\xi^2_{m,n}} \nabla_\perp E_z && (2.9)\\ H_\perp &= \frac{i\epsilon\omega a^2}{\xi^2_{m,n}} (\hat{z} \times \nabla_\perp E_z) && (2.10) \end{aligned}$$

where A_1 is the normalized field, $\xi_{m.n}$ is the Bessel function zero corresponding to m and n, a is the radius ϕ is the radial angle, $E_\perp$ and $B_\perp$ correspond to the transverse components of the electric and magnetic field and $\nabla_\perp = \nabla - \frac{\delta}{\delta z}$.

Modes that follow the pattern $\mathrm{TM}_{0\,n\,p}$ or $\mathrm{TE}_{0\,n\,p}$ are known as monopole modes, Figure 2.2 shows the electric field distribution along the z axis of the first TM monopole mode. The peak electric field is concentrated in the centre of the cavity and decreases radially.

Modes that follow the structure of $\mathrm{TM}_{1\,n\,p}$ or $\mathrm{TE}_{1\,n\,p}$ are known as dipole modes. Figure 2.3 shows the electric field distribution along the z axis of the first $\mathrm{TM}_{1\,n\,p}$ dipole mode. The electric field is split, with one half in the positive z direction and the other half in the negative z direction. With any dipole mode, in a pillbox cavity, there will be a same order mode [SOM] that has an identical shaped field profile that is rotated by 90^o. This second mode is often undesirable and will be removed where needed.

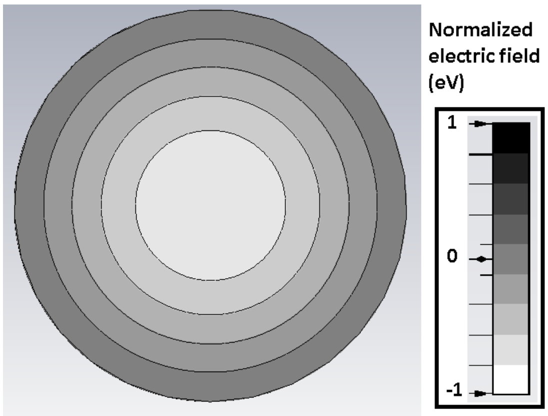

Figure 2.2: Mode position for the monopole mode

To align the dipole mode within the cavity a number of differing methods can be used, be they, rod inserted into the cavity, plates attached to the sides, squashing the cavity or waveguide coupling. These alterations to the cavity geometry have the effect of aligning the dipole field with the beam at the desired angle. The SOM is often shifted in frequency away from the operating mode allowing it to be damped more effectively.

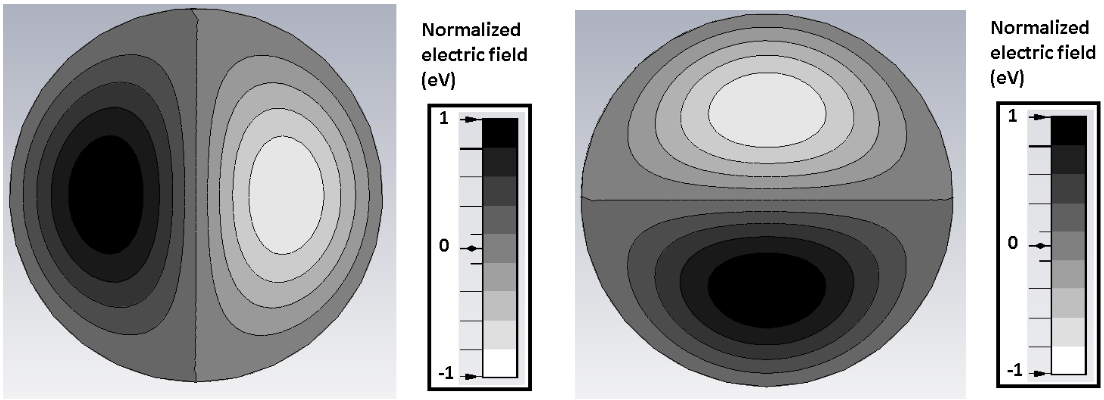

(a) (b)

Figure 2.3: Mode configurations for the two polarizations of the dipole field

The modes following the structure of TM_{2np} or TE_{2np} are known as quadrupole modes. Figure 2.4 shows the electric field distribution along the z axis of the quadrupole mode. Similar to the dipole mode, the quadrupole mode has a SOM that is again rotated 45^o.

J0(x) and J1′(x) are the only Bessel functions or differential Bessel functions

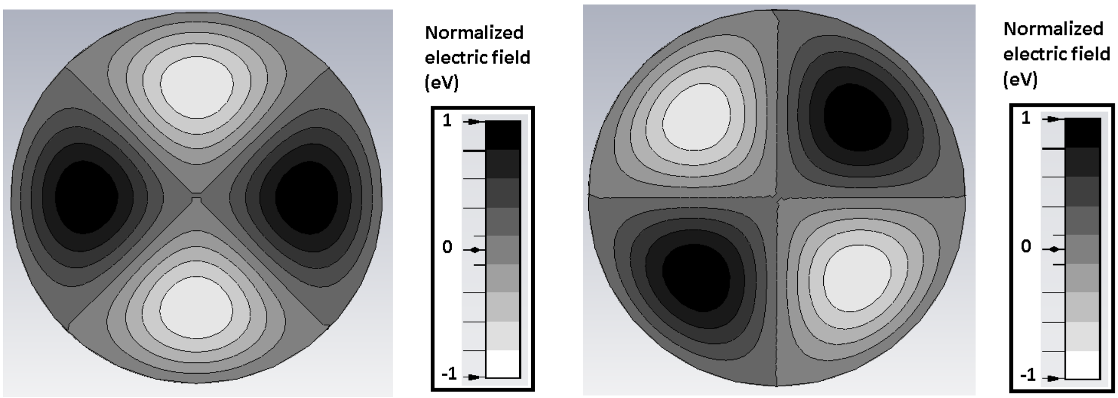

(a) (b)

Figure 2.4: Mode polarizations for the quadrupole mode.

of the first kind that have finite values at $x = 0$. However the J0(x) field comes from the H_r and E_ϕ terms of the monopole modes, which are multiplied by $\sin(m\phi)$ where ϕ is the radial position. As $m = 0$ for monopole modes, $H_r = E_\phi = 0$. Hence only modes with fields that vary as J1'(x) can have transverse fields on axis. Only the dipole modes, $m = 1$, have this field variation in a pillbox cavity.

The fields for the first two dipoles are given as:

For the TM$_{1\,1\,0}$ dipole mode;

$$\begin{aligned}
E_z &= E_0 J_1(k_t r)\cos(\phi) && (2.11)\\
H_z &= 0 && (2.12)\\
H_r &= \frac{i\omega\epsilon}{k_t^2 r} E_0 J_1(k_t r)\sin(\phi) && (2.13)\\
E_r &= \frac{-ik_z}{k_t} E_0 J_1'(k_t r)\cos(\phi) && (2.14)\\
H_\phi &= \frac{-i\omega\epsilon}{k_t} E_0 J_1'(k_t r)\cos(\phi) && (2.15)\\
E_\phi &= \frac{ik_z}{k_t^2 r} E_0 J_1(k_t r)\sin(\phi) && (2.16)
\end{aligned}$$

For the TE$_{1\,1\,1}$ dipole mode;

$$
\begin{aligned}
E_z &= 0 && (2.17)\\
H_z &= H_0 J_1(k_t r)\sin(\phi) && (2.18)\\
H_r &= \frac{ik_z}{k_t} H_0 J_1'(k_t r)\sin(\phi) && (2.19)\\
E_r &= \frac{-i\omega\mu}{k_t^2 r} H_0 J_1(k_t r)\cos(\phi) && (2.20)\\
H_\phi &= \frac{-ik_z}{k_t^2 r} H_0 J_1(k_t r)\cos(\phi) && (2.21)\\
E_\phi &= \frac{i\omega\mu}{k_t} H_0 J_1'(k_t r)\sin(\phi) && (2.22)
\end{aligned}
$$

Both of these modes have either transverse electric or magnetic field components that could potentially deflect a passing bunch .

2.1.1 PW Theorem

In 1956, a paper by Panofsky and Wenzel[36] demonstrated how transverse momentum could be imparted to a fast moving particle parallel to the axis. This theorem allows the deflection of a particle normal to the direction of travel to be calculated from the electric field in the direction of travel, rather than needing both the electric and magnetic fields and the phase between them as in the case of integrating the Lorentz force. This method does not hold for all situations but is accurate over the area of interest for crab cavities as the longitudinal electric field on axis is usually zero.

This was discussed in a paper by Browman [37] in 1993. His derivation is shown here.

The transverse momentum $\mathbf{p}_\perp$imparted to a particle with velocity v and charge e travelling in the z direction through an radio frequency cavity of length d is given by;

$$\mathbf{p}_\perp = \int_{t(z=0)}^{t(z=d)} \mathbf{F}_\perp dt = \left(\frac{e}{v}\right)\int_0^d [\mathbf{E}_\perp + (\mathbf{v}\times\mathbf{B})_\perp] dz \qquad (2.23)$$

if v is large enough to allow the particle direction to remain essentially unchanged by the transverse force. Equation (2.23) can be simplified by taking the right hand side as a vector potential;

$$\mathbf{E} = -\frac{\delta \mathbf{A}}{\delta t} - \nabla \mathbf{V} \tag{2.24}$$

where $\mathbf{A}$ is the magnetic vector potential and $\mathbf{V}$ is the scalar potential.

As $\mathbf{V}$ is constant inside the cavity;

$$\mathbf{E} = -\frac{\delta \mathbf{A}}{\delta t} \tag{2.25}$$

and;

$$\mathbf{E}_{\perp} = -\frac{\delta \mathbf{A}_{\perp}}{\delta t} \tag{2.26}$$

$(\mathbf{v} \times \mathbf{B})_{\perp}$ in terms of $\mathbf{A}$;

$$\begin{aligned}(\mathbf{v} \times \mathbf{B})_{\perp} &= [\mathbf{v} \times (\nabla \times \mathbf{A})]_{\perp} = [\nabla(\mathbf{v} \cdot \mathbf{A}) - (\mathbf{v} \cdot \nabla)\mathbf{A}]_{\perp} & (2.27)\\ &= \nabla_{\perp}(\mathbf{v} \cdot \mathbf{A}) - (\mathbf{v} \cdot \nabla)\mathbf{A}_{\perp} & (2.28)\end{aligned}$$

Thus we can state;

$$\mathbf{p}_{\perp} = \frac{e}{v}\int_0^d \left[\left(-\frac{\delta \mathbf{A}_{\perp}}{\delta t} - (\mathbf{v} \cdot \nabla)\mathbf{A}_{\perp}\right) + \nabla_{\perp}(\mathbf{v} \cdot \mathbf{A})\right] dz \tag{2.29}$$

As $\mathbf{v}$ is essentially constant and in the z direction;

$$(\mathbf{v} \cdot \nabla)\mathbf{A}_{\perp} = v\frac{\delta \mathbf{A}_{\perp}}{\delta z} \tag{2.30}$$

and;

$$\nabla_{\perp}(\mathbf{v} \cdot \mathbf{A}) = v\nabla_{\perp} A_z \tag{2.31}$$

thus;

$$\mathbf{p}_\perp = \left(\frac{e}{v}\right)\int_0^d \left[\left(-\frac{\delta \mathbf{A}_\perp}{\delta t} - v\frac{\delta \mathbf{A}_\perp}{\delta z}\right) + v\nabla_\perp A_z\right] dz \tag{2.32}$$

$$= e\int_0^d \left[\left(-\frac{1}{v}\frac{\delta \mathbf{A}_\perp}{\delta t} - \frac{\delta \mathbf{A}_\perp}{\delta z}\right) + \nabla_\perp A_z\right] dz \tag{2.33}$$

however;

$$v = \frac{dz}{dt} \tag{2.34}$$

allowing the simplification;

$$\left(\frac{1}{v}\frac{\delta \mathbf{A}_\perp}{\delta t} + \frac{\delta \mathbf{A}_\perp}{\delta z}\right) dz = \frac{\delta \mathbf{A}_\perp}{\delta t}dt + \frac{\delta \mathbf{A}_\perp}{\delta z}dz = d\mathbf{A}_\perp \tag{2.35}$$

$$\mathbf{p}_\perp = e\int_{\mathbf{A}_\perp(z=0)}^{\mathbf{A}_\perp(z=d)} -(d\mathbf{A}_\perp) + e\int_0^d \nabla_\perp A_z dz \tag{2.36}$$

For this to be useful, **A** needs to be expressed in terms of **E**, assuming $e^{-i\omega_0 t}$ time dependence on **E** then;

$$\mathbf{A} = -\frac{i}{\omega_0}\mathbf{E} \tag{2.37}$$

is a valid choice for **A**[1]. The first term of Equation (2.36) vanishes as for any cavity where the ends are perpendicular to its axis, $\mathbf{A}_\perp = \mathbf{E}_\perp = 0$ (in metal). It can also vanish for cavities with beam pipes, as long as $\mathbf{E}_\perp = 0$, as $z = 0$ and $z = d$ where d is the length of the cavity. Thus in this case;

$$\mathbf{p}_\perp = e\int_0^d \nabla_\perp A_z dz \tag{2.38}$$

where e is the charge on an electron. Substituting (2.37) into (2.38) we obtain;

---

[1] $-i = e^{-1\frac{\pi}{2}}$ so **A** has a time dependence of $e^{-i(\omega_0 t+\frac{\pi}{2})}$. Thus **A** is shifted 90^0in time from **E** and has the same phase as the magnetic field as would be expected.

$$\mathbf{p}_{\perp} = \left(\frac{e}{\omega_0}\right) \int_0^d (-1)\nabla_{\perp}\mathbf{E}_z dz \tag{2.39}$$

As the particles being deflected have very high longitudinal energy, the transverse kick can be approximated to an equivalent kick from an electric field, using $E = cB$ where c is the speed of light. Using this approximation, we can define the transverse voltage as;

$$V_{\perp =} - c \int_0^d dz \int_{t_0}^{\frac{z}{c}} dt \left(\nabla_{\perp} E_z(z,t)\right) \tag{2.40}$$

where t_0 is the initial time, $\frac{z}{c}$ is the time taken to reach the position z along the z axis and $E_z(z,t)$ is the electric field at the position z at time t.

This can be further simplified, as we know the electric field follows the time dependence $e^{-i\omega_0 t}$.

$$V_{\perp =} - \frac{ic}{\omega} \int_0^d dz \nabla_{\perp} E_z(z, \frac{z}{c}) \tag{2.41}$$

For a dipole mode $m = 1$, this can be simplified to

$$V_{\perp(0) =} - \frac{ic}{\omega r}\left(V_{\parallel(0)} - V_{\parallel(r)}\right) \tag{2.42}$$

where $V_{\parallel}$ is the longitudinal voltage at a radius r.

For a cylindrically symmetric cavity, where there is no longitudinal voltage on axis, this can then be approximated to;

$$V_{\perp(0) =} - \frac{icV_{\parallel(r)}}{\omega r} \tag{2.43}$$

The transverse shunt impedance $R_{\perp}$can be calculated;

$$R_{\perp =} \frac{1}{2}\frac{\mid V_{\perp}\mid^2}{P_c} \tag{2.44}$$

Similarly a calculation for transverse $R_{\perp}/Q$, a useful property for examining the ratio of transverse deflecting voltage to stored energy, can be made;

$$\frac{R_\perp}{Q} = \frac{|V_\perp|^2}{2\omega U} = \frac{|V_\parallel(r)|^2}{2\omega U}\left(\frac{c}{\omega r}\right)^2 \tag{2.45}$$

where $R_\perp$ is the transverse shunt impedance and Q is the cavity quality factor.

Equation 4.14 shows that the transverse kick a beam receives can be calculated from the longitudinal electric field, however equation 2.17 shows us that a TE$_{m\,n\,p}$ has no longitudinal electric field. Thus it can be inferred that only TM$_{1\,n\,p}$ modes are actually able to deflect a beam.

2.2 Beam Dynamics

The deflection experienced by a bunch in a dipole cavity can be expressed geometrically. If the assumption is made that the deflection will be significantly small compared to the longitudinal direction, small angle approximation can also be used. Taking the beam energy in the longitudinal direction z to be E_{beam} , and in the transverse direction x a voltage to be $V_\perp$, a triangle can be constructed with the angle of the deflection ϕ.

$$x = z\tan(\phi) \tag{2.46}$$

Thus the small angle can be assumed to be $\frac{v_t}{v_z}$;

$$x = z\tan\left(\frac{V_\perp}{E_{beam}}\right) \tag{2.47}$$

which can then be further simplified via small angle approximation;

$$x \approx z\left(\frac{V_\perp}{E_{beam}}\right) \tag{2.48}$$

Using the simplified transformation R_{12} which in this case is analogous to length adjusted due to the focusing and defocusing elements between the two points. R_{12} is part of the the transfer matrix that allows the transverse properties of the bunch to be described as it travels round the accelerator.

$$\begin{matrix} x_2 \\ x'_2 \\ y_2 \\ y'_2 \end{matrix} = \begin{matrix} R_{11} & R_{12} & R_{13} & R_{14} \\ R_{21} & R_{22} & ... & ... \\ ... & ... & R_{33} & ... \\ R_{41} & ... & ... & R_{44} \end{matrix} \cdot \begin{matrix} x_1 \\ x'_1 \\ y_1 \\ y'_1 \end{matrix} \tag{2.49}$$

We can make the assumption that $x_2 = R_{12}x'_1$ as the bunch will be travelling near the speed of light, resulting in no perturbation in the y direction, and almost no shift in the position of x as it passes though the cavity, thus the assumption $R_{11} \approx R_{13} \approx R_{14} \approx 0$.

The position becomes:

$$x = R_{12} \left(\frac{V_{\perp}}{E_{beam}} \right) \tag{2.50}$$

However, this assumes that the collision is linear and not recirculating.

An idealised particle in a synchrotron will follow a circular path through the centre of all magnets as it circulates the ring, ending up at the same position that is started at. This is referred to as a closed orbit. In practice, real particles have a spread in position and momentum, and the components of the facility have small errors in them. This results in the particles osculating around the closed orbit as they circulate the ring. This is referred to as betatron motion, or betatron oscillation.

The number of oscillations per revolution a bunch experiences is referred to as the betatron tune Q, given as;

$$Q = \int_{s}^{s+C} \frac{ds}{\beta_y(s)} \tag{2.51}$$

where s is the position within the ring, C is the circumference of the ring and $\beta_y(s)$ is the betatron function at s.

The betatron frequency β_f is the tune multiplied by the revolution frequency of the ring f_0.

$$\beta_f = Q \cdot f_0 \tag{2.52}$$

It is important that the tune does not fall at integer values as this increases the chance of errors in the cavities compounding which leads to the beam destabilising. If the tune was an integer, then on every revolution the bunch phase distribution would be the same at a given point. This would result in any errors compounding on each revolution. If the tune was a half integer, then the dipole errors would cancel out on each revolution as the phase distribution would be opposite. However, a half integer is not usually chosen as it results in resonances from quadrupole terms as these similarly compound. Other fractional values are excluded due to resonances within the machine that could build in the same way.

If an error was introduced at a frequency $(n \pm Q) f_0$ in the form of a deflecting field, then this leads to a signal S;

$$S = \sin\left(2\pi(n - \pm Q) f_0 t\right) \tag{2.53}$$

This results in the bunch seeing the kick;

$$S = \sin\left(2\pi n f_0 t\right) \sin\left(2\pi(n - \pm Q) f_0 t\right) \tag{2.54}$$

which can be simplified using;

$$S = \sin(a)\cos(b) = \frac{1}{2}\left(\sin(a + b + \sin(a - b)\right) \tag{2.55}$$

to get a dependence on;

$$S \approx \sin\left(2\pi Q f_0 t\right) \tag{2.56}$$

Thus an error in the side bands of the betatron tune $(n \pm Q) f_0$ can result in a perpetual build up of deflection, resulting in an RF knock-out as the beam is deflected [38].

When crab cavities are added, they will inevitably disrupt the closed orbit of the LHC. There are two options for correcting the closed orbits.

In the local scheme, the bunch is rotated between the crabbing cavities and the anti-crab cavities, with the crab cavities disrupting the closed orbit and the anti-crab's returning the bunch to the expected orbit. This results in the crabs acting like a local bump and the orbit in the rest of the ring not being effected.

In the global scheme, the initial expectation with the bunches retaining their rotation throughout the entire ring appears to result in a larger kick on each revolution. However, by choosing the correct location of the cavity, it is possible to create new closed orbits for the particles. This results in the cavity maintaining the oscillation as it travels round the machine. Each particle within the bunch obtains a new closed orbit. This, for example, could result in a particle getting transverse momentum on the first pass and have it removed on the second [39].

The voltage required to deflect the beam depends on the scheme selected.

For the local scheme, the voltage required is given as;

$$V_{crab} = \frac{c^2 \cdot p_s \cdot \tan(\frac{\theta}{2})}{q \cdot \omega \cdot \sqrt{\beta^* \cdot \beta_{crab}} \cdot \sin(\Delta\phi_0)} \tag{2.57}$$

where c is the velocity of light, $p_s$is the particle momentum, θ is the crossing angle, q is the charge on the particle, ω is the angular frequency of the cavity, $\Delta\phi_0$ is the phase advance between the cavity and the IP and β^* and β_{crab} are the beta functions at the IP and crab location respectively.

For the anti-crab cavities, the voltage required is ;

$$V_{anti} = -R_{22} V_{crab} \tag{2.58}$$

where R_{22} is the $(2, 2)$ element of the transfer matrix between the crab and anti-crab cavities.

For the global scheme, the voltage is given as;

$$V_{crab} = \frac{c^2 \cdot p_s \cdot \tan(\frac{\theta}{2})}{q \cdot \omega \cdot \sqrt{\beta^* \cdot \beta_{crab}}} \cdot |\frac{2\sin(\pi Q)}{\cos(\Delta\phi_0 - \pi Q)}| \tag{2.59}$$

where Q is the betatron tune of the ring and the other parameters are the same as for the local scheme[39] .

2.3 Introduction to SRF

RF refers to an electronic device operating at radio frequencies, therefore SRF is an abbreviation of Superconducting Radio Frequency. A superconducting cavity is one that is constructed of a material that when cooled below a critical temperature (T_c), its internal resistance drops to be almost zero. For an AC current, a very small residual resistance will be present that is analogous to inertia. This BCS resistance scales with the square of the frequency of the applied current. Conventional normal-conducting cavities may be fed with up to tens of mega watts of power, often for very short time periods which results in massive power loss. This can be due to ohmic heating as the RF power is dissipated into the walls through resistance, or removed to an external dump in a travelling wave structure. By using superconducting cavities, power dissipation in the walls can be almost completely removed, requiring less power to be fed into the cavity and thus making it cheaper.

However, the cost savings made by reducing the amount of wasted power must be compared to the costs of running the cavity at the desired temperature. The machine is limited by the Carnot cycle, this provides an efficiency decrease of:

$$Carnot\, efficiency = 1 - \frac{T_c}{T_H} \tag{2.60}$$

where T_c is the temperature of the cold sink and T_H is the temperature of the hot sink.

This provides an efficiency of $\sim 1-2\%$ for cavities operating at temperatures $\sim 3-6$ K.

The most common material for use as a superconductor is niobium. Niobium is used as it has one of the highest T_c's of any of the periodic elements. It is also able to sustain the highest critical surface fields [40]. Niobium becomes superconducting at 9.2 K, but usually operates at 4.2 K. This is because the niobium is submerged in liquid helium which acts as a coolant, and 4.2 K is the temperature of liquid helium [41]. Liquid helium baths are used due to the large enthalpy that can be absorbed in the cold vapor [42]. Superconducting cavities are often operated at $\sim$ 2 K with the liquid helium being pumped to a lower pressure. The lower temperature improves the SRF properties of the niobium, lowering the surface resistance of the niobium. This has the added benefit of improving the thermal conductivity of the liquid helium. The liquid helium becomes superfluid, so there is no bubbling, and this reduces microphonics within the cavity. By operating at a temperature well below that of the superconducting transition, the chance of a quench can be reduced. A quench is when a superconducting cavity suddenly becomes normal conducting. This reduction comes from the material resistances (*Res*) continued dependence on its temperature;

$$Res \propto exp(-1.76\frac{T_c}{T}) \tag{2.61}$$

where T_c is the critical temperature and T is the current temperature. This reduction in resistance reduces the chance of localised heating and thus a quench [43].

By having very low losses in the cavity walls, the cavities can be run continually at high gradient, unlike normal conducting cavities that must be pulsed to avoid destroying the cavity. This proves advantageous when high repetition rates are required, as normal conducting cavities can only sustain a certain level of pulsed heating [44]. This leads to high power storage rings and synchrotrons using superconducting cavities as they are able to cope with the high repetition rates.

A number of RF parameters are used to describe the properties and behaviour of an SRF cavity. The most prominent of them will be described below.

Surface Resistance

One of the primary reasons for using a superconducting cavity is that the resistance of the cavity is several orders of magnitude smaller, $\sim n\Omega$, below a certain transition temperature (T_c). Although this would imply that below the transition temperature the resistance will be zero, it is not the case. The superconducting state is not perfect and there is a very small resistance within the material.

The surface resistance (R_s) can be summarized as,

$$R_s = R_{BCS} + R_0 \tag{2.62}$$

where R_{BCS} is the temperature and frequency dependent resistance from BCS theory, and $R_0$is the residual resistance. These will be expanded on below.

These parameters result in SRF cavities having very small but non zero resistance [43]. As the temperature decreases, the resistance becomes dominated by the residual resistance R_0 and no longer depends on the BCS resistance, this is shown in Figure 2.5.

BCS Theory

The BCS theory is widely accepted as the best microscopic explanation for the mechanisms of superconductivity. This theory proposed by Bardeen, Cooper and Schrieffer [BCS] allows for electrons to interact with each other within the ion lattice of a material. The electrons couple electromagnetically via the attractive force caused by the perturbation of the lattice. This interaction leads to the formation of Cooper pairs, where a pair of electrons of opposite spin form a boson-like particle with zero spin that obeys Bose-Einstein statistics. This al-

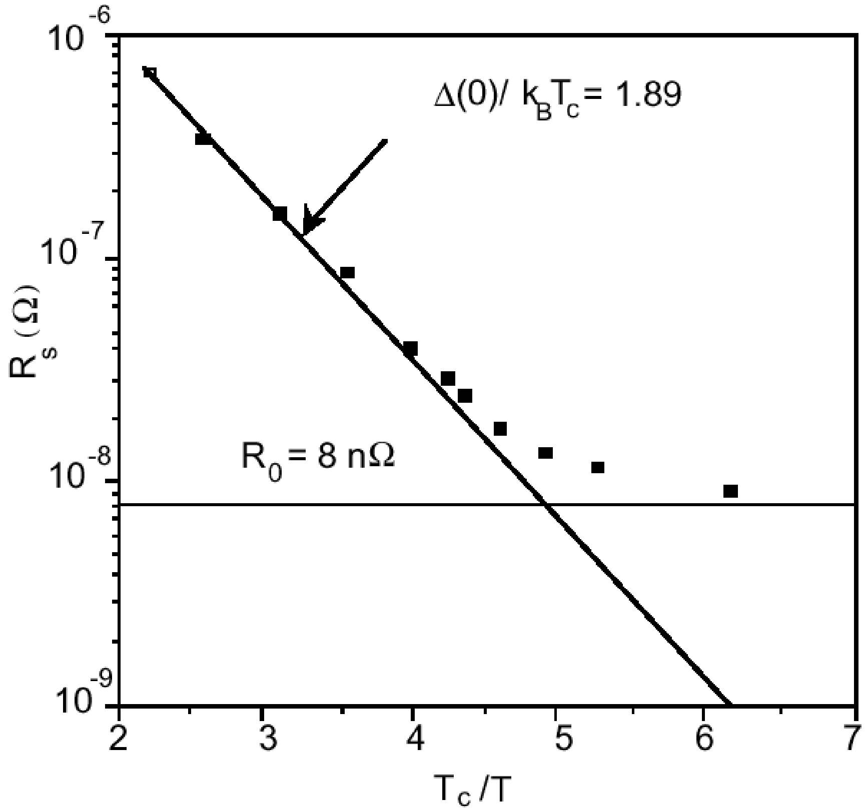

Figure 2.5: Surface resistance vs temperature [43].

lows the pairs to be in the same quantum state and thus exist with a lower combined energy than two separate electrons. The transition to Cooper pairs only happens below a certain transition temperature, T_c, dependent on the material. Above the transition temperature, the thermal vibrations of the lattice disrupt the coupling.

The resistance that electrons experience can be analogous to them colliding with other electrons and atoms on a quantum level. They are able to collide as their coherence length - the length at which they can be said to exhibit particle-like behavior instead of that of a wave - is comparable to the distance between atoms. The coherence length of a Cooper pair is considerably larger than that of an electron. Cooper pairs act more like a wave and less like individual particles on the atomic level. Because they exist in the same quantum state where they can't be scattered as in normal resistance, they act collectively. The longer coherence length also allows for defects or impurities, smaller than the coherence length, to be ignored.

The resistance due to BCS theory can be given as:

$$R_{BCS} = \frac{2 \cdot 10^{-4}}{T} \left(\frac{f}{1.5} \right)^2 \exp \left(-\frac{17.67}{T} \right) \tag{2.63}$$

where T is the temperature in Kelvin and f is the frequency, when $T < \frac{T_c}{2}$.

The resistance increases with the square of the RF frequency. The Cooper pairs themselves have inertial mass that must be overcome for them to move. In the case of an alternating field, as for an RF cavity, the continual change in direction leads to the BCS resistance. This leads to most superconducting cavities being low frequency, usually below ~ 4 GHz, as the trade off in surface heating and cryogenics is not viable at high frequency.

The resistance decreases exponentially with temperature. This is due to the condensation of Cooper pairs that carry the charge rather than electrons. As the temperature falls from the transition temperature (the temperature at which Cooper pairs start to form), the number exponentially increases until $T = 0\,\mathrm{K}$ where all charge carriers are Cooper pairs.

The BCS resistance can also be partly characterized by the amount of impurities in the bulk of the material. This is often referred to as the RRR value, with low RRR implying the material is of lower quality and containing more impurities. The residual resistance ratio (RRR) factor is usually used for thermal conductivity but acts as a good guide for the purity of the bulk material. It is defined as the ratio of the room temperature resistance to that of its saturated resistance at low temperature, as this is dominated by impurity scattering. This can be electrical or thermal conductivity as both are dominated by electron transport in metals.

Residual Resistance

There is always some resistance remaining in the structure even though the BCS resistance falls to zero, this is referred to as the residual resistance (R_0). The residual resistance can form from a number of characteristics of the material, these are usually due to the manufacturing of the cavity.

Magnetic flux can become trapped in regions of impurities, either from inadequate shielding from the Earth's magnetic field, or from indium joins or welds between differing parts of the cavity. The trapped magnetic flux results in currents flowing in the surface contrary to the surface fields of the cavity.

Hydrogen gas can become deposited in the surface of the cavity during cleaning by acid etching. Lossy hydrides then precipitate at the surface of the cavity, this is often called 'Q disease' as it can drastically affect the cavity Q. The effect is most often seen when a cavity is allowed to reach temperatures above 20^oC during acid treatment, though it is not the only source. The hydrogen is trapped in the bulk of the cavity and only precipitates out to the surface during cooling. To avoid the creation of hydrides, the cavity must be cooled quickly in the temperature region $\sim 120 - 170\,$K. By baking the cavity at $700 - 900^o$C under vacuum, most of the hydrogen trapped in the surface can be removed.

Oxides can form on the surface of the cavity if it is exposed to air, which is likely to happen at some point in the preparation of the cavity. By baking the cavity at higher temperatures, the oxides can be removed. However this is sometimes not possible due to the design of the cavity, for example indium seals could melt or the cavity could deform under its own weight.

Cavity Quality

The quality of a cavity is important as it is proportional to how much power needs to be supplied to the cavity to maintain its operating energy. A higher cavity quality means most of the power from the power supply is used to replace any energy deposited into the beam as it traverses the cavity. A low quality cavity would dissipate much of the input energy into its walls and heat up the cavity bulk.

The cavity quality $[Q_0]$ relates the dissipation of power in the cavity to the stored energy.

$$Q_0 = \frac{\omega_0 U}{P_c} \tag{2.64}$$

Where ω_0 is the angular frequency, U is the stored energy and P_c is the power dissipated into the cavity walls. The cavity will take approximately 2π times Q_0 the number of RF cycles to empty the cavity of all its stored energy.

Geometry Constant

The geometry constant is a useful parameter for comparing cavities of different frequency and material, as it depends on the shape of the cavity but not the frequency or material like Q_0. This allows a cavity to be scaled and compared to other cavity shapes more easily. The geometry factor is defined as,

$$G = Q_0 R_s \tag{2.65}$$

where R_s is the surface resistance.

Field Emission

The electrons in the surface of a metal are bound by a potential well that stops them from escaping. As the surface electric field increases, the potential well that the electrons must overcome to escape is lowered. As electrons are able to quantum tunnel though potential wells, this increases the statistical chance of an electron escaping. Thus, in high field regions, electrons can be ejected from the surface of a material.

Small defects on the surface of a cavity, either surface imperfections or contamination, can focus the local electric field. The defect can lead to the local electric field being higher and thus allowing electrons to pass though the potential well and be ejected from the surface. The lowering of the potential well is shown in Figure 2.6. The Fermi energy, E_F, is the base level of energy for electrons. The potential barrier that must be overcome to escape ϕ, however, theis becomes lowered due to the external electric field V_e. The new height of the effective potential barrier ϕ_{eff} provides a shorter distance that the electrons can tunnel though to escape [45].

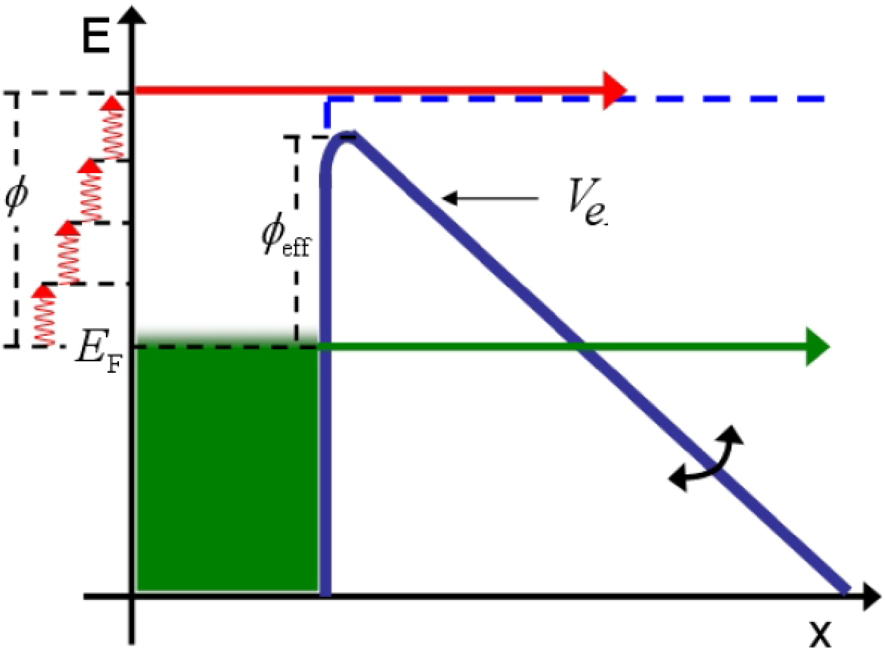

Figure 2.6: Electron energy barrier for emission[45].

This ejection leads to localized heating where the electrons are accelerated and collide with another surface. As the electrons travel they can also absorb RF power from the cavity. This can limit the performance of the cavity as the heating can disrupt the superconductivity.

RF Critical Magnetic Field

The maximum magnetic field that a superconductor can support is limited by three main factors - thermal breakdown due to defect heating, global thermal instability and the RF critical magnetic field.

As the magnetic field increases, the surface current will also increase to maintain Maxwell's equations. Small defects or impurities will not have the same superconducting properties as the bulk of the cavity. The defect is heated by the increased current and starts to affect the bulk around it. When the heat generated by the defect cannot be removed fast enough by the surrounding bulk, a quench will happen, as the bulk of the cavity is also heated above T_c.

If the bulk of the cavity becomes too hot due to the surface currents, then the temperature of the cavity can rise above T_c and a quench will happen.

The magnetic field supported by the cavity depends on the type of superconductor the cavity is made of. There are two types of superconductor, I and II. Type I superconductors have a critical magnetic field H_c based on the free energy in the material. When it is energetically favourable, all the flux is expelled from the material and it becomes superconducting. In a type II superconductor, like niobium, there are two critical fields. H_{c1} is the field at which below all magnetic field is expelled from the surface and and the material becomes completely superconducting. Between H_{c1} and H_{c2} is the field at which superconducting 'pockets' start to appear within the material allowing the formation of a mixed superconducting and normal state. The two states are shown in Figure 2.7.

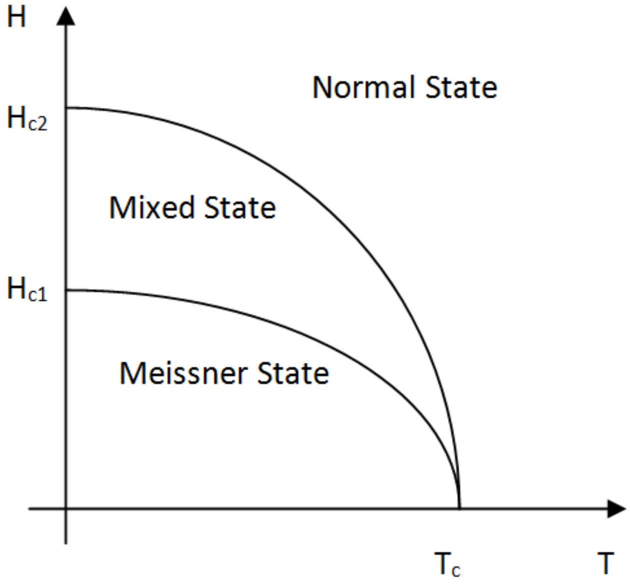

.

Figure 2.7: The two different states of the Type II superconductor

When in this mixed phase, the magnetic flux forms into fluxoids and is not uniformly distributed across the material. A super-vortex current surrounds each fluxoid to allow field and and current free regions. This is shown in Figure 2.8. As the magnetic field increases, these fluxoids become more dense until the material is saturated and becomes normal conducting.

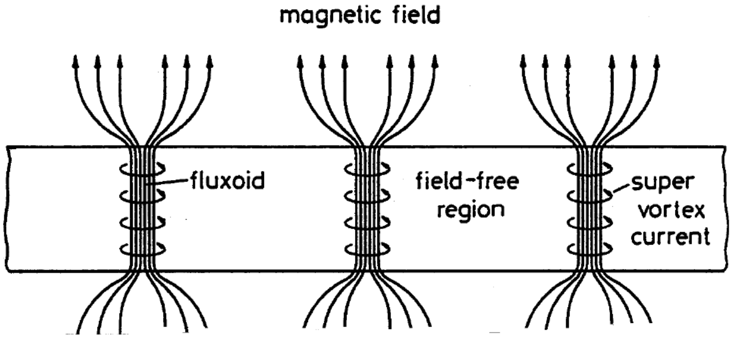

Figure 2.8: Non-uniformity of flux in Type II superconductor [46].

These parameters are for the DC case, both types have a critical RF magnetic field dependant on the maximum RF field that the material can support.

The RF critical field H_{rf} can exist in a metastable state above H_{c1}. The nucleation of fluxoids takes a comparably long period of time compared to the RF periods. This allows the magnetic field to be higher than that of the transition to the Meissner state.

For a typical niobium cavity, the maximum magnetic field is 0.23 Tesla, which in a Tesla-style elliptical cavity corresponds to an electric field of 55 MV/m. However, in mushroom-style cavities, peak fields of up to 145 MV/m have been achieved [43].

H_{c1} Lower critical magnetic field. The magnetic field below which a superconductor in the Meissner phase and the magnetic field is completely expelled. Above this value, the magnetic fields will start to enter a type II superconductor in a mixed state. For niobium this is $130 - 140\, mT$ at $4.2\, K$ [47].

H_{c2} Upper critical magnetic field. The magnetic field at which a superconductor in the mixed phase loses the last of its superconductivity and reverts to a normal conducting state. For niobium this is $\approx 270\,mT$ at $4.2\,K$[47].

H_c The thermodynamic critical magnetic field. The magnetic field at which the free energy of the superconducting state is equal to the normal state.

H_{rf} The RF critical magnetic field. The maximum RF magnetic field that the superconductor can support.

2.4 History of Deflecting and Crab Cavities

Crab cavities are in essence out-of-phase deflecting cavities. Deflectors are used for use in experimentation to separate beams of differing atomic particles, e.g. the Lengler structure [48], or separate beams of differing energy, e.g. the CEBAF structure [49]. The first deflectors were normal conducting, but the advent of superconducting deflectors soon took off due to their efficiency. The first compact deflector was the CEBAF four rod deflector that required a comparatively low frequency cavity in a very limited space region. Although proposed in 1988, it took over twenty years for the first crab cavity to become operational in an accelerator facility. This was the KEKB crab cavity. These structures will now be discussed in chronological order.

2.4.1 Lengler

The first deflecting structures used in accelerators were the CERN separators designed between 1963-1969. They were first designed by Bramham, Fortune and Montague [50] for separation of kaons and pions in the CERN bubble chamber particle beam. The design was chosen to operate at 2.855 Ghz in order to utilize the existing 20 MW klystrons. This design was chosen because of its similarities to the accelerating cavities and was manufactured by electroforming. The accelerating cavities had problems due to a narrow bandwidth and internal reflections that resulted in the deflector not being able to reach the required gradient, so a new structure was designed by Bernard and Lengler in 1969 [48] which aimed to double the achievable deflection.

The new Lengler design required a pass-band of several MHz in order to allow more sophisticated phase modulation, hence a disc-loaded wave-guide operating in a travelling wave mode was chosen, shown in Figure 2.9, as this technology was well understood. The phase advance for the modified design was chosen to be $\frac{2\pi}{3}$ as a compromise between the lower deflection at higher phase advances and shorter cell lengths for lower phase advances [48]. The cell dimensions were chosen to have an iris diameter of 47.146 mm and a cell radius of 117.328 mm. This gave the structure an R/Q of 16.4 MΩ/m and a group velocity of -0.0244 in the $\frac{2\pi}{3}$ mode, structure shown in Figure 2.9.

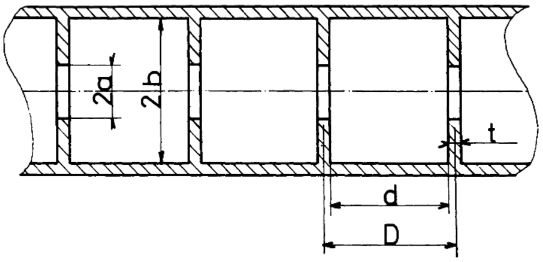

Figure 2.9: Cross section of the Lengler structure [51].

This led to the creation of a 100 cell cavity in order to have a transverse momentum of 22.65 MeV/c at a power of 17 MW. In order to keep the deflection locked in the horizontal plane, two rods were inserted into the cells near the equator in order to polarize the cavity and separate the two polarizations of the dipole mode separated in frequency by 30 MHz. These rods and the structure dispersion diagrams are shown in Figure 2.10. The mode separation between the operating mode and SOM is shown for a variety of operation phases. 0^omode refers to the operating mode, 90^omode refers to the SOM.

To reduce the internal reflections which were problematic for the original Montague structure, the structure manufacture and the input couplers were in-

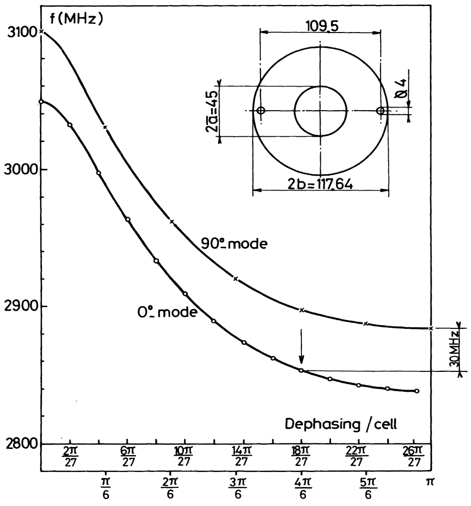

Figure 2.10: Cross section of the Lengler structure showing the position of metallic rods that were added in order to polarize the cavity and the phase shift between the modes over varying phase offsets[52].

vestigated. It was decided to machine each cell individually and braze each cell together. This allowed a better surface finish than electroforming and the possibility to individually check each cell prior to brazing. The couplers were redesigned to reduce the internal reflections. These reflections resulted from standing wave resonances building up in the cavity even though it was designed as travelling wave [52]. This is shown in Figure 2.11 with the choke to reduce RF leakage shown.

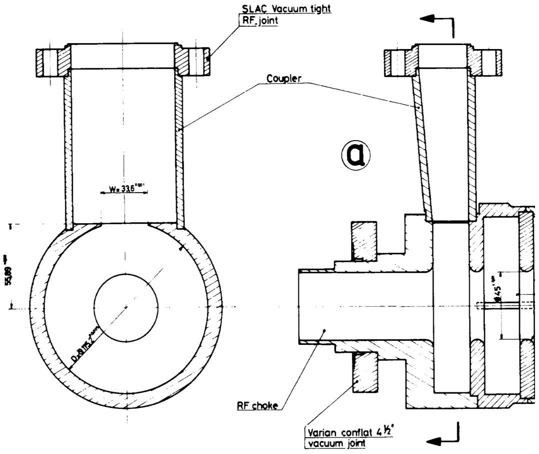

Figure 2.11: Schematic showing the position of the coupler at the end of the deflector as well as the RF vacuum joints[52].

In testing, this structure was limited by breakdown at the first iris next to the input coupler to a maximum electric field of $E_p = 522\frac{kV}{cm}$ [52].

Parameter	Value/Unit
Frequency of operational mode	2855 MHz
Operating mode	$\frac{2\pi}{3}$
Deflecting voltage V_t^a	160 kV/cm
Peak electric field E_p^a	480 kV/cm
R_t/Q	1376 Ω

Table 2.1: Key properties of the Lengler cavity.

2.4.2 CERN - Karlsruhe

The Karlsruhe cavity was designed and built in 1970's and was one of the first superconducting deflecting cavities constructed [53]. The decision to make the Karlsruhe deflectors superconducting was made due to conventional cavities being unable to produce the desired deflecting fields for the required length of time, mainly due to losses [54].

As design improvements progressed, the limit of materials was pushed. Due to concerns about the peak magnetic field on the previous lead surfaces the Karlsruhe deflectors were made out of solid niobium [55]. The location of the joints in the cavity required the cavity to operate in a $\frac{\pi}{2}$ mode, as this allowed for lower surface fields as every second cell has zero fields in a standing wave $\frac{\pi}{2}$ structure. Figure 2.12 shows one of the Karlsruhe cavities.

As the cavity operates with a standing wave unlike the travelling wave structures previously, ensuring that a pair of cavities remain at the same frequency is very important. As the RF power in travelling wave structures is being continually replaced, any frequency variation in one pulse should be corrected in the next, and provided two cavities are fed by the same source they will always be in phase. Standing wave structures build up power at the desired frequency and if one cavity shifts its fundamental frequency, via thermal expansion of the cavity, problems can arise. To stop this from happening, the frequency of the cavities must be carefully monitored and the status of any pair-

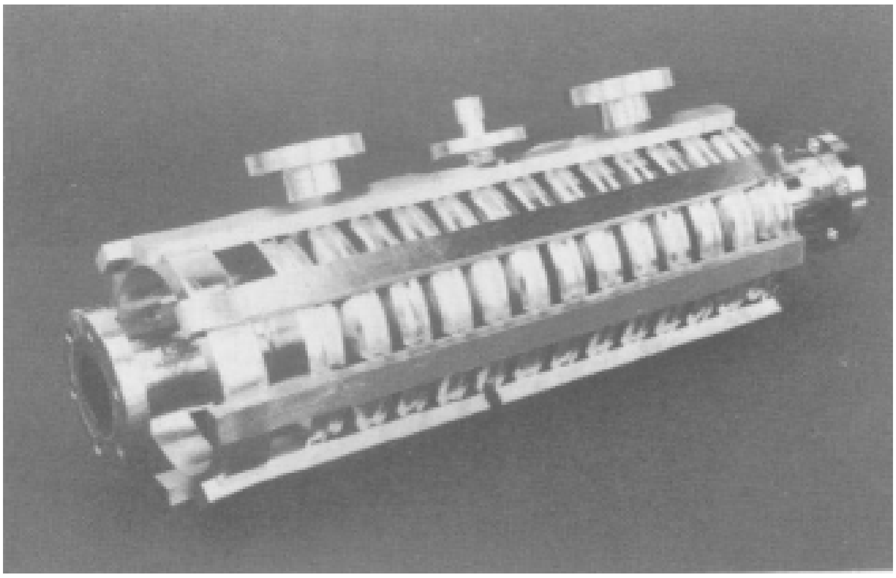

Figure 2.12: A picture of the Karlsruhe deflecting cavity. The couplers and mounting points can be clearly seen [51].

ings maintained. The Karlsruhe dipole cavities used tuning stubs to allow pairs of cavities to be kept at the same frequency [56, 57].

Parameter	Value/Unit
Frequency of operational mode	2855 MHz
Operating mode	$\frac{\pi}{2}$
Deflecting voltage V_t^a	2MV/m
Peak electric field E_p^a	0.2 MV/m
Peak magnetic field B_p^a	20 mT

Table 2.2: Key properties of the Karlsruhe cavity.

2.4.3 NAL

In 1973, an RF beam separator for NAL was designed [58, 59]. The seven cell cavity was machined from solid niobium to have elliptical cells operating at 8.665 GHz. Figure 2.13 shows the structure of the cavity, as well as the individual cells and couplers. The phase advance was chosen as a compromise between a high shunt and fabrication tolerances - the tolerances in the $\frac{2\pi}{3}$ are easier to meet than that of the π mode. To polarize the cavity, a slight elliptical cross section was used.

Unlike previous cavities that were hydro-formed, the decision was made to machine the cell components out of solid niobium. This removed the need for having high fields on a eb-weld. Instead, the welds could be located at the circumference join in the middle of the cell where the fields were much lower.

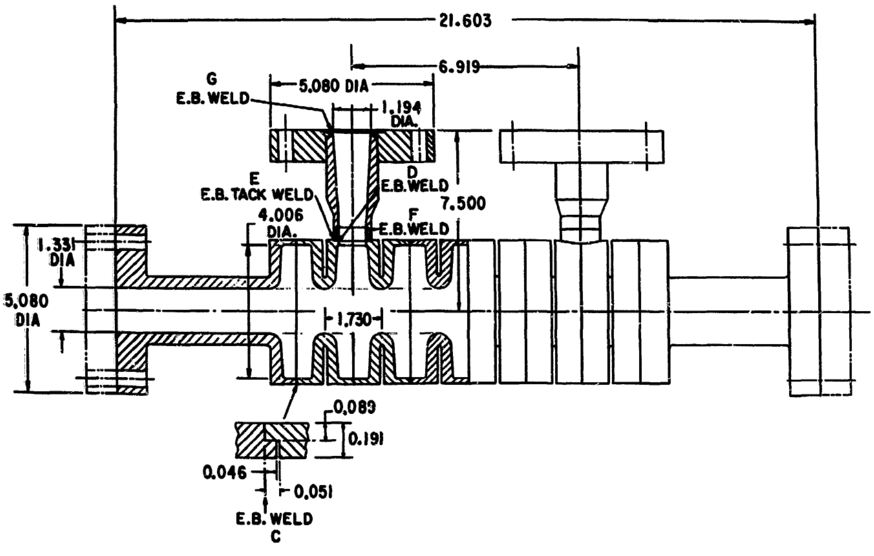

Figure 2.13: Schematic diagram of the BNL separator, with dimensions and the couplers shown. The half cell joins are also shown [51].

Parameter	Value/Unit
Frequency of operational mode	8.665 GHz
Operating mode	π
Deflecting voltage V_t^a	4.7 MV/m
Peak electric field E_p^a	17 MV/m
Peak magnetic field B_p^a	50 mT
R_t/Q	4730 Ω

Table 2.3: Key properties of the NAL cavity [59].

2.4.4 CEBAF

The Constant Electron Beam Accelerator Facility (CEBAF) required compact normal conducting RF structures to separate the beam for its three experimental halls. A compact structure was proposed [49] that consisted of four rods supporting a TEM dipole mode. The structure was taken from a $\frac{1}{4}$ wave resonator containing two central conductors rather than one. Figure 2.14 shows the rod layout within the structure.

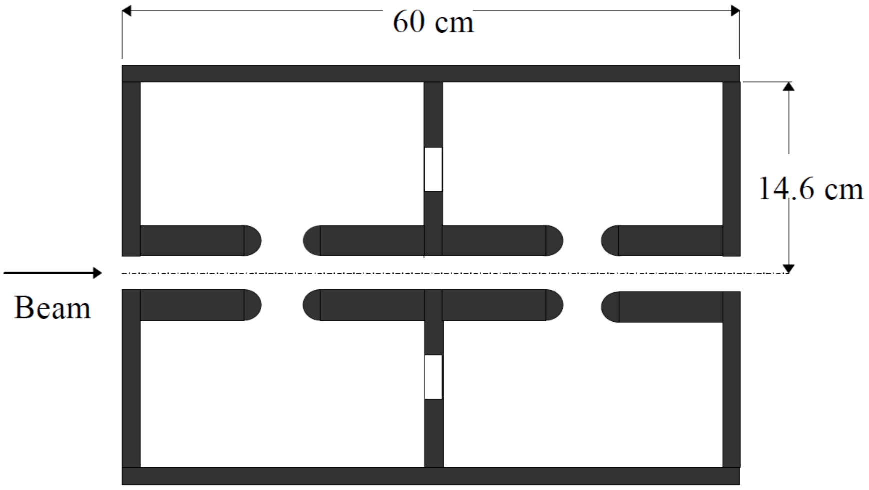

Figure 2.14: Schematic of the CEBAF deflector shown in the plane of the rods, the transverse size is only 14.6 mm where as a conventional deflecting crab cavity could be up to four times this size for the equivalent frequency[51].

With each rod's length being dependent on the desired frequency, the usual dependence on outer radius that a standard pillbox cavity exhibits is removed, allowing the cavity to have a considerably reduced outer radius for an equivalent frequency. A pair of straight rods with no central gap cannot be used as this would eliminate and E_z field components. Electric field in the z direction is needed for deflection as shown in Section 2.1.1. The rods have the added benefit of compressing the desired field into the centre of the cavity and increasing the transverse shunt impedance $R_\perp$ [60].The RF separators are used in two configurations, either to split a portion of the beam off the recirculating linac and into one of the experimental halls, or to divide the beam into 3 for the separate experimental halls.

Due to machine protection concerns, primarily due to limitations on the beam current each experimental hall can receive, phase stability between the injector and the separators is closely measured. If the phase difference exceeds the predefined limits, the beam can be shut down [60].

The unusual and compact shape was needed for the CEBAF deflector due to space requirements within the accelerator facility. There was not enough space to fit a pillbox style 500 MHz cavity in the space available. An equivalent pillbox cavity would have had an outer radius of at least 300 mm, but the 4 rod design shrunk this to less than 150 mm.

Tuning of the cavity was accomplished by flaps that could be moved into the cavity from the equator, closing the distance between the rods and the outer wall. Power was coupled in using a klystron output coupler from the end flanges. Figure 2.15 shows the CEBAF separator on a test stand along with its water cooled input coupler, tuners and monitoring probes. To ensure flexibility of operation while also standardizing parts, the cavities were fabricated in modular elements.

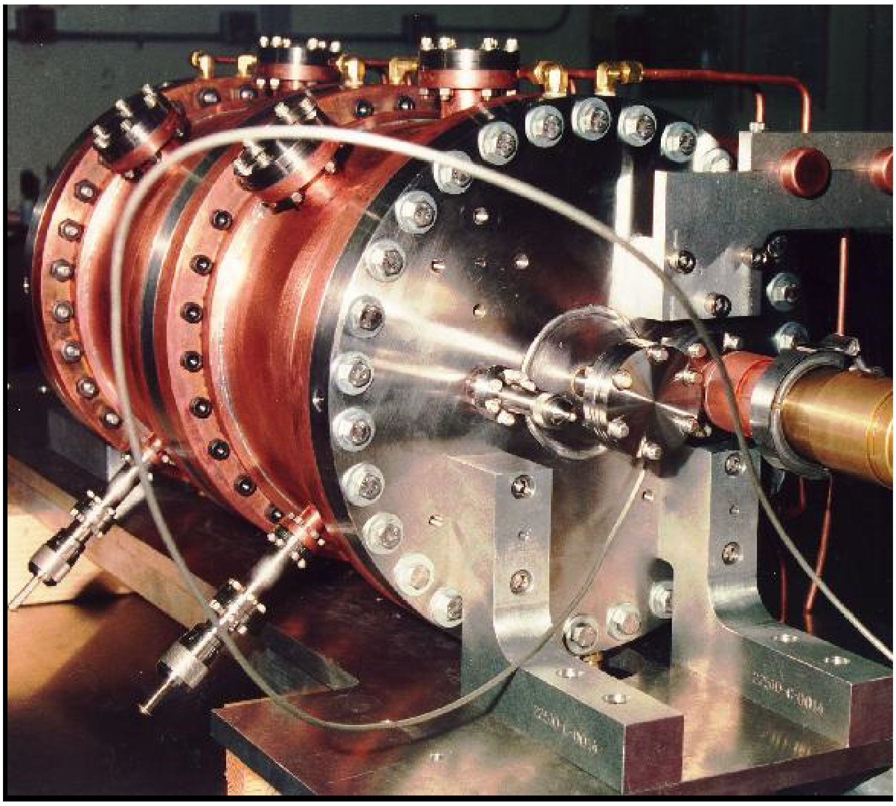

Figure 2.15: CEBAF separator on a test stand[51].

The cavity design could be mathematically approximated to that of a quarter wave resonator with some modifications [49]. As the properties of a quarter-wave resonator can be calculated using equivalent circuits, it was possible to make a similar approximation for this four rod cavity.

Many of the properties of the cavity can be calculated. However, due to the initial calculations by C. Leeman and Yao [49] not including the capacitance at the ends of the rods between two opposing rods, the model only holds for a limited region.

The transmission line model assumes that each rod can be at a different potential and as such, TEM modes can exist around them. The potential difference between the rods act as a capacitance, while the magnetic field caused by the current flowing along them creates self-inductance. Thus aN equivalent circuit and set of formulas can be generated for the two wire line [61, 62].

Figure 2.16: Two rod transmission line, each rod has radius R and the mid points of the rods are separated by a distance of 2A

The charge distribution on each wire depends on the relative position of the wires. Figure 2.16 shows the layout of the two conductors, each of radius R separated by a distance of 2 A. The charge in each wire will cause an image charge in the other, redistributing the surface charge of the wire and shifting the effective point charge locations closer together. As the wires move closer together this shift will have a greater effect.

The position and effect of these charges can be calculated from Gauss's law of a cylindrical surface. If we assume that the line charge is infinite and uniform along its length with a charge per unit length of λ, and Gauss's law is applied as a cylinder around the line charge, then:

$$\int\int E \cdot da = \frac{q_{enc}}{\epsilon_0} \tag{2.66}$$

where $\lambda = \frac{q_{enc}}{l}$ and $q_{enc}$is the enclosed charge and l is the length of the enclosing cylinder, thus:

$$E \cdot 2\pi r = \frac{\lambda}{\epsilon_0} \tag{2.67}$$

$$E = \frac{\lambda}{2\pi r \epsilon_0} \tag{2.68}$$

where r is the radius of the cylinder, though this only holds if $r > R$.

By integrating this, the potential can then be found:

$$\phi = \int E \cdot dr = \frac{\lambda}{2\pi\epsilon_0} \ln\left(\frac{b}{r}\right) + const \tag{2.69}$$

where b is an arbitrary point that we can and will choose to have a potential of zero. Again, this only holds for $r > R$, but this also allows the wire to be treated as a line charge as there is no longer a dependence on R.

This can then be combined with a second oppositely-charged line, which is placed a distance 2A away from the initial wire.

$$\phi = \frac{\lambda}{2\pi\epsilon_0} \ln\left(\frac{1}{r_1}\right) - \frac{\lambda}{2\pi\epsilon_0} \ln\left(\frac{1}{r_2}\right) \tag{2.70}$$

where r_1 and r_2 are the radii of the two cylinders.

$$\phi = \frac{\lambda}{4\pi\epsilon} \ln\left(\frac{r_2^2}{r_1^2}\right) \tag{2.71}$$

This can then be simplified using:

$$a = \sqrt{(A^2 - R^2)} \tag{2.72}$$

where a is the distance between the mid point of the wire and the effective charge location, A is the distance between the mid point of the wires and the centre of a wire and R is the radius of a wire. In the case where $A \gg R$, we can assume that $a \approx A$. Thus the voltage between the two wires is given as:

$$V = \frac{\lambda}{2\pi\epsilon_0} ln\left(\frac{A+a}{A-a}\right) \tag{2.73}$$

Thus the capacitance between the two rods can be calculated as:

$$C = \frac{q}{V} = \frac{2\pi\epsilon_0}{\ln\left(\frac{A+a}{A-a}\right)} = \frac{\pi\epsilon_0}{\ln\left[\frac{(A^2+a^2)}{A^2-a^2}\right]} = \frac{\pi\epsilon_0}{\ln\left(\frac{(A+a)}{a}\right)} \tag{2.74}$$

This can then be rearranged using $a = \sqrt{(A^2 - R^2)}$, $\alpha = \frac{A}{R}$ and the relationship:

$$\cosh^{-1} x = \ln\left(x + \sqrt{x^2 - 1}\right) \tag{2.75}$$

becomes:

$$\ln\left(\frac{A+a}{A-a}\right) = \cosh^{-1}(\alpha) \tag{2.76}$$

Thus the capacitance becomes:

$$C = \frac{\pi\epsilon_0}{\cosh^{-1}(\alpha)} \tag{2.77}$$

Similarly, the inductance becomes[63]:

$$L = \frac{\mu_0}{\pi} \cosh^{-1}(\alpha) \tag{2.78}$$

Hence the impedance becomes:

$$Z_1 = \sqrt{\frac{\mu_0}{\epsilon_0}} \frac{1}{\pi} \cosh^{-1}(\alpha) \tag{2.79}$$

assuming:

$$Z_1 = \frac{\omega L}{k} = \sqrt{\frac{L}{C}} \tag{2.80}$$

Instead of having two concentric conductors, it is possible to have a pair of similar rods that act as the two conductors, each with different potentials.

The equivalent circuit for the four rod structure is simplified by assuming the capacitance between the two adjacent rods is far greater than the capacitance between either rod and the walls of the cavity, thus the walls are ignored. The second facing pair of rods are simplified by assuming a symmetry plane as shown in Figure 2.17

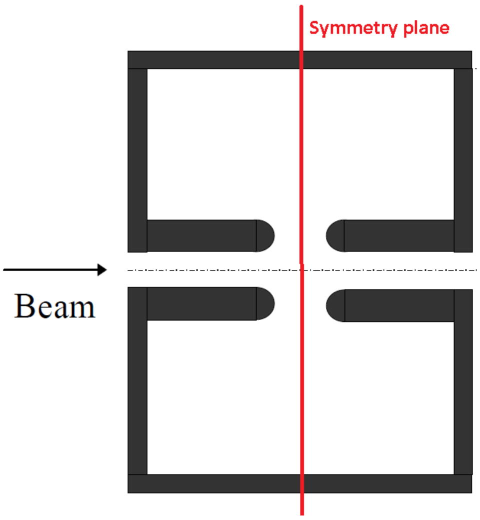

Figure 2.17: Side view of a four rod cavity, with the mirror plane shown as a dotted line.

As previously calculated, this means the capacitance between the two rods is given as:

$$C = \frac{\pi \epsilon_0}{\cosh^{-1}(\alpha)} \tag{2.81}$$

The inductance given as:

$$L = \frac{\mu\mu_0}{\pi}\cosh^{-1}(\alpha) \tag{2.82}$$

The peak electric field will again be dependant on the maximum voltage between two points over a given distance, however this could be between the tips of two parallel rods, or between two facing rods, depending on the distances involved.

At the ends of the rods the maximum electric field will still be:

$$E_{max} = \frac{V_0}{d} \tag{2.83}$$

where d is the distance between the tips

However this is likely not to be the case. To calculate the electric field at the surface of the rods between two adjacent parallel rods, the voltage between them must be calculated. The potential difference at the end of the rods is known to be $\pm V_0$, and as such the voltage a distance z down the rod will be given as:

$$V_p = V_0 \sin(kz) \tag{2.84}$$

where V_0 is the maximum voltage through the tip, k is the wave number, z is the distance down the rod.

From this the charge per unit length q can be calculated [63]. Equation 2.85 can then be rearranged and placed in Equation 2.87. This can then be used to calculate the electric fields at the surface where $x = A - R$ or the transverse electric field where $x = 0$.

$$V_{(x,y)} = \frac{q}{4\pi\epsilon_0}\ln\left(\frac{r_-^2}{r_+^2}\right) \tag{2.85}$$

$$E_x(x,y) = -\frac{\partial V}{\partial x} \tag{2.86}$$

$$= -\frac{aq}{\pi\epsilon_0}\left[\frac{x^2-a^2-y^2}{r_-^2 r_+^2}\right] \tag{2.87}$$

where A is the rod separation, R is the rod radius, $a = \sqrt{A^2-R^2}$, $r_- = \sqrt{x^2-a^2}$, $r_+ = \sqrt{x^2+a^2}$

Using the relation $H = \frac{E}{Z_c}$, the magnetic field can then be calculated. Once the transverse electric and magnetic fields are known, the transverse voltage can be calculated from:

$$V_{trans} = \int_0^l \left[E_{trans}\sin(kz)e^{ikz} + cB_{trans}\cos(kz)e^{ikz}\right]dz \tag{2.88}$$

Where l is the length of the rod in the z direction and E_{trans} and B_{trans} are the transverse electric and magnetic field components calculated previously.

As there is no current flow across the gap at the end of the rod, it is easier to work with only the energy stored magnetically, as the inductance only has one component, rather than two in the case of the electric fields.

We know:

$$U = \int LI^2 dz \tag{2.89}$$

$$I(z) = I_L\cos(kz) \tag{2.90}$$

$$I_1 = \frac{V_1}{Z_1} \tag{2.91}$$

We can rearrange this to get:

$$\begin{aligned} U &= \int LI^2 dz && (2.92) \\ &= LI_1^2 \int \cos^2(kz)dz && (2.93) \\ &= L\frac{V_1^2}{2Z_c^2}\int_0^l \cos^2(kz) && (2.94) \\ &= L\frac{V_1^2}{2Z_c^2}\left(\frac{l}{4}+\frac{1}{4}\sin(kl)\right) && (2.95) \end{aligned}$$

Where l is the actual length of the rod, which is not $\frac{\lambda}{2}$ but is very close to and can be calculated as shown earlier.

The integral can be simplified as the initial conditions mean $\frac{x}{2}+\frac{1}{4}\sin(2x)=0$ when $x=0$. If the rod length was to be $\frac{\lambda}{2}$, then then the additional dependence on $\sin(kl)$ would also disappear.

The R/Q of the cavity can be calculated as:

$$\frac{R}{Q}=\frac{V_0^2}{2\omega U} \tag{2.96}$$

2.4.5 KEKB

The KEKB dipole cavity is the first super-conducting crab cavity implemented and operated on a working facility. The crab cavities were added to the electron-positron collider to eliminate any beam-beam instabilities caused by synchrotron-betatron oscillating[2] and reduce loss of luminosity caused by geometrical effects. The cavity is of a non-axially-symmetric squashed cell shape, often called 'racetrack'. The racetrack shape, characterized by its two linked semi-circles provides polarization of the cavity by shifting the SOM to a different higher frequency [64]. Figure 2.18 shows part of the structure, including

---

[2] Synchrotron oscillation are the motion of of particles longitudinally within the bunch, betatron oscillations are the harmonic motions of the particles transverse to the direction of propagation.

both the input coupler and the specially-designed coaxial coupler that removes both the lower order accelerating mode (LOM) and some higher order modes. In a crab cavity, the first mode of the cavity is not always the operating mode. This is usually equivalent to the accelerating mode of a pillbox cavity. As the KEK-B cavity is a standard single cell cavity, the deflecting mode is not the fundamental mode. The TM_{010} mode is very prominent, thus the cavity needs strong damping [65]. To meet these requirements a hollow cylindrical coaxial coupler was developed that was contained within the beam pipe. The coupler was designed to damp the accelerating mode of the cavity as well as provide coupling to some HOM's. The inclusion of a notch filter to reject the operating mode is included, as the crabbing mode can couple to the coaxial coupler as a TEM mode. The frequency-shifted SOM has its cut-off raised above that of the coaxial beam-pipe, allowing it to propagate and be extracted at the RF absorber at the end of the coaxial pipe [66]. Other HOM's could be extracted out of the large beam-pipe due to being above cut-off [67].

The cavity was formed from 5 mm niobium. This was hydro-formed into shape and e-beam welded. The walls were required to be at least 4 mm thick to withstand the external pressure of 0.13 MPa, and additional reinforcing ribs were added to reduce stress around the iris. Special care was taken to remove excess hydrogen deposited by electropolishing, as this caused a significant drop off in operating Q during prototype testing. A high temperature bake-out[3] could not be used during initial testing due to indium joints. After several rounds of cleaning and processing, the cavity was able to exceed its upper design gradient of 21 MV/m and reached 36 MV/m [66].

---

[3] A high temperature bake out involves raising the temperature of the cavity and attached components in a vacuum to $700^o \sim 1200^o$ C to allow gasses trapped in the surface to escape.

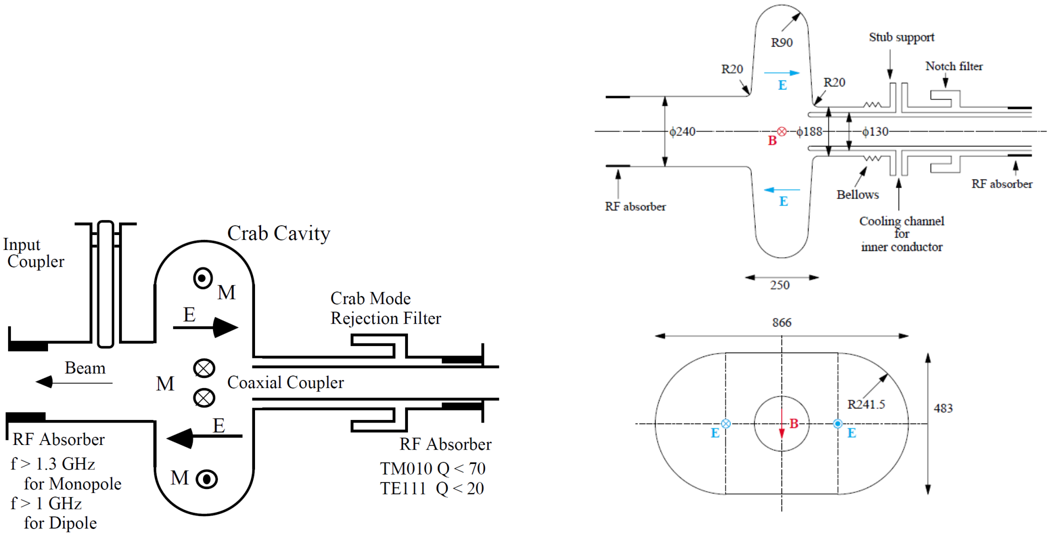

(a) (b)

Figure 2.18: Schematic of the KEK-B deflecting cavity, both the input coupler and the coaxial damper are shown[51].

Parameter	Value/Unit
Frequency of operational mode	508 MHz
Operating mode	π
Deflecting voltage V_t^a	1.41 MV/m
Peak electric field E_p^a	14.4 MV/m
Peak magnetic field B_p^a	8.17 mT
R_t/Q	48.9 Ω

Table 2.4: Key properties of the KEKB cavity.

2.5 Other LHC Crab cavities

To be compact, a TEM-like structure is needed.

There are a limited combination of structures that exist that can support a suitable TEM wave. A brief summary of all the designs at present follows below. In all diagrams the design is split into electric field profiles and magnetic field profiles. The fields are arbitrary but represent the operating mode of the cavity demonstrating their position within the cavity.

Quarter Wave

A quarter wave structure consists of a single conductor approximately $\frac{1}{4}\lambda$ long, inside a vacuum can. The beam passes across the end of the conductor as shown in Figure 2.19. This shape has inherent asymmetries that must be compensated for, usually with an opposing plinth to reduce the longitudinal voltage. The cavity is extremely compact in both the beam direction and vertical direction. In the horizontal direction, the cavity is constrained by the length of the $\frac{1}{4}\lambda$ resonator and and the plinth. Due to the beam passing across the tip of the conductor, there is some longitudinal field present that will cause acceleration in the deflecting mode. This can be seen in Figure 2.19a, where there is field in the beam-pipe region that is not transverse to the beam direction. The magnetic field circulates the main central conductor, as can be seen in Figure 2.20.

This type of deflector was first proposed by Ilan Ben-Zvi [68], and is undergoing further study.

Half Wave

A half wave structure consists of one or two conductors approximately $\frac{1}{2}\lambda$ long. Although one conductor could be used, this would create very large asymmetrical properties within the cavity. As such, two conductors would be used. The two conductors could either run parallel or perpendicular to the

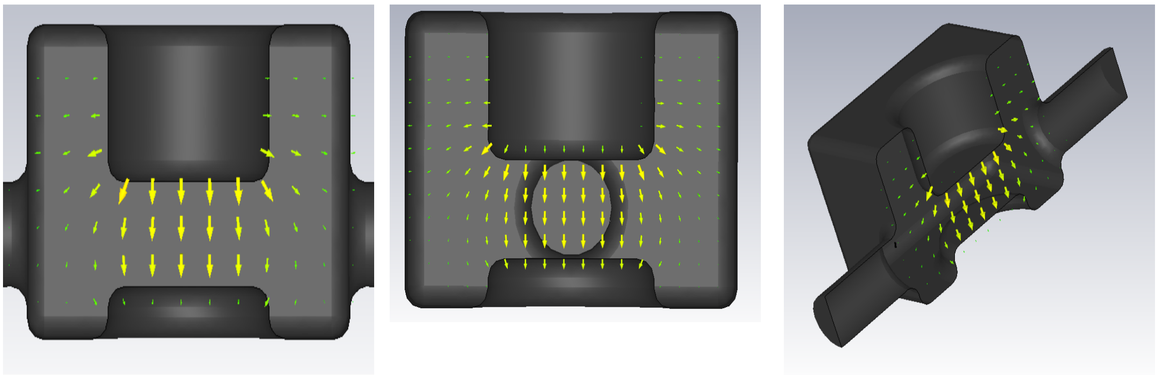
(a) (b) (c)

Figure 2.19: Quarter wave deflector electric field.

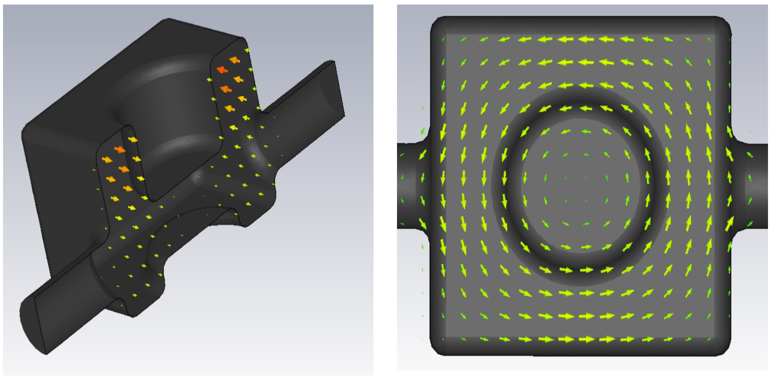
(a) (b)

Figure 2.20: Quarter wave deflector magnetic field.Arrow size is proportional to field strength,

beam line. If the conductors run parallel to the beam line, the electric and magnetic field components cancel out the kick received by the beam. By having the conductors perpendicular to the beam, the kick is generated by the electric field, as the beam passes through the centre of the cavity. This can be seen in Figure 2.21. The magnetic fields are confined to the ends of the rods where they join the cavity body and circulate the rods as shown in Figure 2.22. The cavity is again very compact in the direction of the beam, however the horizontal direction requires space for the conductors so it is limited on how compact it can be. The vertical direction contains the $\frac{1}{2}\lambda$ conductors and as such is fixed at this dimension.

This structure was proposed by J. R. Delayen [63] and underwent several iterations.

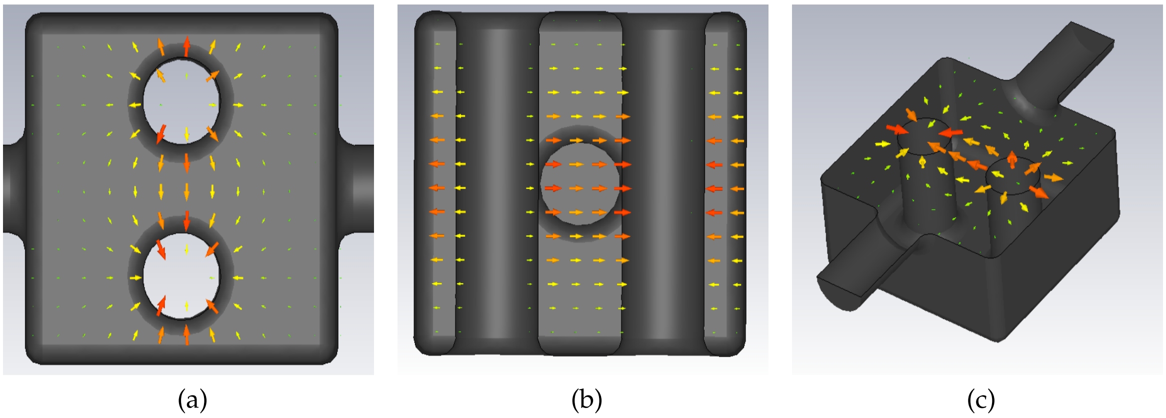
(a) (b) (c)

Figure 2.21: Half wave deflector electric fields.

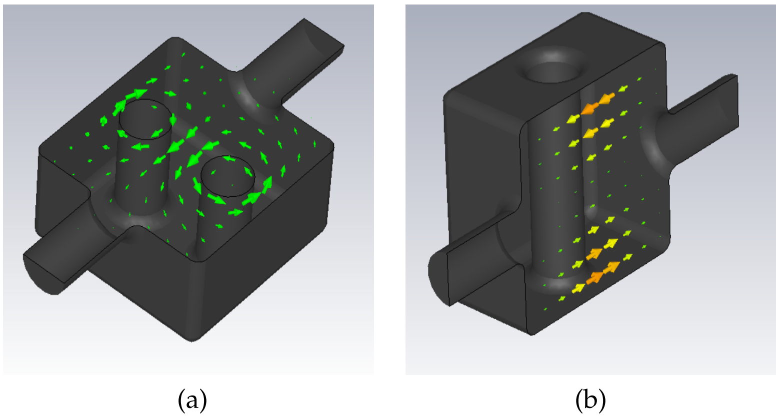
(a) (b)

Figure 2.22: Half wave deflector magnetic fields.

Ridged Waveguide

By placing a ridge in a piece of waveguide, its cut-off frequency can be lowered. To use this as a deflecting cavity, the waveguide is oriented such that the ridge lies in the desired plane of deflection. The electric field then provides a transverse kick to the bunch, as shown in Figure 2.23. The magnetic field circles round the ridge, as shown in Figure 2.24. This cavity is highly compact in both transverse directions, as the transverse dimensions are not an important factor of the components of the cavity. The cavity is highly dependent on the longitudinal length as the ridge in the cavity is $\sim \frac{1}{2}\lambda$long. As the cavity requires some longitudinal electric field, there is a gap between the ridge and the end of the cavity. This results in the being the largest in the longitudinal direction of the four compact crab cavities proposed. The half wave cavity was abandoned in favour of this design, circa 2011, as the half wave cavity evolved into a ridged waveguide shape[69].

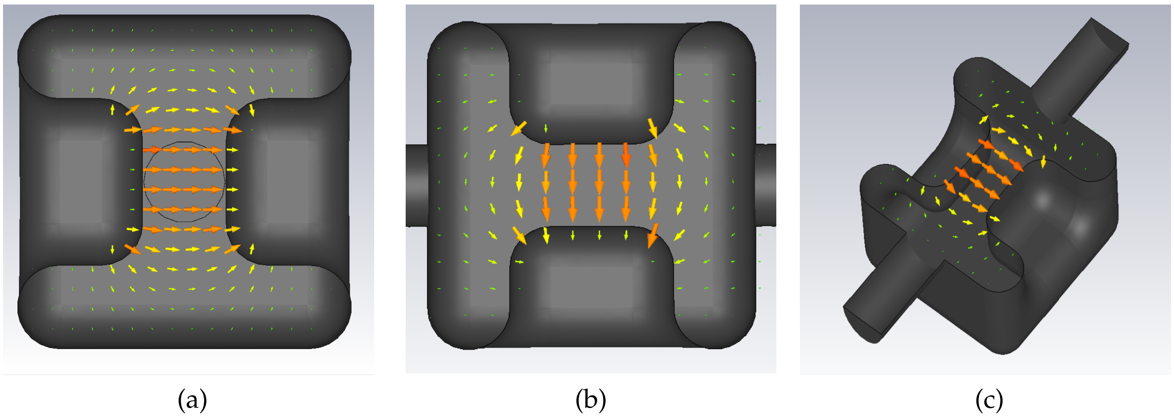
(a) (b) (c)

Figure 2.23: Ridged waveguide deflector electric fields.

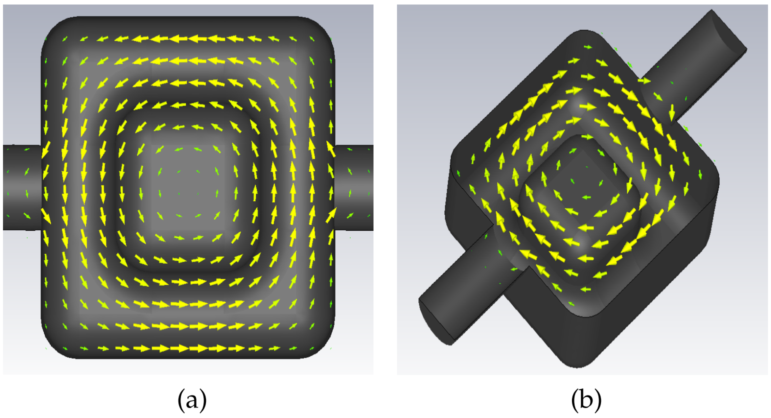
(a) (b)

Figure 2.24: Ridged waveguide deflector magnetic fields.

Four Quarter Wave

A four quarter wave resonator consists of 4 $\frac{1}{4}\lambda$ rods arranged parallel to the beam direction. This layout is similar to a $\frac{1}{2}\lambda$ resonator, but with the conductors parallel to the beam direction, with a gap halfway along the conductors as seen in Figure 2.25. The inclusion of a gap allows for a longitudinal electric field component and thus deflection. The electric fields at the tips of the rods point in opposite directions as seen in Figure 2.25. This emulates a dipole mode in a pillbox cavity. The magnetic field circulates the rods as seen in Figure 2.26, with its peak near the base of the rods.

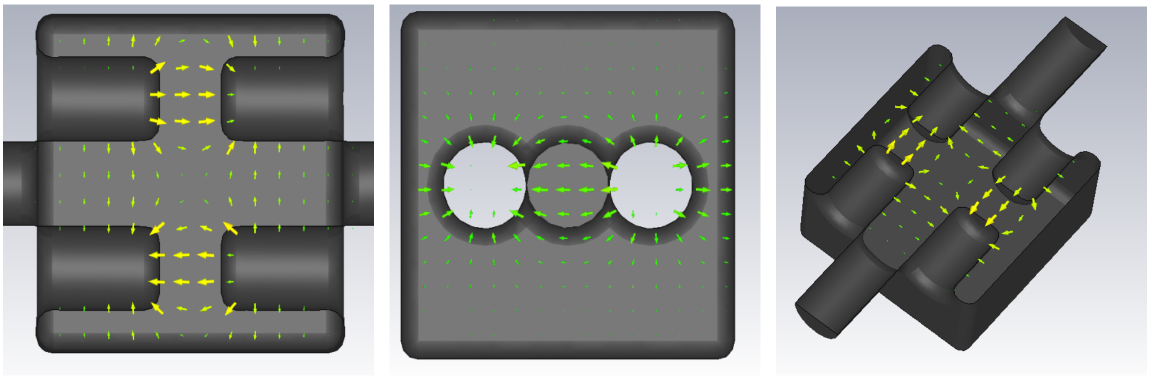
(a) (b) (c)

Figure 2.25: Four quarter wave deflector electric fields.

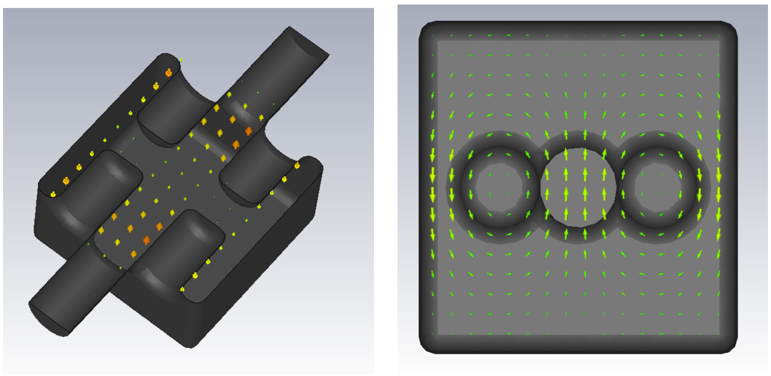
(a) (b)

Figure 2.26: Four quarter wave deflector magnetic fields.

Unlike the other three cavities previously discussed, the 4 $\frac{1}{4}\lambda$ cavity (4RCC) has a LOM. There are also two HOM's that are of interest as they are close to the operating mode. The fields for the LOM are shown in Figure 2.27. The electric fields at the tip of both rods point in the same direction, emulating an accelerating mode of a pillbox cavity. The magnetic field circles both conductors.

The first HOM is similar in appearance to the deflecting mode, and has oppositely-charged parallel rods. However, there is no flip in the electric potential. This leads to very low longitudinal fields and, as such, little interaction with the beam. The magnetic field circles the base of the rods similar to the deflecting mode, but is in opposite directions at each end of the cavity.

The second HOM has the tips of all rods at the same potential, and interacts with the outer can. The magnetic field circulates the four rods. This results in

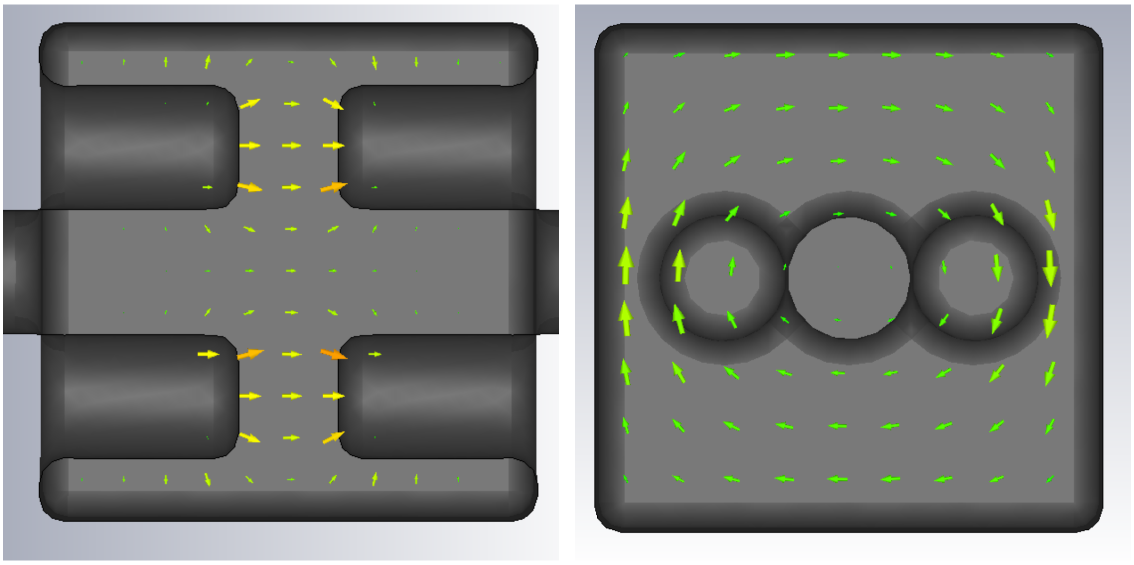
(a)

(b)

Figure 2.27: Electric (a) and Magnetic (b) fields for the LOM in the 4RCC.

the beam having almost no interaction with this mode.

These four modes represent the four unique charge configurations that the rods can support. The presence of a LOM is of some concern as it could interact with the beam, however it is believed that the mode can be suitably damped. This will be studied in further detail in 8.

The kick provided by the cavity is from both the electric and magnetic fields as a bunch passes though the cavity. This results in a slight transverse offset compared to the nominal position of the beam. This transverse offset arises as the ideal bunch has transverse momentum added and then removed, rather than than passing through at field null.

The deflecting and crabbing kicks are shown in Figure 2.30.

However, this transverse offset is on the order of $0.5 \cdot 10^{-8}$ m, which is believed to be small enough to not be of concern [70].

The cavity is very compact in the vertical direction and again limited by the conductors in the horizontal direction. As the $\frac{1}{4}\lambda$ conductors are in the direction of the beam, the cavity is fixed in this direction. This design was first used as the CEBAF deflector [49] and has been operated successfully since. This thesis will examine this type of structure.

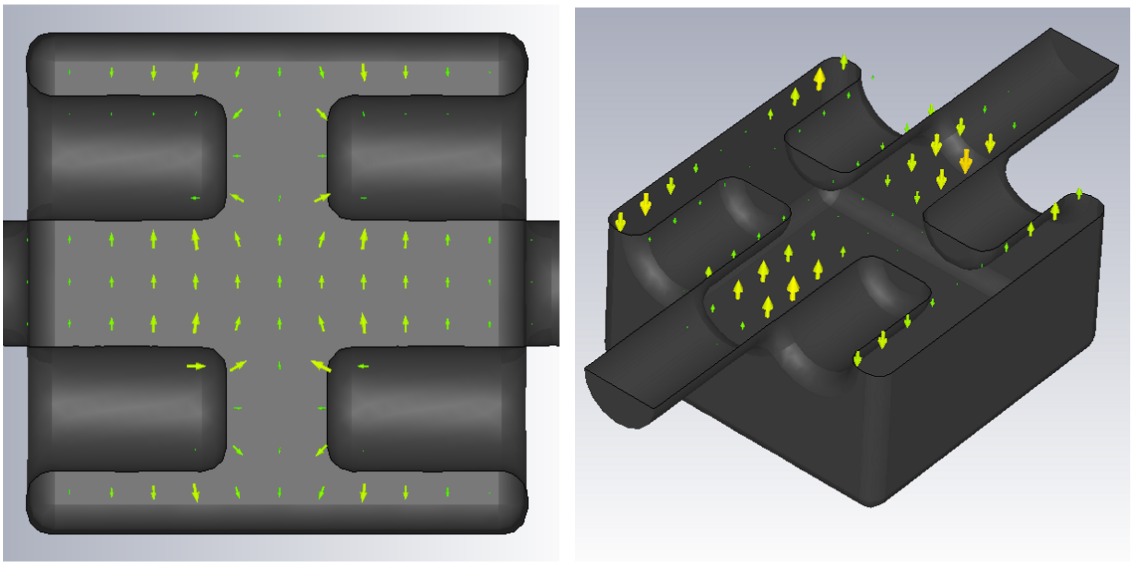

(a) (b)

Figure 2.28: Electric (a) and Magnetic (b) fields for the first HOM in the 4RCC

In the original CEBAF design, no account was made for the capacitance at the end of the rods. This can be modelled as a capacitor between the terminals of the equivalent circuit and give an impedance of:

$$Z_2 = \frac{1}{i\omega C_2} \tag{2.97}$$

thus:

$$Z_c(l) = \frac{1}{i\omega C_2} + iz_0 \tan(kz) \tag{2.98}$$

The capacitance at the end of the rod can be determined by the dimensions of the rod and the size of the gap, similar to any other plate capacitor, thus:

$$C_2 = \frac{\pi \epsilon_0 R^2}{2G} \tag{2.99}$$

where R is the radius of the rod and $2G$ is the distance between the end of a rod and its opposing rod face. However, during simulations it was noted that at large gap sizes, the simulations were diverging from the expected results.

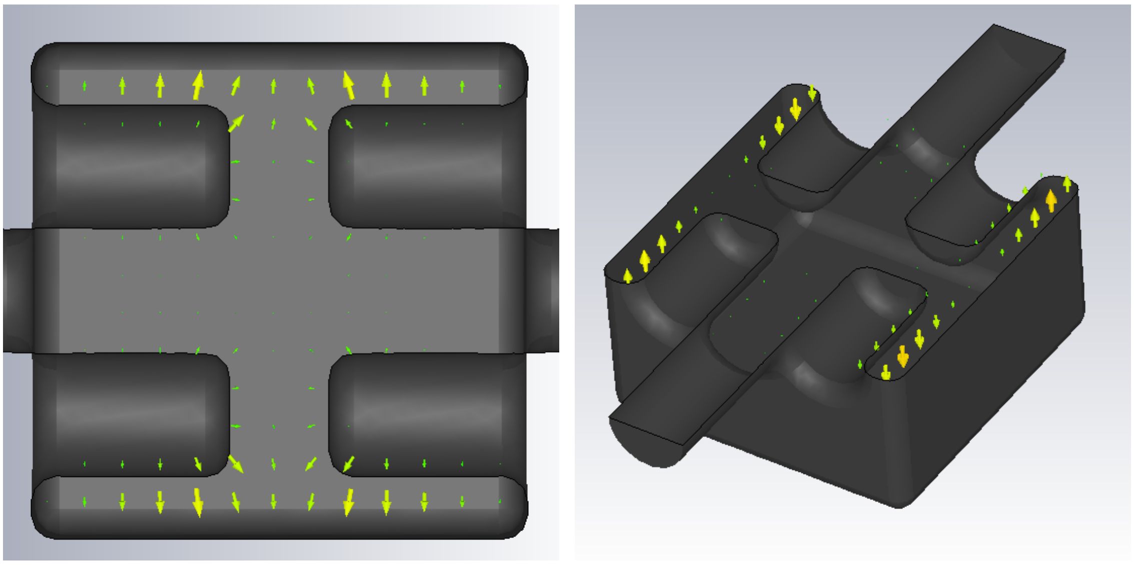
(a) (b)

Figure 2.29: Electric (a) and Magnetic (b) fields for the second HOM in the 4RCC

Increasing C_2 by a factor reduced this error. Thus the effective surface area of the capacitor needed to be increased with increasing gap. This increase can be attributed to the fringing fields that are present when the gap of a disk capacitor is similar in scale to the radius of a plate, thus:

$$C_2 = \frac{\pi\epsilon_0(R+G)^2}{2G} \tag{2.100}$$

To calculate the length of the cavity one starts with the the equations for the equivalent circuit:

$$Z_c = \frac{1}{i\omega C_2} + iZ_0\tan(kz) \tag{2.101}$$

$$k = \frac{2\pi}{n\lambda} \tag{2.102}$$

$$Z_1 = \sqrt{\frac{L}{C_1}} \tag{2.103}$$

$$\omega = \frac{2\pi c}{\lambda} \tag{2.104}$$

We then calculate the admittance of the circuit $Y_{aa} = \frac{1}{Z_c}$

$$Y_{aa} = \frac{2\pi c C_2}{\lambda} + \frac{1}{Z_1 \tan(\frac{2\pi}{\lambda} l)} \tag{2.105}$$

where, c is the speed of light, C_1 is the capacitance of the rod to the cylinder along its length, C_2 is the capacitance at the end of the rod, L is the inductance of the rod, λ is the desired frequency and l is the length of the rod.

By setting Y_{aa} to zero we are able to calculate the length of the rod and henceforth the total length of the cavity, as the frequency and gap will have been chosen before hand. Once the length is known, the internal energy can be calculated.

2.6 Conclusion

Crab cavities are RF cavities that provide a transverse rotation to bunches that pass though them by giving equal and opposite kicks to the front and back of the bunch.

The deflection from a crab cavity can be calculated using Panofsky-Wenzel theorem. This theorem allows the deflection of a particle normal to the direction of travel to be calculated from the electric field in the direction of travel.

Superconducting cavities have very low resistance and high quality factors, enabling them to operate with very low losses to the walls of the cavity. This is useful when the cavity is operating continually as it reduces the wasted power and heating load making the whole experiment more efficient.

Crab cavities are in essence out-of-phase deflecting cavities. Deflectors have been used to separate beams of differing atomic particles for many years. The CEBAF structure was the first compact deflector used in experimentation, and can be modified for use as a crab cavity. The first operational crab cavity was the KEKB crab cavity that demonstrated crabbing as a means of recovering luminosity loss from geometric overlap.

For the LHC, there is extremely limited space and this requires a compact cavity design. There are four main designs that could be used to fulfil the LHC requirements. The four quarter wave design based on the CEBAF deflector will be the focus of this thesis.

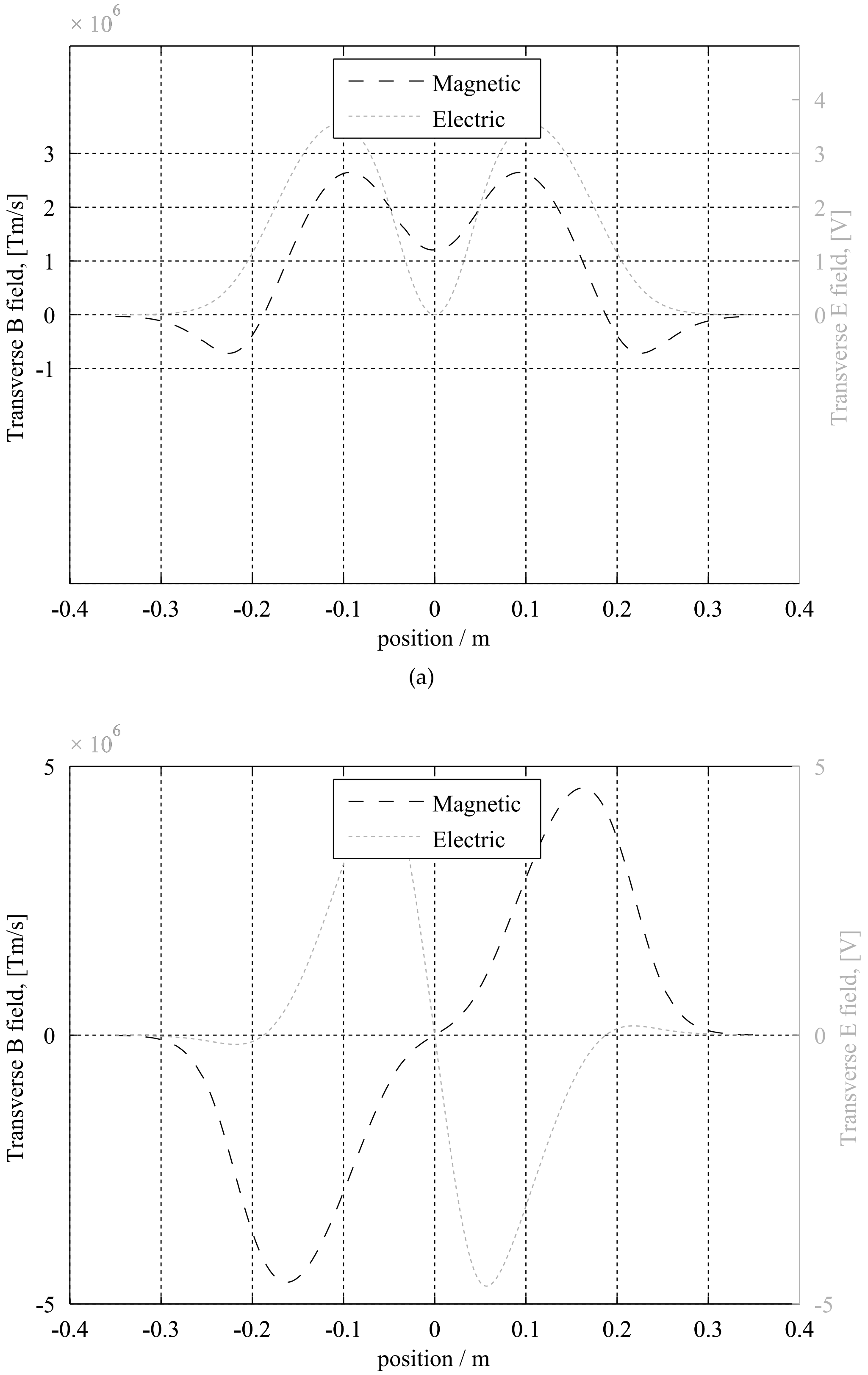

(a)

(b)

Figure 2.30: Fields seen by the beam in deflecting (a) and crabbing (b) phases.

Chapter 3

CST Cavity Modelling

3.1 Introduction

For the upgrade in 2020, the LHC requires a new style crab cavity. Due to the desired position within the LHC of the crab cavities, a normal cylindrically-symmetric cavity is not viable. The initial LHC space requirements given by CERN state that the beam-pipe must be at least 50 mm, but the outer radius can be no more than 150 mm. This is due to the close proximity of the second beam-pipe. This limited space is shown in Figure 3.1. The desired operating frequency of 400 Mhz would require a cylindrically-symmetric cavity of approximately 350 mm radius. A new design compact four-rod crab cavity (4RCC) was optimized to fulfil these requirements.

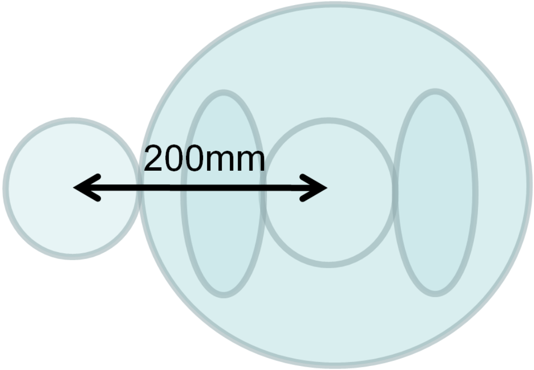

Figure 3.1: Space available for the LHC crab cavity. Centre to centre separation is 200mm with 50mm beam-pipes allowing 150mm for cavity radius.

The Constant Electron Beam Accelerator Facility (CEBAF) required compact normal conducting RF structures to separate the beam for its three experimental halls. A compact structure was proposed[49] that consisted of four rods supporting a TEM dipole mode. This cavity was chosen as a base for the LHC design as it offered a number of benefits;

- A deflector uses the same mode as a crab cavity, but 90 degrees out of phase.
- The design can be relied upon to work as the deflector has operated reliably for many years.
- The design is compact compared to an equivalent cylindrically-symmetric cavity

The CEBAF deflector is designed to work at normal conducting temperatures and deflect electrons, so for the LHC a redesign is needed.

In the design of superconducting RF cavities, surface fields need to be kept as low as possible while remaining balanced so that neither field dominates the performance of the cavity. The peak surface electric field is important because electrons can be emitted through field emission from the surface of the cavity, accelerated by the RF field, and collide with a different surface causing localised heating. Likewise, the superconducting surface of the niobium can only support a given value of magnetic field before it quenches. The LHC requires that the peak fields remain below 80 mT and 50.0 MVm^{-1} to avoid such an issue. These numbers are set lower than the values expected from actual operation to allow for surface defects during manufacture. As such, the peak surface electric and magnetic fields will be of primary concern during optimisation. The R/Q in the 4RCC is very high, as the fields are confined near the rods, thus the stored energy for the cavity is very low for a given voltage. As a result, R/Q will not be optimised.

CST Microwave Studio was used to simulate and partially design the cavity. CST Microwave Studio[71] is a conformal rectangular mesh, 3D FIT electromagnetic solver that is highly regarded and bench-tested as a reliable simulator of RF designs. Due to some limitations in the CST MWS drawing package SolidWorks[72] was used for some of the design as it provided a more robust drawing platform that could cope with complex geometry. SolidWorks is a 3D CAD drawing package that can export CST compatible SAT files. As the optimisation progressed, the shape of the rods became increasingly complex to the point where the shape could no longer be assembled from primitives in CST. SolidWorks enabled the rods to be lofted through differing shapes to provide the desired rod shape. The rounding at the base of the rods where it joins the beam pipe also proved particularly difficult for the CST drawing package to generate. The advanced engine in SolidWorks was able to cope with the highly rounded shape.

During initial testing, it was found that by varying the length of the rods, the cavity could always be brought back onto a resonance of 400 MHz. This was expected from the transmission line approximations that can be made from the cavity shape. Thus throughout all simulations, the length of the rods, and as such, cavity length, were varied to re-obtain resonance whenever a parameter is changed. The initial parameters chosen to optimise to find the minimal surface fields were;

- The separation between the rods, (s).
- The size of the outer can, (R_0).
- The gap between the opposing rods, (g).
- The rod radius, (r).
- The rounding on the rods at the tip and base.

These parameters were varied from the initial values chosen in Table 3.1 to obtain the lowest peak surface electric and magnetic fields. These parameters are shown in Figure 3.2. The initial values were generated from a scaled up version of the CEBAF cavity.

To allow comparison between structures, the peak fields were normalised to a deflecting voltage of 3 MV, as this was a possible operating field of the cavity.

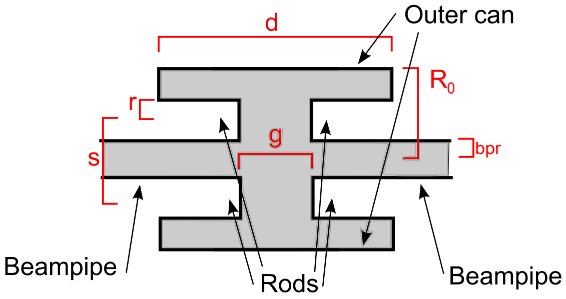

Figure 3.2: Initial shape of the cavity, length (d), can radius (R_0), gap (g), beam-pipe radius (bpr), rod radius (r) and separation (s) are shown.

Parameter	Symbol	Initial Value/mm	Min/mm	Max/mm
Full Gap	g	20	10	100
Length	d	variable	variable	variable
Beam pipe radius	bpr	50	50	50
Outer radius	R_0	150	150	150
Rod radius	r	20	10	40
Separation	s	150	130	210
Rounding		10	5	30

Table 3.1: Basic parameters for the cavity.

3.2 Mesh and Convergence Study

To ensure the simulations were reliable, a mesh study was carried out to make sure the simulations had converged. A study was carried out on the cavity shape to ensure that a suitable amount of mesh was chosen, to provide reliable results. A sweep of lines per wave length [LPWL] was carried out from 30 to 200 LPWL. The general refinement was also varied between 1 and 3. The refinement represents the increase in mesh density around perfect electrical conducting (PEC) surfaces. This allows CST to place more mesh near tightly-curved structures. However, it can also dramatically increase the number of mesh cells used and thus increase the time for a simulation to run. The results of this study are shown in Figure 3.3.

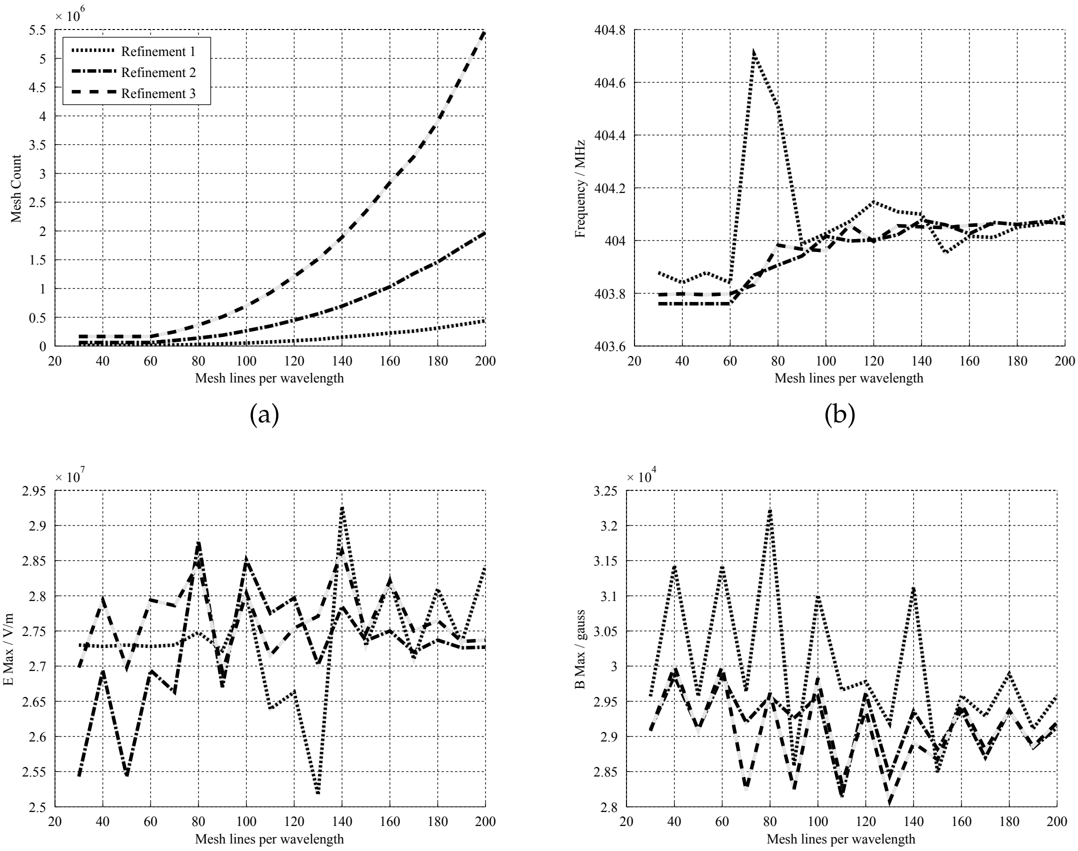

(a) (b)

(c) (d)

Figure 3.3: Convergence study of 4RCC

The frequency of the shape converges very quickly and is very close after 100 LPWL, although the sweep at refinement 1 still has some unpredictable variance.

Both peak fields initially show a saw-tooth reaction to increasing the mesh, as the fields are dependent on the resolution of the surface geometry that includes complex shapes. The amplitude of the variation decreases at increasing LPWL and settles down with good agreement at meshes above 160 LPWL.

As the cavity shape had to be altered to the correct frequency by hand and many simulations were required the shape was first optimised at 100 LPWL. This allowed for the shape to have the correct resonant frequency as this converged at a lower mesh before a higher mesh run at 180 LPWL could finalise the peak fields. The lower mesh limit, defined as the lowest mesh density that will be allowed anywhere, was set to 60 as this would stop there being as large difference in mesh cell size between the smallest and largest mesh cells.

3.3 Separation

The distance between the two conductors plays a critical role in the properties of a transmission line, Therefore, this parameter was varied first. The rod size was kept constant while the separation and beam pipe size were varied. This is shown in Figure 3.4. The lower bound was set at 130 mm with the rod radius set at 25 mm. The upper bound was stopped at 210 mm as this provided no additional data. This provides a beam pipe radius range of 40 mm to 80 mm. The separation was tied to the beam-pipe radius such that $s = 2(r + bpr)$.

The specification for the LHC states a required minimum beam pipe radius of 50 mm [73]. However, having a larger beam pipe can be advantageous e.g. providing HOM extraction or damping [66]. Thus the beam pipe radius was varied to determine if an increased beam pipe size is desirable.

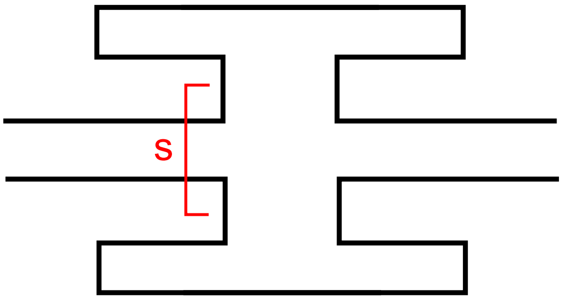

Figure 3.4: Graphical representation of the separation

As shown in Figure 3.5, an increase in beam-pipe size and hence separation is not desired; both peak electric field, located at the tip of the rods and magnetic field, located at the base of the rods and around the beam pipe, decrease as the separation decreases. The electric field has a strong dependence on the rod separation, decreasing almost linearly as the separation decreases. As the rod separation increases, the electric field between them remains constant but

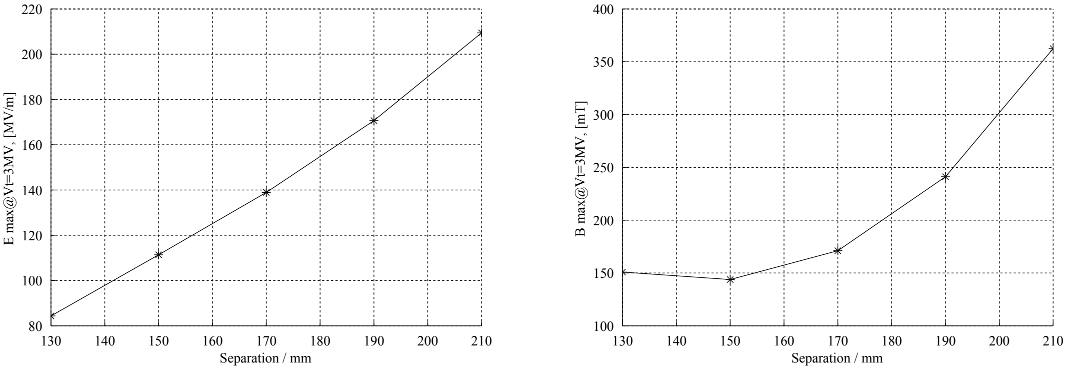

(a) (b)

Figure 3.5: Separation between the rods vs E_{max}/V_t (a), and B_{max}/V_t (b).

over a longer distance, thus the transverse voltage drops. The minimum surface magnetic field is seen at 150 mm with a value of 141 mT, with a slight increase at 130 mm in contrast to the electric field. As voltage drops at low separation, so does the peak magnetic field, as the beam pipe becomes smaller than the rod radius. The slight increase in magnetic field at low separation can be attributed to the convergence of surface currents around the base of the rods and beam-pipe junction, this will be explored later in Section 3.6 and Section 3.7. The general increase in peak magnetic field at larger separation is due to the same fall off in transverse voltage seen for the peak electric field. Figure 3.6 shows how the longitudinal electric field varies as the size of beam pipe is varied between 22 mm and 62 mm across the centre of the cavity. As the transverse voltage is dependant on the rate of change of the longitudinal voltage, and the longitudinal voltage is the integral of the longitudinal electric field, it is fair to assert that the gradient of the electric field at the centre of the cavity is a good representation of the transverse voltage. In this case a smaller beam pipe provides the most gradient.

If the LHC constraints allowed for a smaller beam-pipe, this would be preferable due to the significantly lower peak electric field provided, however a beam-pipe radius of 50 mm is required as such a smaller separation is not achievable.

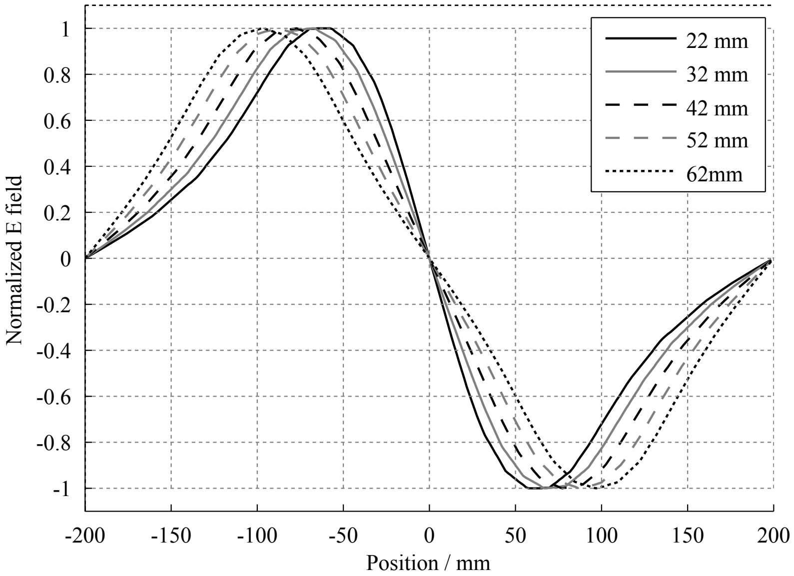

Figure 3.6: Proportional longitudinal electric field across different separations.

3.4 Outer Radius

The LHC specification provides a 150 mm radial envelope for the cavity due to the beam separation. However, this constraint is only in the plane of the rods. As the cavity will be superconducting and placed in an accelerator, an outer casing is required to act as a vacuum vessel. A larger cavity could provide more space for couplers, while a smaller cavity could provide electromagnetic benefits, to investigate this the outer radius was varied between 100 mm and 200 mm. The outer radius is shown in Figure 3.7.

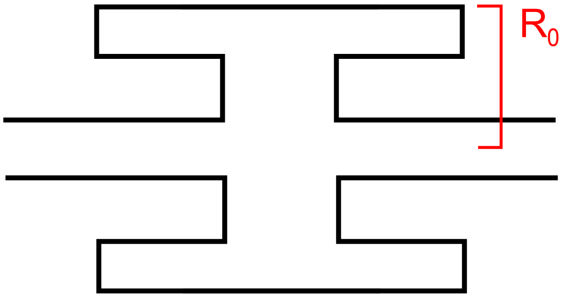

Figure 3.7: Graphical representation of the outer radius

Figure 3.8 shows the peak surface fields, E_{max}/V_t and B_{max}/V_t, with both preferring a larger radius. The outer radius has almost no effect on the peak

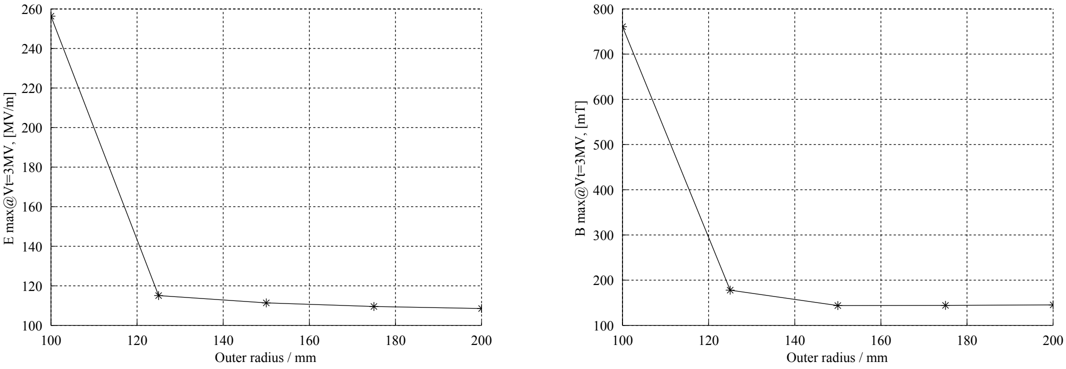

(a)

(b) Outer Radius vs. B/V_t

Figure 3.8: Outer Radius vs. E_{max}/V_t (a) and B/V_t (b)

fields, as the fields are confined to the rods, until the space between the outer can and the rods decreases to a distance of $10 - 20$ mm. This increase is caused by the aforementioned decrease in space between the outer can and rods that, in the case of the magnetic field, reduces the available volume for the magnetic flux to pass through, as the surface current must follow a tight loop between the bottom of the rod and the outer can. For the electric field the proximity of the outer can provides additional capacitance. At a radius of 150 mm, the peak electric field is 113 MVm^{-1} and there is a peak magnetic field of 141 mTMV^{-1}. As long as the outer can maintains a distance of at least 25 mm from the rods, the outer radius can be of any dimension. Below this, careful attention is needed on the rods as the positions of the surface fields are influenced by the proximity of the can.

3.5 Rod Radius Variation

The 'rod radius' was the radius of each of the four rods that support the TEM wave. The rod radius was varied (as shown in Figure 3.9), with the closest faces of the two rods were kept at a constant position against the beam-pipe, between 5 mm and 40 mm . This was to ensure the rod to outer can spacing was at least 20 mm, below which the surface fields increase as seen in Section 3.4.

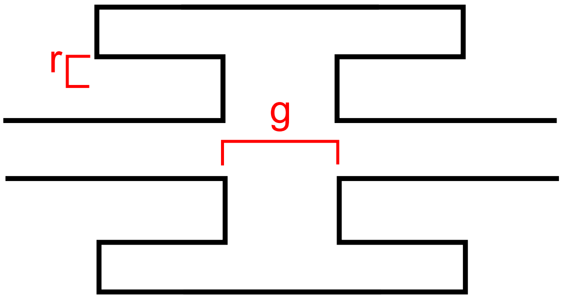

Figure 3.9: Graphical representation of the gap and rod radius

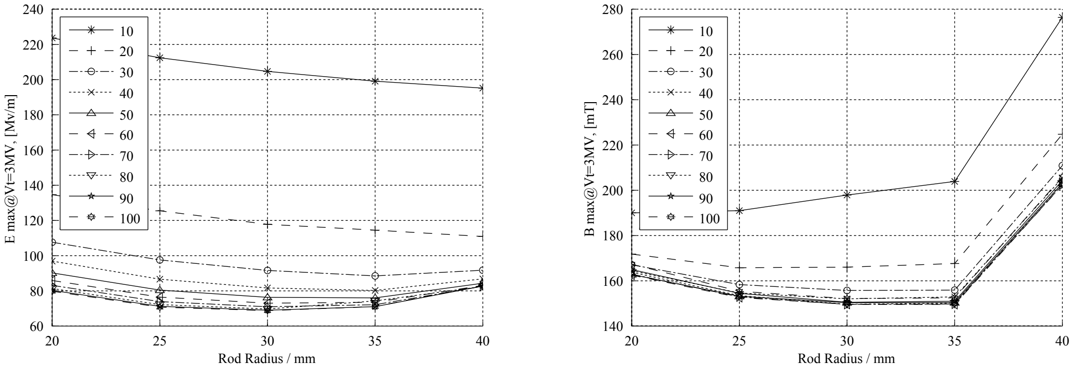

(a)

(b)

Figure 3.10: Variation of rod radius vs E_{max}/V_t (a) and B_{max}/V_t (b)

Figure 3.10 shows the gap between tips vs E_{max}/V_t at various rod radii.

The peak electric field has a minima at a rod radius of 30 mm for all but the smallest gaps. The increase seen at larger rod radii can be attributed to the peaks of the electric field moving further apart, thus lowering the transverse voltage, as seen in Figure 3.11. The increase at smaller rod radii can be attributed to the reduced surface area at the tip resulting in field enhancement[74], though altering the tip rounding may be able to alleviate this.

The peak magnetic field spikes at a rod radius of 40 mm, to values 45 % higher than those of smaller rod radii. This is similar to the increase shown in Section 3.4, when the rod to outer can separation dropped below 20mm and the surface current flows around the outer can rather than between the rods. At smaller radii the peak magnetic field plateaus between 30 mm and 35 mm. The increase seen at small rod radii is the result of the surface current being forced to flow around the beam pipe.

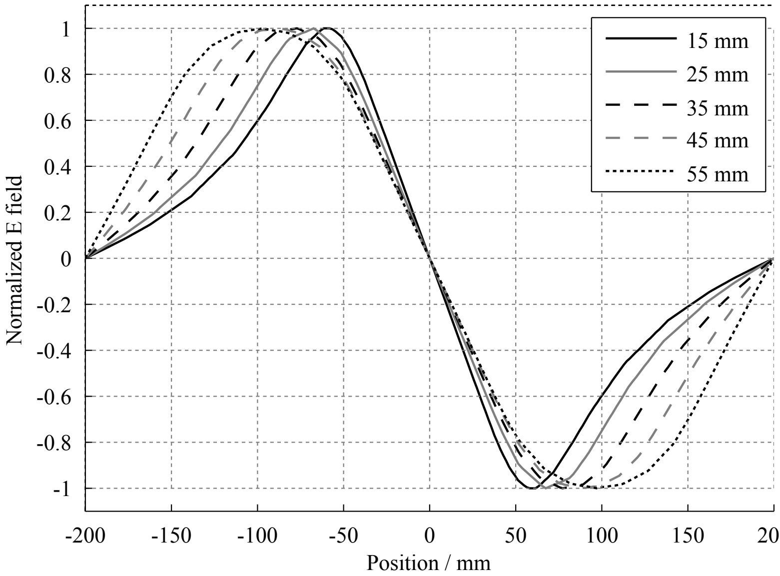

Figure 3.11: Proportional longitudinal electric field across different rod Radii.

The transverse voltage weakly depends on the rod radius, with larger rods causing the field to be more spread out over a larger area. Smaller rods cause the field to congregate towards the centre of the cavity. A rod radii of 30 mm was carried forward for further investigation.

3.6 Gap variation

The 'gap' is the face to face distance between two opposing rods that support the TEM wave. The gap was be varied between 10 mm and 100 mm, as shown in Figure 3.12.

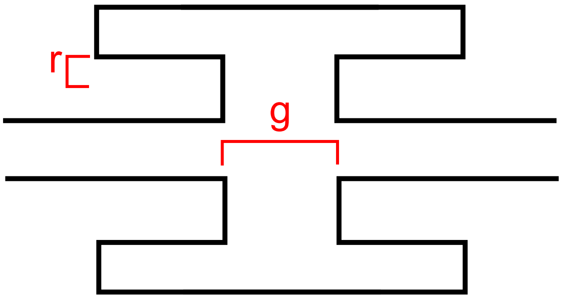

Figure 3.12: Graphical representation of the gap and rod radius

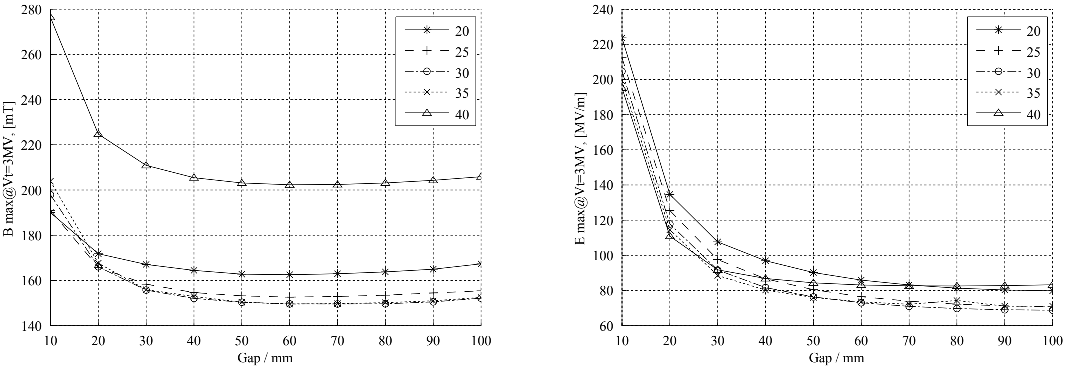

(a)

(b)

Figure 3.13: Gap between tips vs B_{max}/V_t (a) and E_{max}/V_t (b) at various rod radii.

The peak electric field initially depends strongly on the gap as shown in Figure3.13, with the surface electric field peaking at over 200 MVm^{-1} and decreasing as the gap increases. The sharp increase at low gap is caused by the close proximity of the tips causing the charge on the tip to converge at the centre of the tip instead of being spread more uniformly over the tip. This causes the transverse voltage to decrease as almost all of the longitudinal voltage is in the gap and as such there is little interaction with the rest of the cavity. As the charge is located primarily in the small gap, the longitudinal electric field decays very sharply, resulting in considerably less transverse voltage, as shown in Figure 3.14. At a gap of 30 mm, the peak electric field has dropped to below 100 MVm^{-1} for all but a rod radius of 20 mm. After the gap has reached 60 mm, the peak electric field has no dependence on gap and the variation is reduced to less than 5 MVm^{-1} between 60 mm and 100 mm.

The slight increase in peak magnetic field seen at smaller gap values can be attributed to the decrease in transverse voltage as seen in the peak electric field. After 40 mm, the peak magnetic field loses its dependence on the gap and across the remaining parameter space the variation is less than 5 mT.

A gap of 60 mm was chosen to be carried forward for further study, providing a peak surface electric field of 75 MVm^{-1} and a peak surface magnetic field of 135 mT. This was chosen as a foreseeable method of tuning the cavity, as

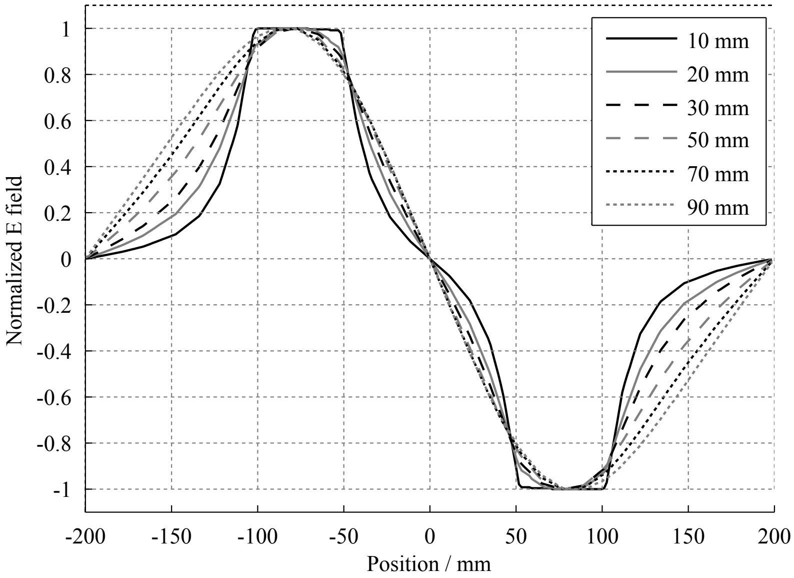

Figure 3.14: Proportional longitudinal electric field across different gaps.

it will rely on squashing the cavity in its longitudinal direction, removing any field performance issues from the tuning process will be beneficial.

3.7 Rounding

In a standard crab cavity, the dipole mode has surface currents that flow around the beam-pipe aperture. For the 4RCC, the current must similarly flow between the two rods around the beam-pipe and also around the outer can. As can be seen in Section 3.5, the peak magnetic surface field was often seen near the base of the rods, or around the beam-pipe rounding due to the high density of surface current in this area. Spreading this current over a larger area reduces the current density as the surface current is not forced over tight curves, and consequently, this reduces the magnetic field. As such, a smooth transition between rod, plate and beam-pipe is needed to reduce the magnetic fields.

Similarly, the peak electric field was seen at the tips of the rods and often near the rounded edge at the largest radius, due to field enhancement[74].

Thus, to reduce the peak fields, suitable rounding at the tip and the base and beam-pipe is needed to ensure good field performance in both the electric and magnetic cases.

3.7.1 Rounding at rod base and beam pipe

As the peak magnetic field is primarily seen at the base of the rods, base rounding and the rod size were varied at the same time to minimise the peak magnetic field. Section 3.5 shows that varying the rod radius shifted the peak magnetic field between the edges of the rods and rounding on the beam-pipe and rod base.

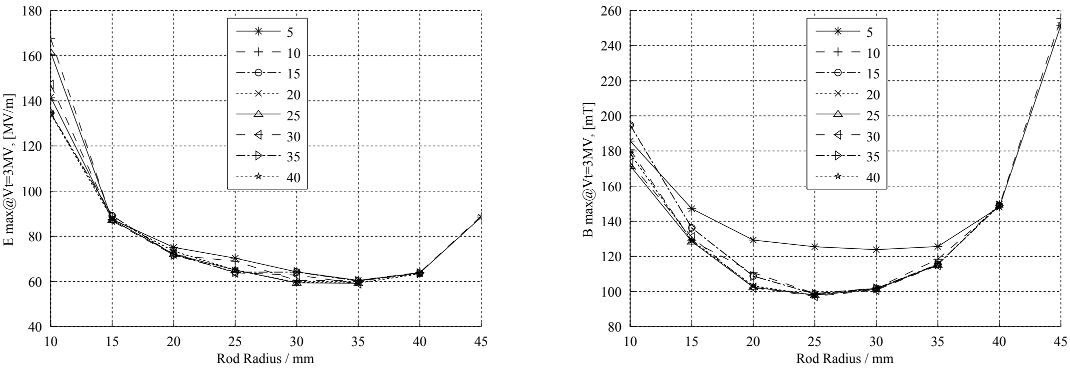

(a) (b)

Figure 3.15: Peak electric (a) and magnetic (b) field over various rod radii at different base rounding

The peak magnetic field is highly dependent on the rod radius, with a minimum at 25 mm of 96.6 mTMV^{-1}. This can be seen in Figure 3.15. At values lower than this, the peak field is condensed across the narrow cylinder of the rods. As the rod size increases, the distance between the rod and the outer can decreases and the peak field moves to between the rod and outer can. Very small rounding results in a smaller area for the surface current to flow though, which results in higher surface fields. The increased rounding provides minimal field improvement beyond - less than 2 % -, however, it does continue to improve and a larger rounding always provides better performance. Larger rounding may provide additional benefit as further changes to the rod shape are made.

As expected, the peak electric field has little dependence on rod-base rounding, due to being located at the tip of the rod and away from this variation . The difference at 5 mm can be attributed to the very high surface fields that were forced onto a very small tip. The minimum electric field is seen at a radius of 30 mm with a rounding of 40 mm. This corresponds to a peak field of 59.0 MVm^{-1}, though there is a $\sim 2\,\%$ variation across all other values of rounding at 30 mm. A larger rod radius provides more surface area for the peak electric field to be spread over. However, at very large rod sizes, $40-45$ mm, the rods become close to the outer can and the peak field rises.

3.7.2 Rounding Tip

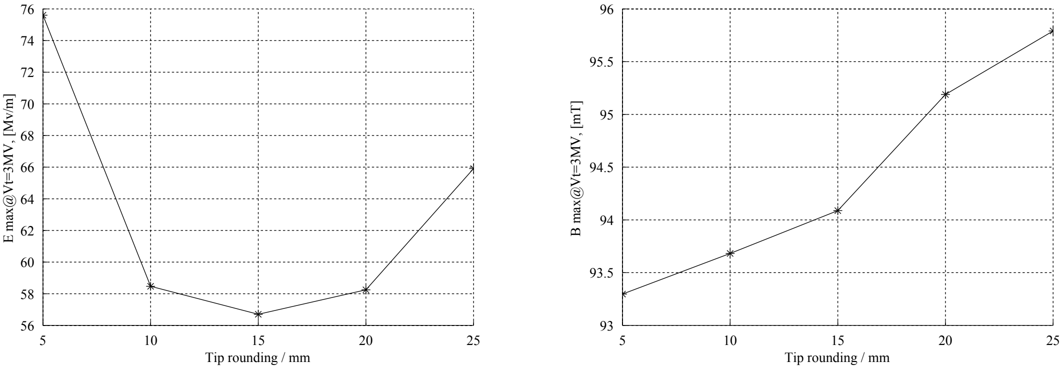

(a) (b)

Figure 3.16: Rounding radius on the tip vs E_{max}/V_{t} (a) and B_{max}/V_{t} (b)

The effects of rounding the tips of the rods are shown in Figure 3.16. The rounding of the tips is quite critical for the peak electric field. This primarily effects the peak electric field, and the 2 % variation in peak magnetic field can be attributed to the slight geometric alterations. The peak electric field has a minimum at 15 mm, although at higher rounding the gap decreases. This does not account for the increase in peak electric field. If the rounding is too small, the field enhancement at the tips dominates and the peak field is at the edge of the rods (see Figure 3.17a). As the rounding increases, this effect diminishes and is replaced by a peak towards the centre of the rods as the surface of the rod curves away, effectively focusing the field at the centre of the tip and reducing the transverse voltage (see Figure 3.17b).

Thus, a tip rounding of 15 mm will be chosen with a peak electric field of 56.9 MVm^{-1}.

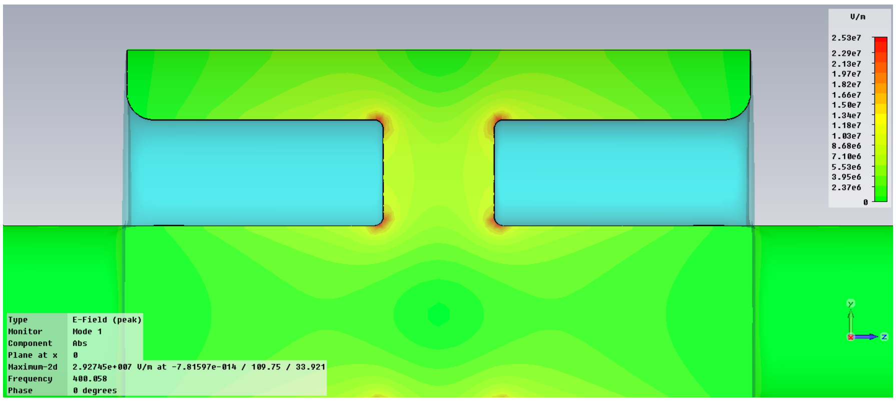

Type	E-Field (peak)
Monitor	Mode 1
Component	Abs
Plane at x	0
Maximum-2d	2.92745e+007 V/m at -7.81597e-014 / 109.75 / 33.921
Frequency	400.058
Phase	0 degrees

(a) Tip rounding of 5mm

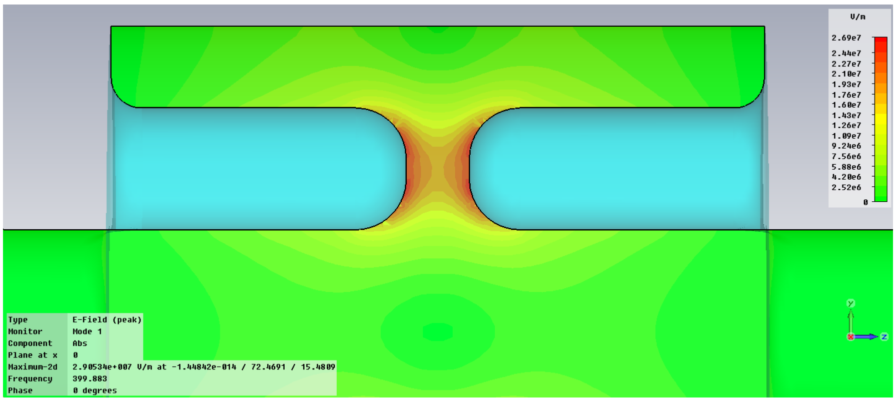

Type	E-Field (peak)
Monitor	Mode 1
Component	Abs
Plane at x	0
Maximum-2d	2.90534e+007 V/m at -1.44842e-014 / 72.4691 / 15.4809
Frequency	399.883
Phase	0 degrees

(b) Tip rounding of 25mm

Figure 3.17: 2D contour plot of peak electric field.

3.8 Conical Rods

As the peak electric and magnetic fields are located in different areas of the rod, the tip, and the base respectively, conical rods were investigated (see Figure 3.18). To this end, the base size was varied independently of the tip to determine if conical rods would prove beneficial.

The rod base diameter has little effect on the peak electric field although it is quite erratic, as shown in Figure 3.19. The variation of electric field is erratic

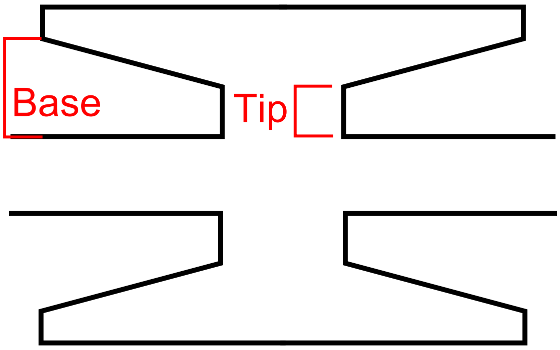

Figure 3.18: Tip and base of rods

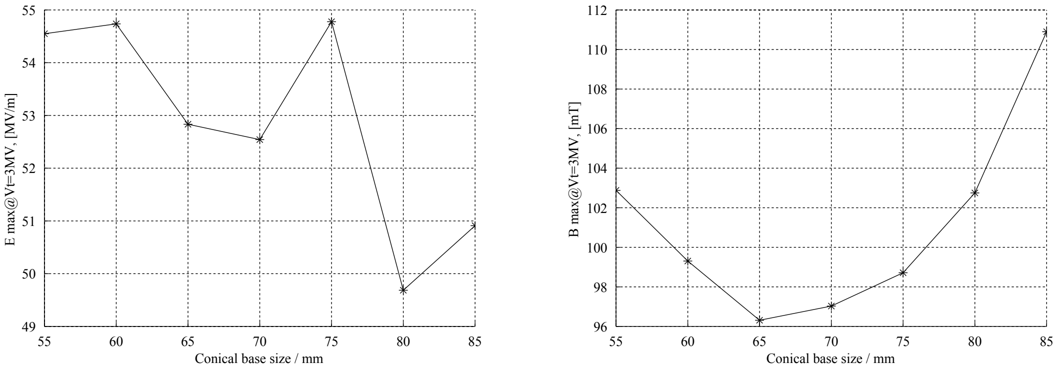

(a)

(b)

Figure 3.19: Rod base diameter vs E_{max}/V_t (a) and B_{max}/V_t (b)

due to numerical instabilities within CST, with a weak decreasing tend in peak surface field. The peak magnetic field increases with decreasing diameter as the surface currents are confined to a smaller area and thus a smaller curvature. A minimum is achieved at 65 mm. Increasing the diameter initially decreases the peak field before increasing it again, which can be attributed to the proximity of the outer wall. As the distance between the outer wall and the base of the rod decreases, there is a preference for the surface currents to flow around the outside of the cavity can rather than between the rods. This results in an increased peak magnetic field on the surface of the cone furthest from the beam pipe.

The optimal circular base of 65 mm was chosen due to the lower magnetic field, however the increased radius perpendicular to the plane of the rods has a negative effect on the overall performance, whilst the increased radius perpendicular to this has positive effect. Thus the decision to make the rods oval was taken to utilise this.

3.9 Oval Rods

At large rod radius where the rod is close to the outer can, the magnetic field concentrates in the space between the rod and the outer can - this can be seen in Figure 3.20. A similar effect was noted for the electric field where the tip of the rod starts to interact with the outer can as the electric field interacts with the smaller gap between the rod and the outer can, due to the outer can effectively being earthed. By altering the rods to have an oval shape, the benefits of larger rods can be achieved while the rod to outer can spacing is maintained.

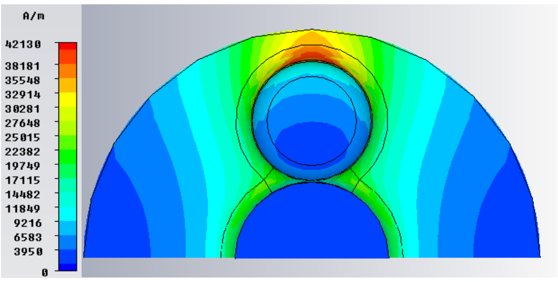

Figure 3.20: Location of peak magnetic field seen at large rod radius.

As the peak of the field moves around the shape of the rod, the location was referred to as the back - the area next to the outer can, side or front - the area next to the beam pipe. These areas are shown in Figure 3.21.

3.9.1 Oval Base

The base has a critical role on the magnetic field, due to the surface currents converging around the beam-pipe, the increased surface away from the beam-pipe alleviates the effect of this convergence.

3.9.1.1 Breadth

The base breadth (BWY) was varied, as shown in Figure 3.22.

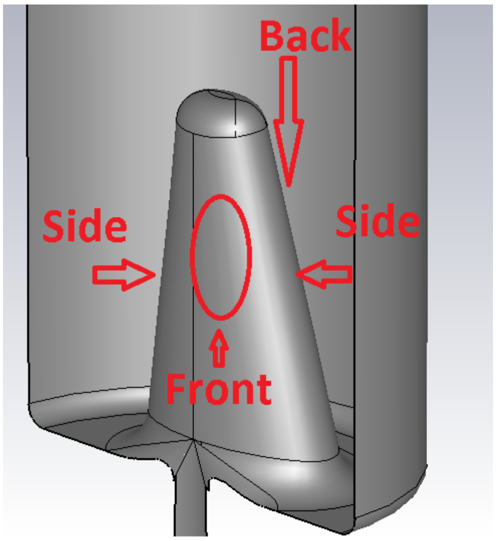

Figure 3.21: Areas on the oval rods.

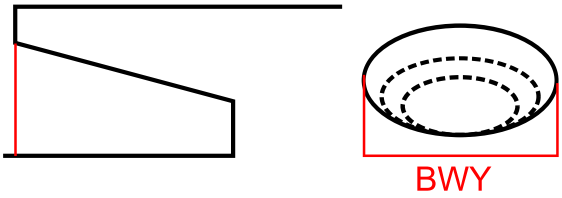

Figure 3.22: Schematic representation of BWY

As shown in Figure 3.23, increasing the base breadth slightly decreases the peak surface electric field, though only by 10 % across the entire parameter space. The peak magnetic field rapidly falls off with increasing base breadth, losing almost 30 %, before slowly increasing after 110 mm.

As expected, the BWY has a critical role on the peak magnetic field. When the BWY is smaller than the beam-pipe, (100 mm) there is a steep decrease in peak field as the BWY increases to the beam-pipe size. This dependence is caused by the magnetic field peaking on the beam-pipe instead of the rod, as the magnetic field is forced to bend around the beam pipe. When the BWY becomes larger than the beam-pipe, the trend reverses and a slower increase is seen where the magnetic field concentrates on the increasingly pointed sides of the rods.

The peak electric field weakly depends on BWY and falls slightly, this is

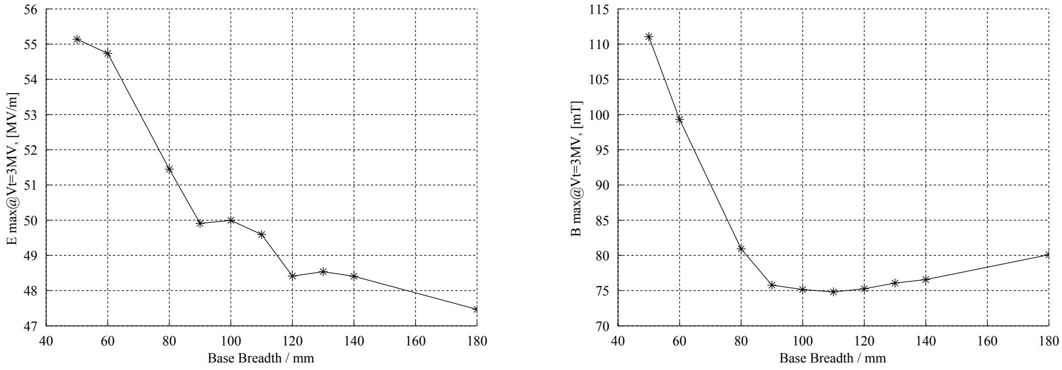

(a) (b)

Figure 3.23: Rod base breadth vs E_{max}/V_t (a) and B_{max}/V_t (b)

most likely due to a slight decrease in transverse voltage.

The minimum peak magnetic field occurs at 110 mm with a peak field of $76.4\,\mathrm{mTMV}^{-1}$, thus is the chosen value due to the significant improvement it offers.

3.9.1.2 Width

The base width (BWX) was varied, as shown in Figure 3.24.

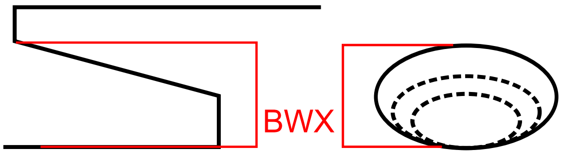

Figure 3.24: Schematic representation of BWX

Again the BWX plays crucial role on the peak magnetic field and a limited role on the electric field. The width affects the peak magnetic field in two ways, firstly increasing the width decreases the distance between the outside wall and the base of the rod, as noted in Section 3.5. When this space becomes too small, the surface currents take an alternative route and the peak magnetic field spikes. However, when BWX decreases, the peak magnetic field shifts away from the back of the rods to the sides and increases as the surface current is forced to make a tighter curve, similar to the problem noted in Subsection 3.9.1.1.

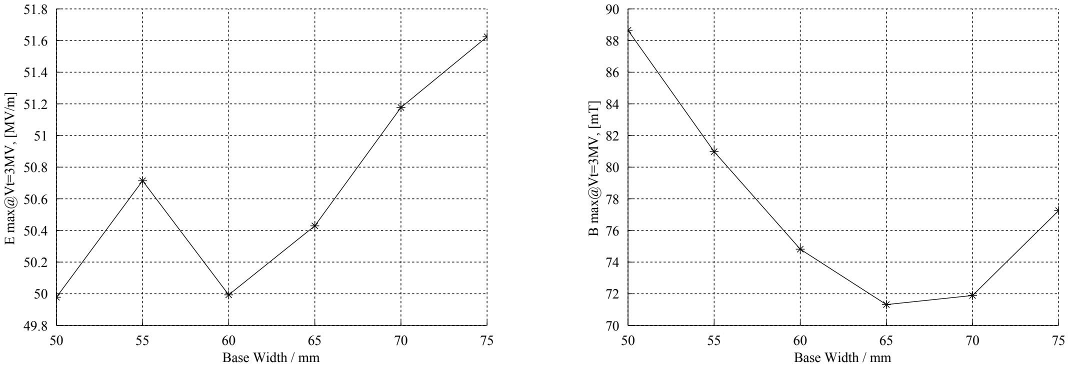

(a) (b)

Figure 3.25: Rod base width vs E_{max}/V_t (a) and B_{max}/V_t (b)

The peak electric field shows little dependence on BWX though a minor increase is seen with increasing BWX, most likely due to the slightly increased interaction with the can wall. The best value for a compromise between two magnetic field factors is 65 mm.

3.9.2 Oval Mid point

The mid point of the rods was varied to see if having a concave or convex rod profile would improve the peak field performance. A guide oval halfway along the rod was used to alter the profile. As this area is slightly removed from the peak fields, no dramatic reductions were expected.

3.9.2.1 Breadth

The mid breadth (MWY) was varied, as shown in Figure 3.26.

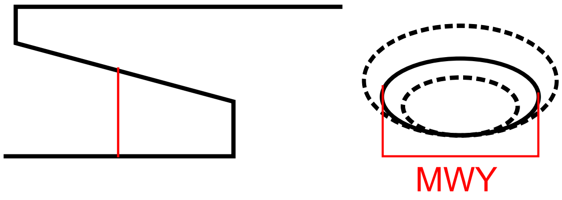

Figure 3.26: Schematic representation of MWY

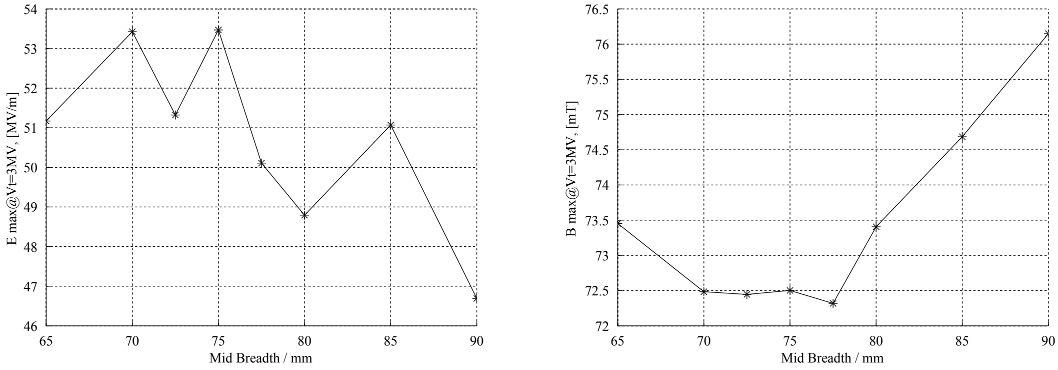

(a) (b)

Figure 3.27: Rod mid breadth vs E_{max}/V_t (a) and B_{max}/V_t (b)

The peak electric field weakly depends on the MWY , for convex sides, above 77.5 mm, the field is slightly lower than for concave profile, below 77.5 mm.

The peak magnetic field for concave profile shows a good decreasing coloration that has a minima for straight profile at 77.5 mm. A convex profile causes the peak magnetic field to increase as the sides of the rods become elongated and the field is concentrated into a smaller area. To this end, varying the breadth of the rod has little discernible effect. A straight profile was chosen at 77.5 mm. Though this could be used to allow a slight trade off between peak electric and magnetic fields by increasing the MWY to lower peak electric field if desired.

3.9.2.2 Width

The mid width (MWX) was varied, as shown in Figure 3.28.

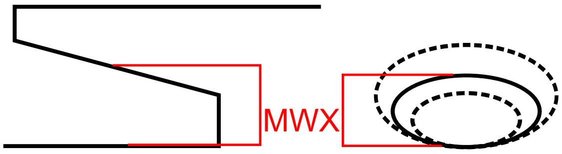

Figure 3.28: Schematic representation of MWX

The Peak magnetic field depends strongly on the MWX with two factors limiting the field performance. When MWX is small, the edges of the rods are

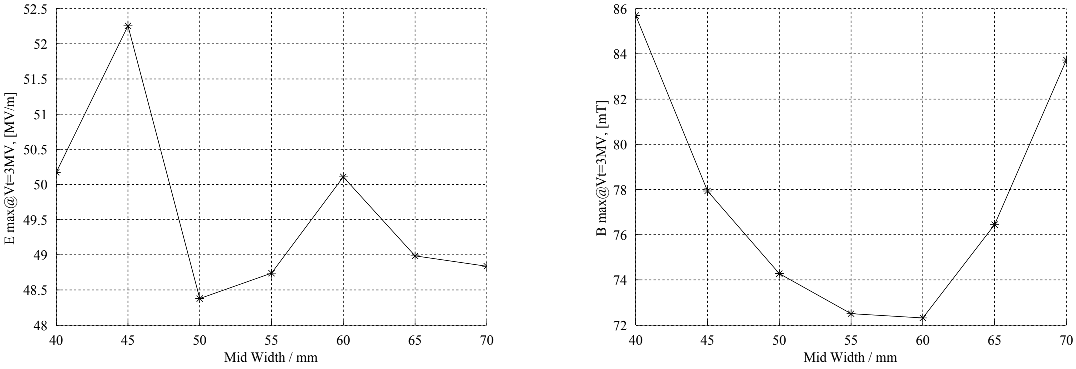

(a)

(b)

Figure 3.29: Rod mid width vs E_{max} / V_{t} (a) and B_{max} / V_{t} (b)

elongated and the peak field increases. Alternatively, when MWX is large, the rod-to-can distance falls and magnetic field increases.

The MWX has little effect on the peak electric field, though a weak trend of decrease is shown, this slight decrease could be attributed to the minor increase in fringing fields due to an increased angle on the side faces of the rod. Thus a value of 60 mm was chosen as this provides good peak magnetic field with little impact on the electric field.

3.9.3 Oval Tip

The tips of the rods are the location of most of the electric field and as such the peak electric fields will be most effected by any variation in their size. However, changing the tip profile can have dramatic effects on the overall profile of the rod and thus effect the magnetic field significantly.

3.9.3.1 Breadth

The tip breadth (TWY) was varied, as shown in Figure 3.30.

The peak electric field has some dependence on TWY due to the transverse voltage being intrinsically linked to the electric field at the tips, but there is little change as long as the tip is not 40 mm, or smaller, leading to field enhancement. The peak magnetic field has a strong dependence on the TWY, which follows

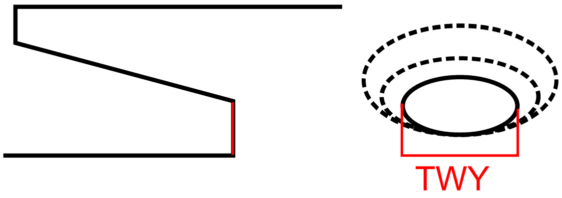

Figure 3.30: Schematic representation of TWY

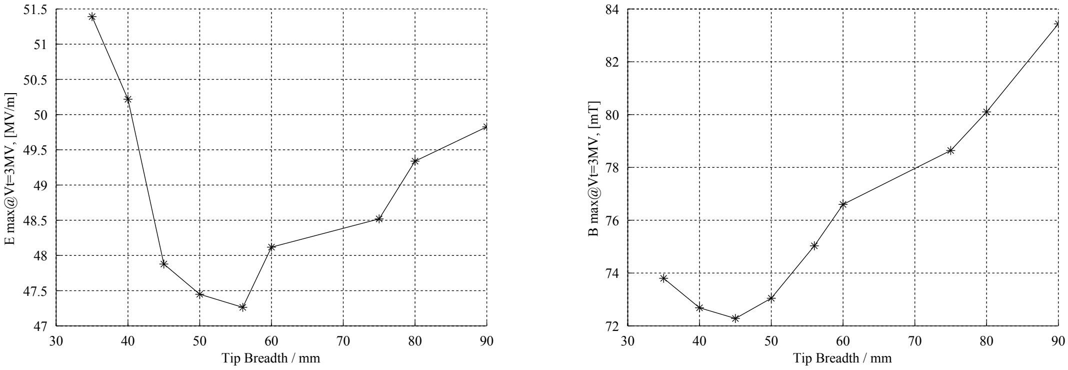

(a) (b)

Figure 3.31: Rod tip breadth vs E_{max}/V_t (a) and B_{max}/V_t (b)

the previously seen trend of increasing peak field as the edges of the rod become more elongated. The slight increase at 35 mm can be attributed to the decrease in transverse voltage. A value of 45 mm was chosen as it gives a good trade off between minimum magnetic and electric peak fields.

3.9.3.2 Width

The tip width (TWX) was varied, as shown in Figure 3.32.

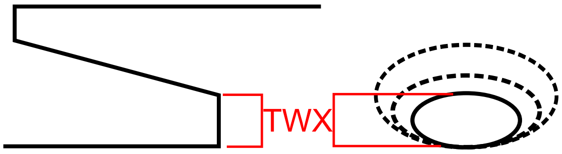

Figure 3.32: Schematic representation of TWX

The peak electric field decreases with increasing TWX as the tip becomes more circular, at 45 mm, this reverses as a slow increase. At low TWX, the

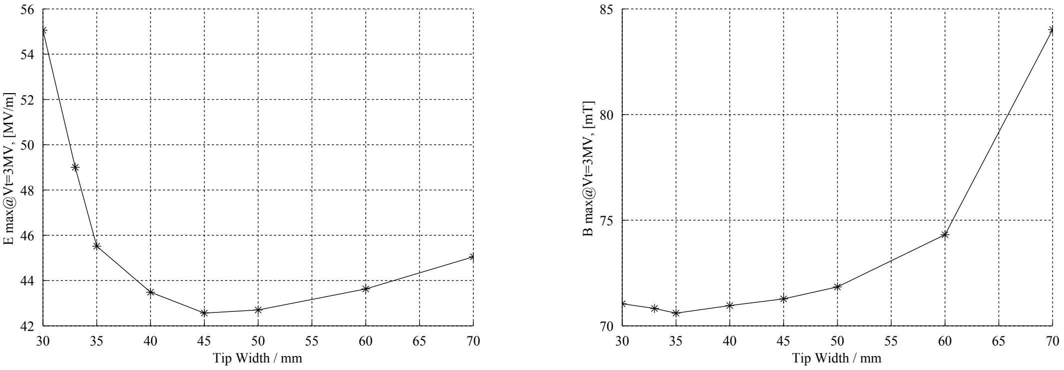

(a) (b)

Figure 3.33: Rod tip width vs E_{max}/V_t (a) and B_{max}/V_t (b)

surface area of the tip is reduced, causing field enhancement. Increasing the surface area helps to reduce the field enhancement. However, as the tip becomes closer to the outer can, the peak is pulled towards the back of the rod and starts to increase.

The peak magnetic field also has a strong correlation to the increased TWX and suffers from the same decrease in rod to can spacing, as seen earlier. The small increase seen at low TWX is caused by the narrowing of the sides of the rods. As a compromise between both peak fields, 40 mm was chosen, however, if a trade off for an improvement in either field is needed in the future, a variation of $\sim$ 5 mm can be made.

3.10 Cavity Shape

The optimised cavity shape parameters are presented in table 3.2. The absolute surface fields are shown in Figure 3.34.

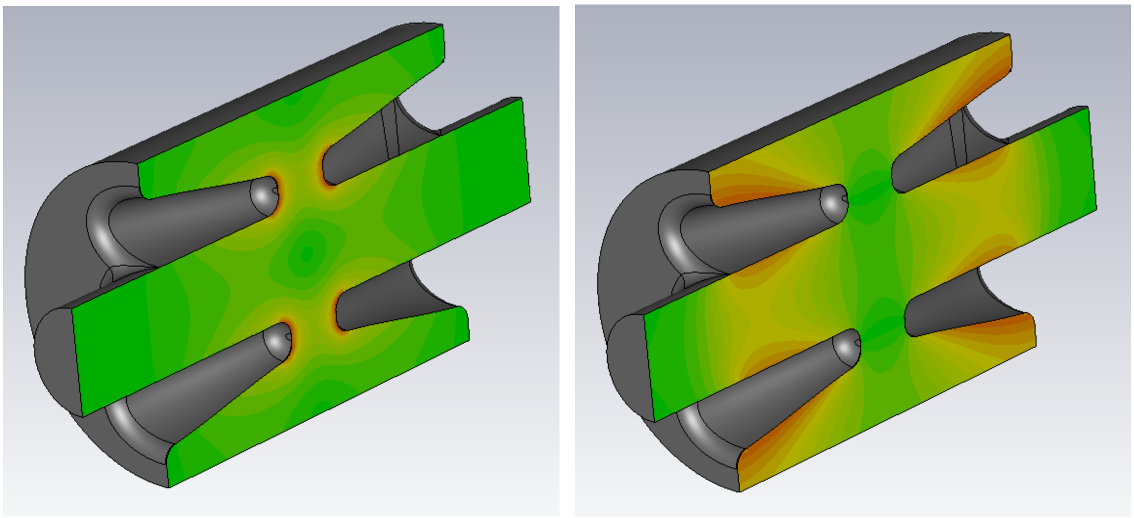

(a) (b)

Figure 3.34: Peak electric (a) and magnetic (b) fields as absolute plot

Parameter	(mm)
Gap	60
Beam pipe radius	50
Outer radius	150
Base breadth	110
Base width	65
Mid breadth	77.5
Mid width	60
Tip breadth	45
Tip width	40
Tip rounding	15
Base rounding	30

Table 3.2: Optimised parameters for the cavity.

The peak fields for this cavity are - B max at $\mathbf{V}_t = 3$MV of 70.9 mT and an E max at $\mathbf{V}_t = 3$MV of 43.8 MV.

3.11 Changes due to Beam-pipe shrinkage and coupler squash

The decision was made by CERN at the LHC CC Workshop in 2010 [75] for local crabbing rather global, a change in optics led to the requirement for the minimum beam-pipe diameter allowable for the crab cavity to be reduced from 100 mm to 84 mm. The separation between the opposing beam lines was fixed at 192 mm, this resulted in a smaller available envelope for the cavity, as 150 mm was available for the cavity, cavity walls and space for alignment. From Section 3.3 it was known that having the rods close together provides better field parameters, which was beneficial. Moving the rods closer together (thus increasing the space between the rods and the outer wall) also gave more room to alter the profile of the base of the rods. At this time, design work on the couplers had progressed somewhat and a racetrack-shaped outer can was desired (see Chapter 8). This consisted of two semicircles of radius 115 mm, linked by two straights of 60 mm creating a racetrack shape that fitted within the allowed confines of the LHC envelope. This is shown in Figure 3.35.

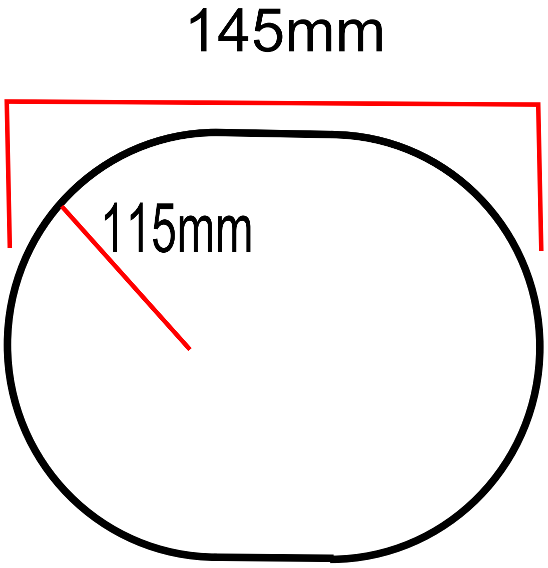

Figure 3.35: Racetrack-shaped outer can

An optimum shape had to be chosen that provided good coupling and acceptable peak fields. The variation with racetrack size is shown in Figure 3.36. The peak magnetic field was the primary concern as the reduced distance between the outer can and rod was known to cause the field to spike.

The envelope is 5 mm smaller at 145 mm than the 150 mm previously. This size was chosen to allow more space for the walls of the can and opposing beam line.

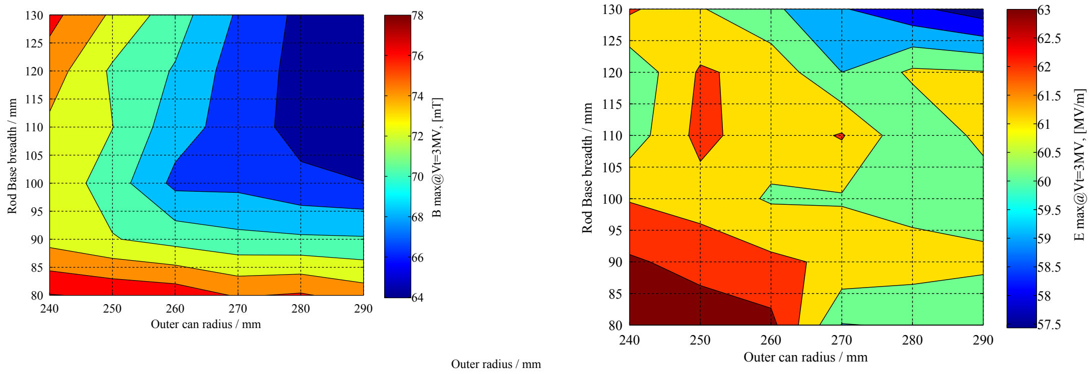

(a) Magnetic field variation

(b) Electric field variation

Figure 3.36: Variation in Peak fields as the size of the rod base and outer can was varied.

3.12 Updated Cavity Design

With the reduced beam-pipe size, the rods were moved closer together, which produced a significant decrease in peak surface fields. This is primarily due to the transverse voltage for a given amount of energy being at least in part proportional to the separation between the rods. The 16 % decrease in distance produces a $\sim$ 15 % decrease in peak surface fields. The additional space created by moving the rods closer together allowed the base width of the rods to be increased. Using knowledge and experience gained from Sections 3.3 through 3.9, the shape was subtly re-optimised to the new peak surface fields of 68.2 mT and 37.0 MV at 3 MV transverse field.

Although the available space in the cavity decreased, with the outer can being limited to 145 mm from 150 mm, the larger decrease in the beam pipe radius from 50 mm to 42 mm added an additional 3 mm of room.

This enabled the base width to be increased by 5 mm, providing an increased curvature on the edge of the rod bases. This allowed the surface current to be spread over a larger area and reduce the peak field. The increased tip size results in the larger curvature propagating further up the sides of the rods to further decrease the peak magnetic field. Figure 3.37 shows on of the repeated optimizations of the rod base width. With these changes, the peak surface magnetic

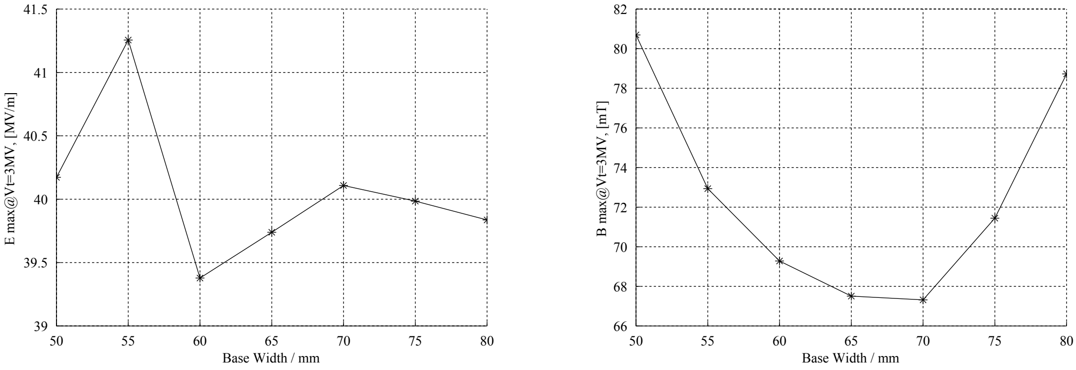

(a) (b)

Figure 3.37: Rod base width vs E_{max}/V_{t} (a) and B_{max}/V_{t} (b)

field at a transverse voltage of 3 MV was reduced to 66.2 mT.

The additional space allowed the tip size to be increased from 40 mm to 65 mm in width and 45 mm to 70 mm in breadth. The larger tip size allowed for increased rounding on the tip without causing field emission. This allowed for the peak electric field to be uniformly spread over a greater surface and with the additional changes reduced to 37.0 MV at a transverse voltage of 3 MV

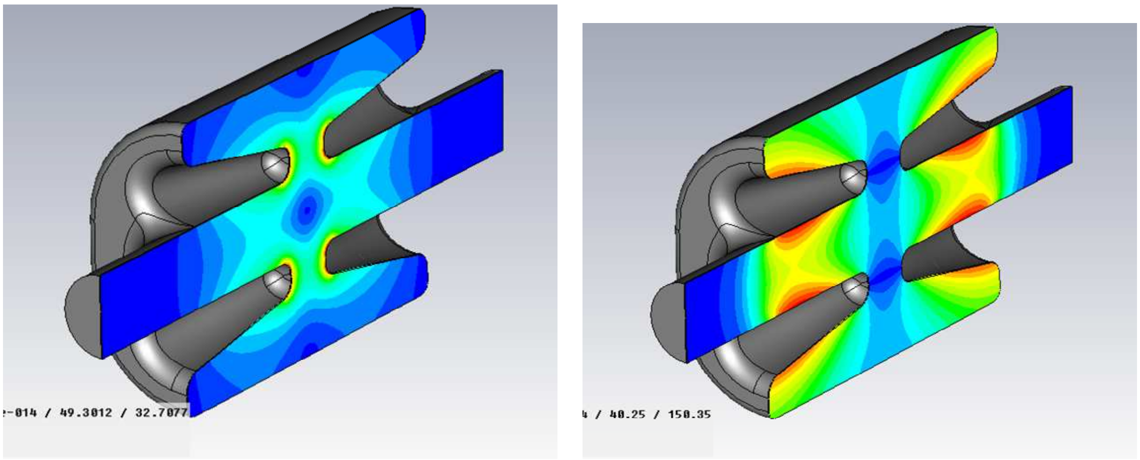

(a) Peak electric field as absolute plot

(b) Peak magnetic field as absolute plot

Figure 3.38

The final cavity design is shown in figure 3.38. The peak electric field is uniformly spread across the tip surface. The peak magnetic field is spread around the base of the rod. By having the back of the rod follow the curvature of the outer can, the peak field is not concentrated in the space between rod and can.

Instead the peak field sits away from the beam-pipe on the edges of the rod near its base.

3.13 Conclusion

Parameter	Value
Full Gap	60 mm
Length	402 mm
Beam pipe radius	42 mm
Outer radius	145 mm
Beam pipe rounding	30 mm
Rod base rounding	20 mm
Tip rounding	20 mm
Tip width	65 mm
Tip breadth	70 mm
Mid width	67.5mm
Mid breadth	90 mm
Base width	70 mm
Base breadth	110 mm
Emax @ 3MV	37.0 MV/m
Bmax @ 3MV	66.20 mT

Table 3.3: Parameters for the cavity.

The final cavity dimensions and fields are given in Table 3.3. When designing the cavity, the limitations imposed by the LHC restricted most parameters to their nominal values. In this case the smallest beam-pipe available (84 mm) and the largest outer can size (145 mm centre to edge). This left the shape of the rods as the primary focus for optimisation. The rod shape was split into two primary areas of focus - the tips focused on the peak surface electric field, while the junction between the rods, baseplate and beam-pipe focused on the peak magnetic field. In both cases fields need to be dissipated over as large a surface area as possible. For the tips, this involved finding the best ratio tip rounding to tip area. For the base, a compromise between base size, rounding and rod-to-can-spacing had to be found. The peak electric field is only strongly dependent on the tip width, however Bmax is spread over the rods. Hence, it is dependent on almost every parameter but is most sensitive to the base variation.

Electric field

The peak electric field is concentrated near the tips of the rods and as such these should be the main focus for reducing the peak electric field. An increased surface area at the tip is usually preferred for an increased surface area for the electric field to be spread over, however this can cause problems for the peak magnetic field. Rounding on the tips of the rods is critical as shown in Figure 3.17, too much and the field is forced into a smaller area, too little and the field peaks at the edges. Thus an optimum must be found that evenly distributes the field over the entire area.

Magnetic field

The peak magnetic field is located around the base of the rods, the beam-pipe and the narrow sides of the rods. Rounding on the beam-pipe is critical up to a point, then becomes insignificant once the peak is shifted away from the beam pipe. At decreased beam-pipe radii, an increased rounding is necessary over a larger beam-pipe radii. The size of the base of the rods greatly influences the peak magnetic field, although the rod profile as a whole dictates the areas where the peak field is located. A large base is optimal, though the distance between the base of the rod and the outside wall, can be critical, if the distance decreases the peak shifts from the narrow, sides of the rods to the face against the outside wall often increasing in value. Similarly if the rods become too elongated and narrow the field concentrates along these narrow edges, driving up the peak magnetic field. The oval shape is necessary however, as the profile of the base of the rods should extend beyond the edge of the beam pipe so the surface currents do not converge around the beam pipe. Thus an optimum shape must be found that allows for the greatest surface area around the base of the rod to distribute the magnetic field. However, this increase must not result in the base of the rod becoming too close to the outside wall, nor must the rounded faces of the rods become too pointed, as both of these will dramatically increase the peak magnetic field.

Chapter 4

Voltage Calculations

4.1 Introduction

At the LHC-CC Workshop 2010[75], the question of field flatness was raised. The fields for the cavity at that time were deemed unsuitable and a partial re-design was undertaken to eliminate the change in field whist still maintaining as low surface fields as possible. In an ideal case, the transverse voltage would be uniformly flat across the entire region where the beam would be present. This re-design called for the field profile to be as flat as possible and no worse than that of a pillbox cavity. Ideally, a crab cavity will have a purely dipole field within it. However, this is not always the case, and asymmetric components or higher order components may exist within the cavity. These will perturb the dipole field and produce unwanted effects.

4.2 Complications of Voltage Variation

When a particle travels through a crab cavity, it is hoped there will be no kick in the direction of travel $(\hat{\mathbf{z}})$. The full kick will be in the desired direction of deflection $(\hat{x})$ and there will be no kick perpendicular to this $(\hat{y})$.

The two beams of colliding particles will lie on a plane, therefore the kick imparted to the beam should also lie on this plane (usually the horizontal). In the LHC, there is the possibility of a vertical kick, and although the principles are identical, we shall concentrate only on the horizontal here. Any kick normal to this plane will result in misalignment of the beam, which will result in a vertical rotation. This will lead to an unwanted vertical crossing angle at the IP, and thus loss in luminosity. If a vertical kick is induced, and is not able to be removed by the anti-crab cavity, the beam will start to oscillate around the ring and could cause the collimators to interact with it, clipping the beam . This unwanted kick will be referred to as "the parasitic deflection", as it is an unwanted but innate by-product of the crabbing mode.

When combined with the positional variation, the minimisation of any unwanted variation is essential. As such a uniform horizontal deflecting voltage is desired, with minimal parasitic voltage. The crab that is induced in the beam must also be removed after the interaction, if the de-crabbing cavities do not remove the full crab it is possible for instabilities to build up as the bunch revolves around the beam line.

The deflecting voltage for a pillbox, a cylindrically-symmetric cavity with beam pipes and a four rod deflecting cavity will be analytically calculated across the region of the LHC beam-pipe (radius 42mm). The numerically-simulated deflecting voltages for parallel plates and the four rod compact LHC crab cavity will then be compared to these. To compare these cavities easily, the voltage will be calculated at specific (x,y) co-ordinates, as well as being displayed graphically across a range of co-ordinates to aid in comparison.

The deflecting voltage received by a particle travelling through a crab cavity would ideally be independent of its transverse position. However, this is not always the case due to design constraints imposed by the cavity shape or its additional components. If a particle travelling through off-axis receives a different kick to a particle on axis, the resulting change in transverse momentum will be different across the bunch. Similarly, if a bunch enters the cavity at the wrong position due to an error in the dipole kicker magnets or beam-beam interactions, the bunch could be misaligned with its reciprocal bunch in the second beam line.

In the case of the LHC, the beam length is 75.5 mm and its transverse size is 16.6 μm. With the 2020 upgrade expected to increase the crossing angle to 315 μrad[73]from the current 285 μrad, there is expected to be a significant luminosity drop. Using the geometric loss factor R :

$$R = \frac{1}{\sqrt{1+\Phi^2}} \tag{4.1}$$

Φ is the Piwinski factor calculated as[18]:

$$\Phi = \frac{\theta_c \sigma_z}{2\sigma_t} \tag{4.2}$$

Where θ_c is the crossing angle, σ_z is the longitudinal bunch size and σ_t is the transverse bunch size. Using the parameters from the 'Crab Cavity for the LHC Luminosity Upgrade'[73], the loss factor decreases from, 0.838 to 0.813, using the lower crossing angle of 315 μrad. If the upper crossing angle of 509 μrad is used, this increases even further to 0.656.

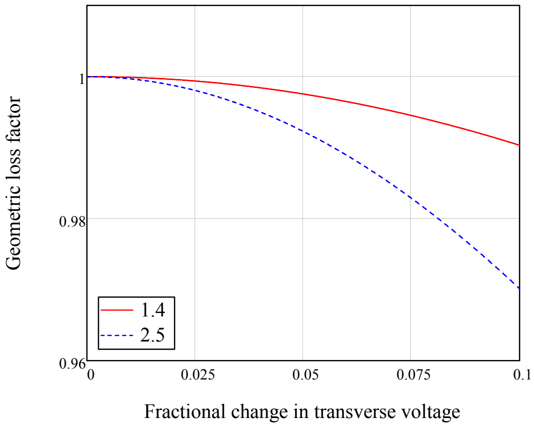

Figure 4.1: Geometric loss factor at varying factional change in voltage at the two extremes of Piwinski factor.

Assuming the crab cavities are able to account for this crossing angle and, in the nominal case, return the loss factor to 1 (i.e. no loss), then small changes in the deflecting angle will result in a different deflecting angle and thus a different

Piwinski factor. If we calculate the change in angle as

$$\Delta\theta_c(x,y) = \theta_c \frac{\mathbf{V}_x(x,y) - \mathbf{V}_x(0,0)}{\mathbf{V}_x(0,0)} \tag{4.3}$$

where $\mathbf{V}_x(x,y)$ is the deflecting voltage received at the position (x,y) in the cavity by the particle and $\mathbf{V}_x(0,0)_0$ is the nominal value of the deflecting voltage at the centre of the cavity. Then, as the Piwinski factor is directly proportional to the crossing angle, it will also be proportional to the change in deflecting voltage. From Figure 4.1, the change in geometric loss factor for a 3% drop in deflecting voltage will cause a 0.088% or a 0.280% drop in luminosity for a Piwinski factor of 1.4 and 2.5 respectively. For a 10% drop in voltage, a 0.966% or 2.986% drop in luminosity is seen for 1.4 and 2.5 respectively, however this is comparatively small. These numbers are unlikely to be a limiting factor on the LHC, however they may be indicative of multipole components interfering with the deflection.

4.3 Multipole Components

The deflecting mode in the LHC is not a pure dipole. The mode consists of a superposition of terms that create the defecting mode. The main component of the operating mode is dipole however there are higher order terms that appear at increased offset that can impact the beam [76]. As the higher order modes are highly susceptible to offset, the decapole mode varies with r^5, the terms of most concern are those with components that are noticeable close to the beam position.

The multipole components for the cavity were examined to ensure they were of acceptable levels. The multipole expansion of the cavity can be expressed as a summation of angularly dependant components at.

$$\mathbf{V}_z = \sum_n x_n (r^n \cos(\theta^n) + r^n \sin(\theta^n)) \tag{4.4}$$

We know that there is no longitudinal voltage on axis, or in the plane perpendicular to the direction of deflection. Thus for $\theta = \frac{\pi}{2}$, $\mathbf{V}_z$ must be zero. This results in the elimination of the terms with a dependence on $\cos(2^n\theta)'$. Due to symmetry the terms of $\sin(\theta)$ may similarly be eliminated.

This provides the following variation in $\mathbf{V}_z$ for the first three terms, with higher order terms following the same patten.

$$\mathbf{V}_z = ar\cos(\theta) + br^3\cos(3\theta) + cr^5\cos(5\theta) \tag{4.5}$$

To calculate the coefficients a b and c a full circular profile of the voltage is taken, this consisted of 800 points taken at a radius of 5 mm. A fast Furrier transform was then preformed. The resulting values then could be normalised to a 5 mm offset before being used as the variables.

$$V_z(circle) = A[2,800] \tag{4.6}$$

$$FFT(A[2,800]) \propto M[800] \tag{4.7}$$

$$a = M[2]/0.005^1 \tag{4.8}$$

$$b = M[4]/0.005^3 \tag{4.9}$$

$$b = M[6]/0.005^5 \tag{4.10}$$

where $V_z(circle)$ is the values taken from CST, placed in the two by eight hundred matrix $A[2,800]$, $M[800]$ is the result of the Furrier transform with $M[2]$ corresponding to the 2^{nd} term of the transform.

By comparing measurements of $\mathbf{V}_z$ at a range of offsets in an arc the from CST to the analytical values of a, b and c calculated the calculation can be checked for self consistency . To calculate the multipole components from CST the longitudinal voltage was calculated at a range offset's across a $\frac{\pi}{2}$ segment of the cavity.

The original oval shape was studied to see how the multipole components varied as they were the expected cause of the variance in the deflecting field. The comparison between multipole components and CST data is shown in Figure 4.2. Good agreement is shown close to the axis with the Fourier transform. To ensure good agreement with CST the original shape had to be taken to the seventh order term, implying large multipole components.

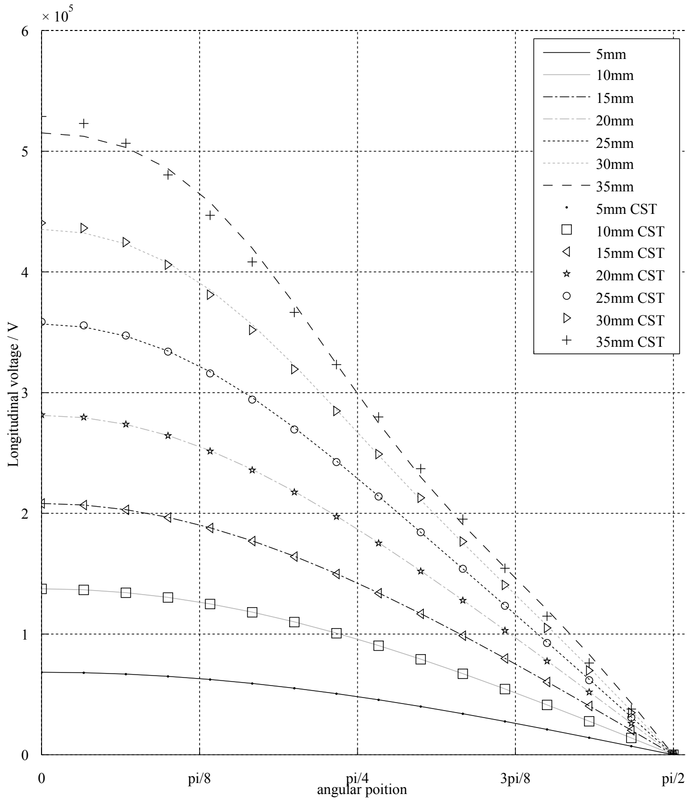

Figure 4.2: Fitting multipole measurements of 'Original' cavity to CST.

For the original shape the multipole components were calculated as[76];

Dipole $1.36 \cdot 10^7$

Sextupole $1.09 \cdot 10^9$

Decapole $1.22 \cdot 10^{12}$

These were compared to a D2 separation dipole that is currently installed on the LHC ring near interaction regions 1 and 2. The multipole components are on the same order of magnitude as the dipole magnets[76]. This is currently deemed acceptable, however full numerical simulations are required to check long term effects on the beam dynamics.

4.4 Voltage Variation in the Original Shape

The oval rods in the initial design were found to have significant variation in transverse voltage at increasing offset from the centre of the beam-pipe, this is shown in Figure 4.3.

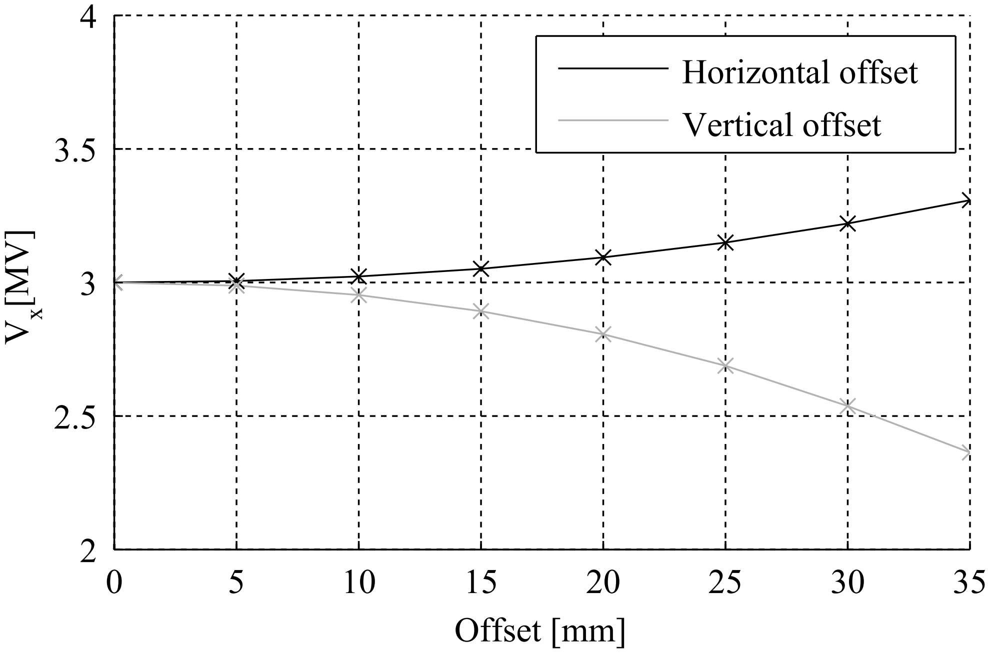

Figure 4.3: Variation in the transverse voltage ($\mathbf{V}_x$) against horizontal and vertical offset

The deflecting voltage depends greatly on the vertical offset, peaking at the centre of the beam-pipe. At a horizontal offset of 25 mm the vertical deflecting voltage was found to increase by 4.98 % with respect to the voltage in the centre, while a 25 mm horizontal offset lead to a decrease of 10.39 % in deflecting voltage. Closer to the rods field enhancement causes the transverse voltage to increase at increased offset.

The particularly large variation seen in the deflecting voltage can be attributed to the size of the rods, as seen in Section 4.7, where small rods produced a larger variation in deflecting voltage. Due to the constraints imposed on the size of the LHC crab cavity, cylindrical rods of a size large enough to eliminate this problem are unfeasible.

It is clear that circular rods have a large variation in deflecting voltage across the beam-pipe aperture, hence it was necessary to investigate other rod geometries to minimise the variation in transverse voltage. It is well known that the transverse electric field in between two infinite parallel plates is constant.

4.5 Pill Box Voltage Variation

The most simple electromagnetic cavity design is that of a pill box; a cylindrical cavity of length d and radius R_0. By looking at this shape we can compare the fields of mathematical models and real world designs to a simple crab cavity design. The longitudinal voltage in a pill box cavity can be calculated from the integral of the longitudinal electric field E_z at any choice of radial coordinate for any $\mathrm{TM}_{m\,n\,p}$mode [43].

Here, the position within the cavity is defined as the longitudinal position z, the radial angle θ , the radial offset as ρ and E_0 is the nominal time-dependent electric field. While applying this to the dipole mode $\mathrm{TM}_{1\,1\,0}$ there is no $\hat{\mathbf{z}}$ variation and the equation simplifies to;

$$V_z(\rho,\theta) = \int_{\frac{-d}{2}}^{\frac{d}{2}} E_z(\rho,\theta,z)dz \tag{4.11}$$

which becomes:

$$V_z(\rho,\theta) = V_0 J_1\left(\frac{\zeta_{11}\rho}{R_0}\right)\cos\left(\theta\right) \tag{4.12}$$

Where $V_0$is the nominal accelerating voltage and ζ_{11} in the first root of the first Bessel function J_1.

This can then be transformed into Cartesian coordinates the longitudinal voltage can be rewritten as:

$$\mathbf{V}_z(x,y) = V_0 J_1\left(\frac{\zeta_{11}\sqrt{x^2+y^2}}{R_0}\right)\frac{x}{\sqrt{x^2+y^2}} \tag{4.13}$$

From the Panofski Wenzel theorem,

$$V_{\perp=} - \frac{ic}{\omega}\int_0^d \nabla_\perp E_z(z,\frac{z}{c})dz \tag{4.14}$$

the deflecting component of this can derived as:

$$\mathbf{V}_x = \frac{c}{\omega}\frac{\partial \mathbf{V}_z}{\partial x} \tag{4.15}$$

With the parasitic deflection derived as:

$$\mathbf{V}_y = \frac{c}{\omega}\frac{\partial \mathbf{V}_z}{\partial y} \tag{4.16}$$

By performing a Taylor expansion on J_1, the behaviour of the deflecting and parasitic voltages can be examined and generalisations made on how they will behave close to the axis:

$$J_1\left(u\right) = \frac{u}{2} - \frac{u^3}{16} + \frac{u^5}{384} + \left(O^7...\right) \tag{4.17}$$

Substituting in the first 3 terms and ignoring terms of 7^{th} order and higher:

$$\begin{aligned}\mathbf{V}_z\left(x,y\right) &= V_0\left\{\frac{\zeta_{11}\sqrt{x^2+y^2}}{2R_0}\frac{x}{\sqrt{x^2+y^2}} - \left(\frac{\zeta_{11}\sqrt{x^2+y^2}}{R_0}\right)^3\frac{x}{16\sqrt{x^2+y^2}}\right.\\ &\quad \left. + \left(\frac{\zeta_{11}\sqrt{x^2+y^2}}{R_0}\right)^5\frac{x}{384\sqrt{x^2+y^2}} + \left(O^7...\right)\right\}\end{aligned} \tag{4.18}$$

This was then simplified by cancelling and grouping terms together to get:

$$\mathbf{V}_z\left(x,y\right) = V_0\left(\frac{\zeta_{11}x}{2R_0} - \frac{\zeta_{11}^3 x\left(x^2+y^2\right)}{16R_0^3} + \frac{\zeta_{11}^5 x\left(x^2+y^2\right)^2}{384R_0^5} + \left(O^7...\right)\right) \tag{4.19}$$

In the ideal case the dipole would vary with just x, thus being a uniform. The higher terms are distortions that lead to the variations in the deflecting voltage.

Then while using Equations 4.15 and 4.19, the deflecting voltage can be derived as:

$$\mathbf{V}_x = V_0\frac{c}{\omega}\left(\frac{\zeta_{11}}{2R_0} - \frac{3\zeta_{11}^3x^2}{16R_0^3} - \frac{\zeta_{11}^3y^2}{16R_0^3} + \frac{5\zeta_{11}^5x^4}{384R_0^5} + \frac{6\zeta_{11}^5x^2y^2}{384R_0^5} + \frac{\zeta_{11}^5y^4}{384R_0^5} + \left(O^7...\right)\right) \tag{4.20}$$

converting this back into θ and ρ with $x = \rho\cos\theta$ and $y = \theta\cos\theta$

$$\mathbf{V}_x = V_0\frac{c}{\omega}\frac{\zeta_{11}}{2R_0}\left(1 - \frac{\zeta_{11}^2\rho^2\left(2\cos^2\theta+1\right)}{8R_0^2} + \frac{\zeta_{11}^4\rho^4\left(5\cos^2\theta+\sin^2\theta\right)}{192R_0^4}\right) \tag{4.21}$$

Similarly, using Equation 4.16, the parasitic deflecting voltage can be derived as:

$$\mathbf{V}_y = V_0\frac{c}{\omega}\left(\frac{2\zeta_{11}^3yx}{16R_0^3} - \frac{4\zeta_{11}^5xy^3}{384R_0^5} - \frac{4\zeta_{11}x^3y}{384R_0^5} + \left(O^6...\right)\right) \tag{4.22}$$

and again converted back into $\theta$and ρ.

$$\mathbf{V}_y = V_0\frac{c}{\omega}\frac{\zeta_{11}^3}{8R_0^3}\left(\rho^2\cos\theta\sin\theta - \frac{\zeta_{11}^2\rho^4\cos\theta\sin\theta}{12R_0^2}\left(O^6...\right)\right) \tag{4.23}$$

The two voltages are normalized to the transverse voltage so the relative magnitudes of the deflecting voltage and the parasitic deflection across each of the differing cavities and to allow relative percentage changes to be tracked. The variation in $\mathbf{V}_x$is dominated by the ρ^2term, as seen in Equation 4.21. The ratio of the dipole amplitude to this term is $\frac{\zeta^2}{4R_0^2}$, hence the higher the cavity frequency, the larger the variation over a fixed distance. This is to be expected as the aperture becomes larger compared to the wavelength. At larger offsets, the variation can become quite profound as the ρ^4starts to become dominant. The initial variation depends more on the horizontal offset than the vertical by a factor of three. Likewise, the $\mathbf{V}_y$variation is also dominated by the ρ^2 term, as seen in 4.23, though it is zero on both the horizontal and vertical plane, and is largest at an angle of $\frac{\pi}{4}$ where the ratio of this term to the dipole is $\frac{\zeta^2}{8R_0^2}$.

$$\mathbf{V}_t(x,y) = \sqrt{\mathbf{V}_x\,(x,y)\,^2 + \mathbf{V}_y\,(x,y)\,^2} \tag{4.24}$$

$$\mathbf{V}_X\,(x,y) = \frac{\mathbf{V}_x(x,y)}{\mathbf{V}_t(0,0)} \tag{4.25}$$

$$\mathbf{V}_Y\,(x,y) = \frac{\mathbf{V}_y\,(x,y)}{\mathbf{V}_t\,(0,0)} \tag{4.26}$$

As the cavity properties for a pill box are dependent on the frequency, a value of 400 MHz was chosen for these calculations. This results in an angular frequency(ω) of $2.513 \times 10^9 s^{-1}$ and a wave number (k) of $8.383\,\mathrm{m}^{-1}$, which leads to a cavity radius (R_0) of 0.475 m, a wavelength (λ) of 0.749 m and a cavity length (d) of 0.375 m.

The cavity length is defined as

$$d = \frac{\lambda}{2} \tag{4.27}$$

and cavity radius is defined as:

$$R_0 = \frac{\zeta_{11}}{k} \tag{4.28}$$

Using these dimensions and plotting over the LHC beam pipe [42 mm], the behaviour of the deflecting voltage can be ascertained.

Figure 4.4shows a general Bessel-shaped fall in the $(\mathbf{V}_x)$, as expected over the sampled area, the decrease is more pronounced at increasing horizontal offset than the equivalent vertical offset. At an offset of $(30, 0)$, the deflecting

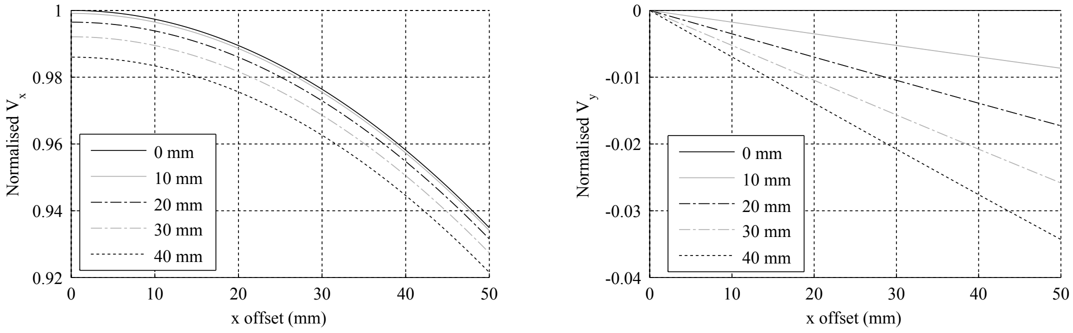

(a) (b)

Figure 4.4: Proportional deflecting voltage ($\mathbf{V}_x$) (a) and parasitic deflecting voltage ($\mathbf{V}_y$) (b) of a pillbox cavity at various offsets in the x and y direction, normalization to central transverse voltage, $\hat{x}$ is the direction of desired deflection.

voltage has dropped by 2.36 %, at position $(0, 30)$, it has dropped by 0.78%, and at (30@45 Deg), there is a drop of 1.40 %. For ($\mathbf{V}_y$), there is an almost linear drop, at increasing x and y offsets. At an offset of $(30, 0)$ and $(0, 30)$ there is no change in deflecting voltage as expected due to lying on the horizontal and vertical planes; at (30@45 Deg), there is a change of 0.7 %. These parameters are summarised in Table 4.1.

Method	Deflecting Drop (%)			Parasitic Increase (%)		
	$(0, 30)$	$(30, 0)$	(30@45 Deg)	$(0, 30)$	$(30, 0)$	(30@45 Deg)
Pill Box	-0.78	-2.36	-1.4	0	0	-0.7

Table 4.1: Summary of pillbox voltage variation

Figure 4.5 shows how increasing the frequency of the cavity leads to more rapid drop-off in deflecting voltage. This is because of the overall size of the cavity shrinking, due to increased frequency, providing a more pronounced effect in drop. Thus for flatter fields, a lower frequency (and thus larger cavity) is desired.

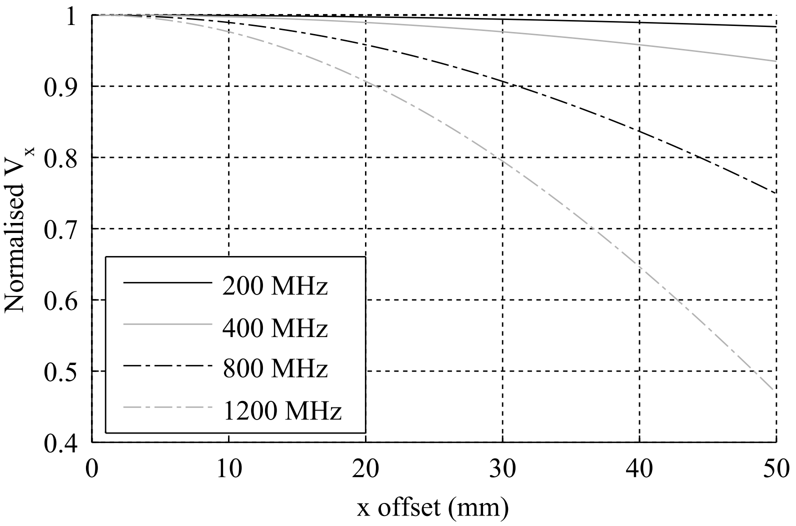

Figure 4.5: Variation in deflecting voltage across increasing x offsets at different frequencies. The y offset is at 0 mm.

4.6 Voltage Variation in Cylindrically-Symmetric Cavity with Beam-Pipes

The addition of beam-pipes to the pill box cavity causes the transverse field to flatten in the region of the beam-pipe. This flattening effect is caused by the hybridisation of the dipole mode that causes no variation in the deflecting voltage along the x axis. This allows deflecting cavities to have a far flatter field profile than the theoretical pill box.

$$k_0^2 = k_\perp^2 + k_z^2 \tag{4.29}$$

$$k_\perp^2 = \sqrt{k_0^2 - k_z^2} \tag{4.30}$$

$$k_\perp^2 = \sqrt{\left(\frac{\omega}{c}\right)^2 - \left(\frac{\omega}{v}\right)^2} \tag{4.31}$$

Here $k_0$is the wave number, $k_\perp$is the transverse wave number and k_z is the longitudinal wave number, $\omega$is the angle of frequency of the wave, v is the velocity of the wave and c is the speed of light.

As the velocity of the particles will be less than c, the transverse wave number will be imaginary, thus the complex Bessel function was used:

$$iI_n(A) \quad = \quad J_n(iA) \tag{4.32}$$

The longitudinal voltage is defined as [77]

$$\mathbf{V}_z(x,y) = V_0 I_1 \left(\frac{\omega}{c} \sqrt{\frac{1}{\beta^2} - 1\rho} \right) \frac{x}{\rho} \tag{4.33}$$

However, as β approaches 1, the complex Bessel function becomes increasingly small. Using the Taylor expansion of the complex Bessel function:

$$I_1\left(u\right) = \frac{u}{2} + \frac{u^3}{16} + \frac{u^5}{384} + \left(O^7...\right) \tag{4.34}$$

all the terms greater than $\frac{u}{2}$ can be ignored as they are of the order $\delta^3$and as such, would be completely dominated by the first term. This then leaves :

$$\mathbf{V}_z(x,y) \quad = \quad V_0 \frac{\omega x}{2c} \tag{4.35}$$

at very large β. This then results in zero parasitic voltage and a uniform deflecting voltage.

For a value of $\beta = 0.9999$, there is almost no variation in either the deflecting or parasitic voltage, at (30@45 Deg) the parasitic voltage has a value of 1.406×10^{-6} . These parameters are summarised in Table 4.2.

Depending on the β chosen for the cavity, particles travelling through at this speed will receive a greater or lesser uniform kick. At a low β, particles would travel through at a lower speed and thus will see more of the sinusoidal variation of the RF field. As β increases, this results in a more uniform deflecting voltage, as can be seen in 4.6.

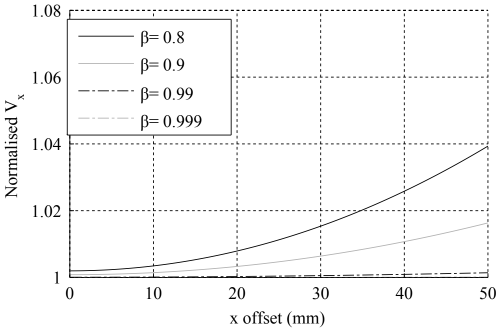

Figure 4.6: Proportional Deflecting voltage, at various x offsets across a range of β values

Method	Deflecting drop (%)			Parasitic increase (%)		
	$(0,30)$	$(30,0)$	$(30@45Deg)$	$(0,30)$	$(30,0)$	$(30@45Deg)$
C-Symmetric	0	0	0	0	0	1.406×10^{-6}

Table 4.2: Summary of cylindrically-symmetric voltage variation

4.7 Voltage Variation for a Four Rod Deflecting Cavity

The four rod deflecting cavity consists of two parallel rods with a break in them, inside an outer can. The fields of the deflecting mode supported by these rods can be approximated to those of the fields generated by statically charged rods. This approximation was examined by C. Leeman for the CEBAF experiment. The field between two charged rods is the same as the field between two infinite parallel lines separated by a distance, provided the rods sit on the equipotential lines. The centre of the rods is offset from the line of charge due to the presence of the other rod.

Assuming each cylinder has a radius of R and the centre is offset from the axis by A, the effective centres of any equipotential lines being generated will be at an offset of a from the axis.

$$a = \sqrt{A^2 - R^2} \tag{4.36}$$

The equipotentials are proportional to $\frac{1}{r^2}$, thus the potential at each point is space will be equal to the sum of these two charges.

$$E(x,y) = V_0\left(\frac{1}{r_+(x,y)} - \frac{1}{r_-(x,y)}\right) \tag{4.37}$$

$$r_+(x,y) = \sqrt{(x+a)^2 + y^2} \tag{4.38}$$

$$r_-(x,y) = \sqrt{(x+-a)^2 + y^2} \tag{4.39}$$

where the two effective charges are located at $\pm a$ and r_+ is oppositely charged to r_-.

A representation of these equipotentials are plotted in Figure 4.7. The rods could be placed on any of the equipotential lines.

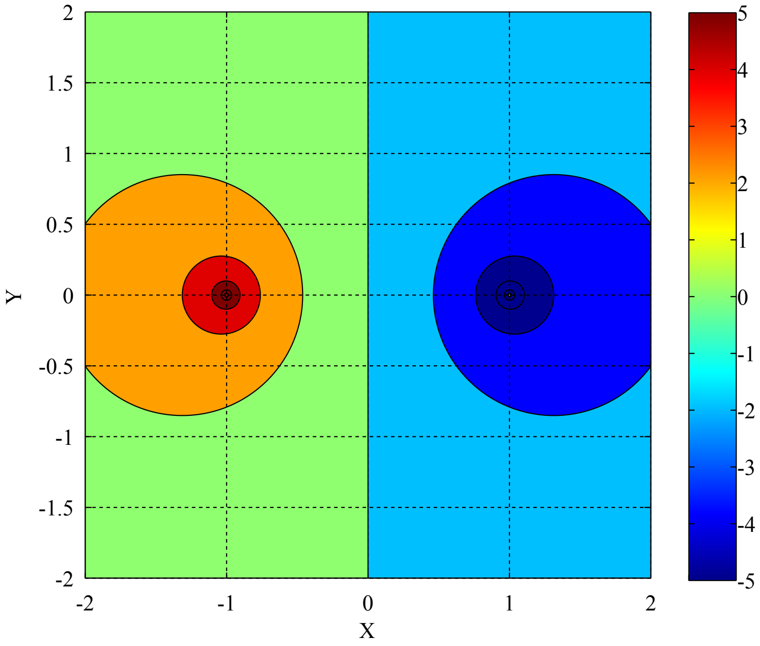

Figure 4.7: Representation of the equipotential lines generated by two line charges.

Integrating equation 4.37 in the $\hat{\mathbf{z}}$direction, the longitudinal voltage can be calculated as :

$$\mathbf{V}_z = V_0 ln \left(\frac{r_+(x,y)^2}{r_-(x,y)^2} \right) \tag{4.40}$$

Thus $\mathbf{V}_z$ is proportional to the $\log_e$ of $r_+(x,y)$ and $r_-(x,y)$.

The deflecting component of this is arithmetically calculated as:

$$\mathbf{V}_x = \frac{c}{\omega} \frac{\partial \mathbf{V}_z}{\partial x} \tag{4.41}$$

with the parasitic deflection calculated as:

$$\mathbf{V}_y = \frac{c}{\omega} \frac{\partial \mathbf{V}_z}{\partial y} \tag{4.42}$$

$$\mathbf{V}_x = V_0 \frac{c}{\omega} \frac{\partial}{\partial x} \left(ln \left(r_+(x,y)^2 - ln \left(r_-(x,y)^2 \right) \right) \right) \tag{4.43}$$

$$\mathbf{V}_x = V_0 \frac{c}{\omega} \left(\frac{2\,(a+x)}{\left((a+x)^2 + y^2 \right)} - \frac{2\,(x-a)}{\left((a-x)^2 + y^2 \right)} \right) \tag{4.44}$$

$$\mathbf{V}_y = V_0 \frac{c}{\omega} \frac{\partial}{\partial y} \left(ln \left(r_+(x,y)^2 - ln \left(r_-(x,y)^2 \right) \right) \right) \tag{4.45}$$

$$\mathbf{V}_y = V_0 \frac{c}{\omega} \left(\frac{2y}{\left((a+x)^2 + y^2 \right)} - \frac{2y}{\left((a-x)^2 + y^2 \right)} \right) \tag{4.46}$$

The two deflecting voltages were then once again normalised;

Our crab cavity design has roughly $A = 92mm$ and $R = 50mm$, so these dimensions are used for comparison. With four rods, the deflecting voltage decreases at increasing y offset, but at low y, close to the axis, the field is relatively flat with a slight increase at large x. As y increases, this increase levels out before becoming a decrease, see Figure 4.8. At an offset of $(30,0)$, the deflecting voltage has increased by 8.94%. At$(0,30)$, it has decreased by 7.59%, and at $(30@45Deg)$, there is a drop of 0.5%.

For the parasitic deflecting voltage 4.8b, there is a significant in drop in de-

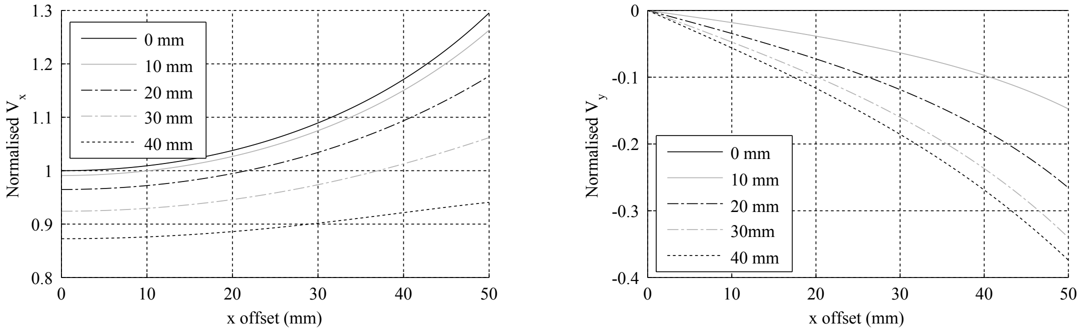

(a)

(b)

Figure 4.8: Proportional deflecting ($\mathbf{V}_x$) (a) and parasitic deflecting voltage ($\mathbf{V}_y$) (b) of the four rod deflecting cavity, normalised to the normal transverse voltage, with the parameters $A = 92mm$ and $R = 50mm$.

flecting voltage at increasing offset. At an offset of$(30, 0)$ and $(0, 30)$ there is no change in deflecting voltage due to this lying on the x axis, at $(30@45Deg)$, there is a drop of 7.26%. These results are summarised in Table 4.3.

Method	Deflecting drop (%)			Parasitic increase (%)		
	$(0,30)$	$(30,0)$	$(30@45Deg)$	$(0,30)$	$(30,0)$	$(30@45Deg)$
Four rod	8.94	-7.59	0.5	0	0	-7.26

Table 4.3: Summary of four rod deflecting voltage variation

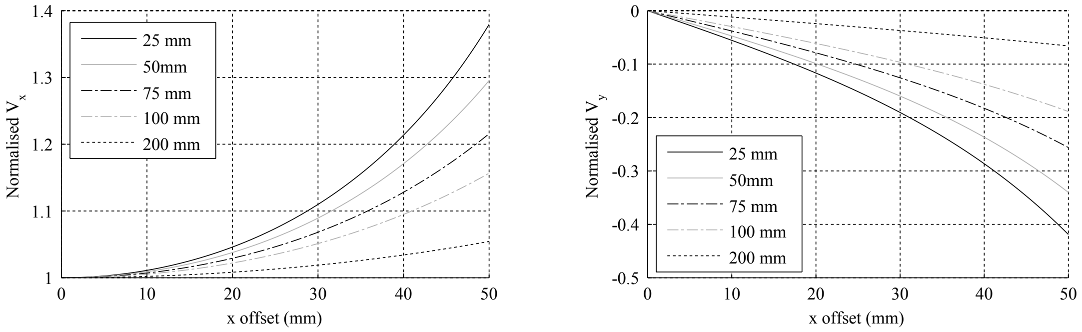

(a)

(b)

Figure 4.9: Proportional deflecting voltage ($\mathbf{V}_x$) (a) and parasitic deflecting voltage ($\mathbf{V}_y$) (b) of the four rod deflecting cavity across a range R values with $A - R = 42mm$.

Assuming $A - R = const$, at increasingly large rod radii, the deflecting voltage becomes ever flatter as the rods begin to resemble flat surfaces and the charges are moved apart. The large radii of the rods begins to resemble parallel plates. This leads to an almost uniform field across the aperture see 4.9.

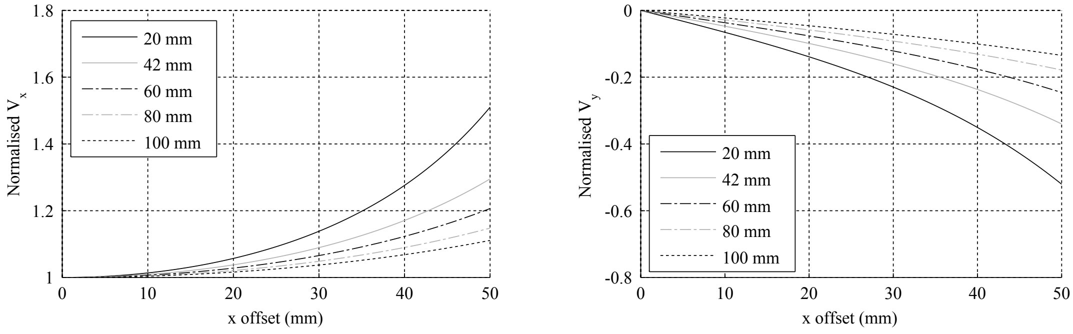

(a) (b)

Figure 4.10: Proportional deflecting voltage ($\mathbf{V}_x$) (a) and parasitic deflecting voltage ($\mathbf{V}_y$) (b) of the four rod deflecting cavity with $R = 50mm$ across a range of τ where $A = R + \tau$.

If the size of the rod remains constant but the distance between the rods increases, increasing τ with $A = R + \tau$, the fields again become flatter as the position of the charges move further apart. This has a an almost identical effect to increasing the rod radii, where the charge location changes. This causes the equipotential lines around these charges to be located around very distant points, effectively part of a very large circle, which causes the fields to again behave like parallel plates, see Figure 4.10.

4.8 Voltage Comparison

The variation in the deflecting and parasitic voltages for the three cavities studied is presented in Table 4.4.

Method	Deflecting variation (%)			Parasitic increase (%)
	$(0,30)$	$(30,0)$	(30@45 Deg)	(30@45 Deg)
Pill Box 400 MHz	-0.78	-2.36	-1.4	-0.7
Pill Box 800 MHz	-3.13	-9.32	-5.54	-2.76
Symmetric with beam-pipes	0	0	0	1.406×10^{-6}
4 rod (A= 92 mm, R=50 mm)	8.94	-7.59	0.5	-7.26

Table 4.4: Comparison in deflecting voltages at chosen points for a pillbox, a cylindrically-symmetric cavity with beam pipes and a four rod deflecting cavity.

The pillbox cavity offers insight into how the deflecting and parasitic voltages vary inside the cavity at a range of offsets. There is little change close to the axis, but the variation becomes more pronounced at increased offsets. The cylindrically-symmetric cavity obviously provides the most uniform deflecting voltage, however this is only true for $\beta \sim 1$ and some variation is seen when cavities are designed for a lower β. Although the 4RCC has significant variation, the percentage change in both the deflecting and parasitic voltage could be greatly reduced by altering the size of the rods or by increasing the separation between the rods. This could allow non-cylindrical rod shapes to provide a more uniform deflecting voltage.

In all cases, the parasitic voltage is not seen on either the x or y axis. The parasitic voltages dependence on increased offset, away from the horizontal or vertical axes, allows design considerations to be taken into account to reduce its presence in the case of the four rod design.

4.9 Parallel Plates

To reduce the change in transverse voltage at various offsets, a study was preformed on simple plate-like rods. It is known from electrostatics that two infinite parallel plates will have flat equipotential lines between them. As the width of the plates decreases, fringing fields at the edges start to play a role in the linearity of the equipotentials. This effect is similar to increasing the rod radii greatly in a four rod cavity. The variation in deflecting voltage caused by effectively flat rods was investigated.

As the plate length increases, there is an exponential drop in deflecting voltage variation for both the vertical and horizontal directions. The flat equipotentials created by the rod shape result in the desired uniform shape. However as the length of the rods increased, there was a significant drop in transverse R/Q as seen in Figure 4.12a due to a decrease in transverse voltage. The peak elec-

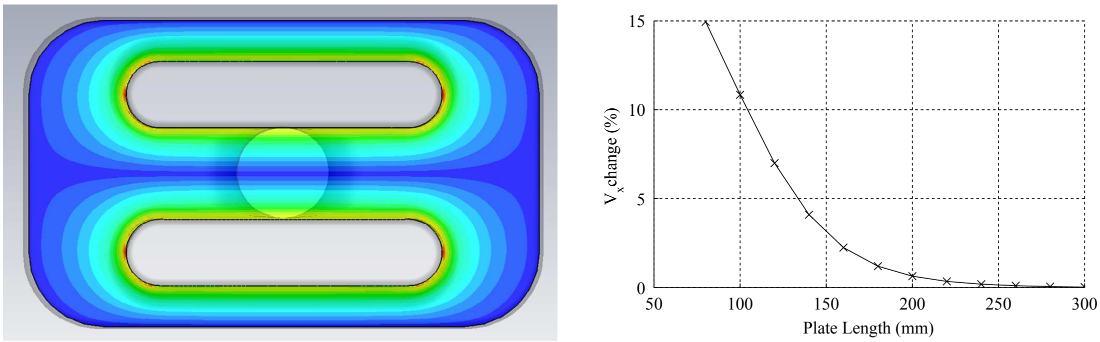

(a) (b)

Figure 4.11: The flat equipotantials of large plate like rods are shown in a. However, there is a large variation in transverse voltage at different plate lengths which is shown in figure b.

tric field followed the trend in transverse voltage and the peak field remained within 35 $\mathrm{MVm^{-1}} \pm 5\,\mathrm{MVm^{-1}}$. The peak magnetic field, as seen in Figure 4.12b, was highest around the beam pipe as the surface currents are forced to go around the beam pipe aperture. It was also high between the outer-can and the back of the rod due to the tight curve the surface currents must take to go around the outside of the can, with its peak at 66 $\mathrm{mT} \pm 5\,\mathrm{mT}$. This is not a significant increase in peak fields, however the LHC may require vertical crabbing, as such the cavity width cannot exceed 142 mm.

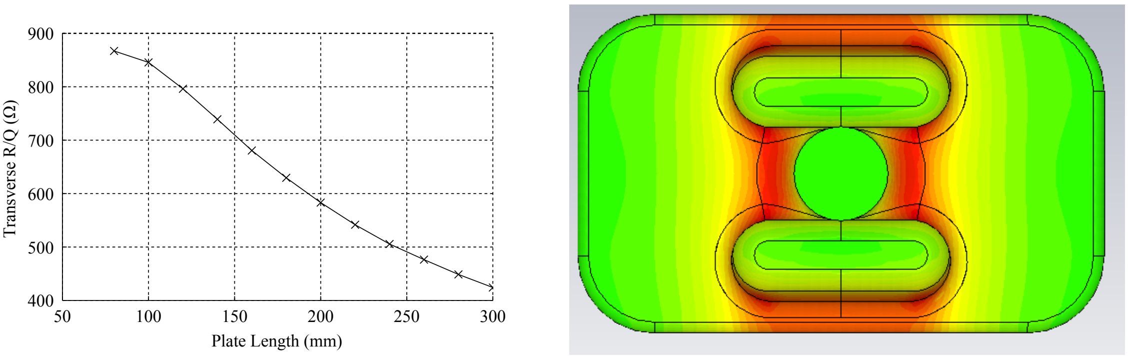

(a) (b)

Figure 4.12: R/Q variation at various plate lengths a, Peak surface magnetic field for plate length 200 mm b.

The large variation in R/Q as the rod width varies allows for the R/Q to be reduced if desired if the beam loading is too great.

4.10 Focus Electrodes for removal of sextupole component

As shown previously, flat plate like rods would be ideal, however it is not yet known if a vertical crossing angle is required at HL-LHC as well as the horizontal crossing angle. In order to accommodate a vertical crossing angle, the cavity must be compact in both horizontal and vertical dimensions. In addition, wider rods lead to a sharp drop in R/Q. Thus a solution is needed where the effect of wide plate-like rods is emulated by a shorter more compact shape. In fast stripline kickers the equipotential lines are bent back towards parallel by the addition of focusing electrodes. These focussing electrodes act to make the horizontal deflecting voltage uniform over the beam-pipe aperture. We use a similar approach by adding four electrodes to the plate, a cup-like structure is created. By varying the length and angle of these electrodes the strength of the sextupole component of the deflecting field can be varied and minimized as desired, hence creating a uniform deflecting voltage. The shape is shown in Figure 4.13.

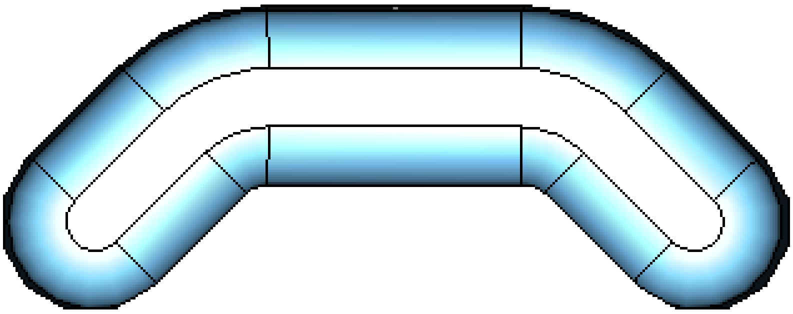

Figure 4.13: Shape of the plate-like rod with electrodes added

The geometry was simulated in CST microwave studio and a multipole expansion was used to identify the sextupole component of the deflecting voltage. As the electrodes are widened the angle required to remove the sextupole component decreases. For an arm width of 15 mm an angle of 26 deg is needed. However for an arm length of 30 mm an angle of only 8 deg is needed. Thus by adjusting the respective width and angle of the electrodes the sextupole component can be eliminated. Figure4.14 shows that for every arm length there is a corresponding angle that reduces the sextupole component to zero.

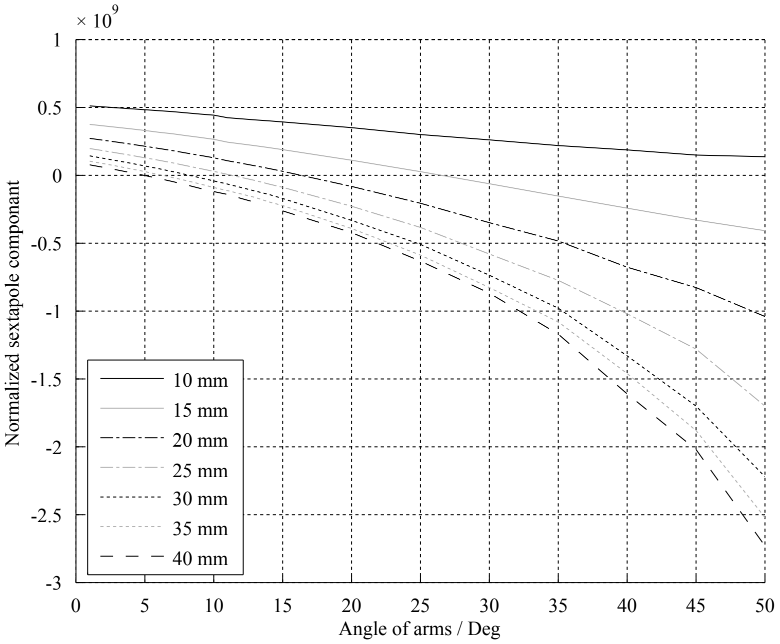

Figure 4.14: Strength of the sextupole term for different wing lengths across a range of angles.

The decision was made to keep the R/Q high and use a short plate and arm width. The focus electrodes added to the rods could not sit around the beam pipe in a manner that would be easy to manufacture due to small inconsistencies at the join between the beam pipe and rod base, hence it was necessary to round the edges. This altered the shape to that of a kidney, a more rounded shape that followed the profile of the beam pipe and could be optimized for better peak field performance. The general profile of the rod remains similar. This kidney-shaped rod is shown in figure 4.15 overlaid with a plate width of 20 mm, electrode width of 30 mm at a 30 deg angle and arm length 15 mm.

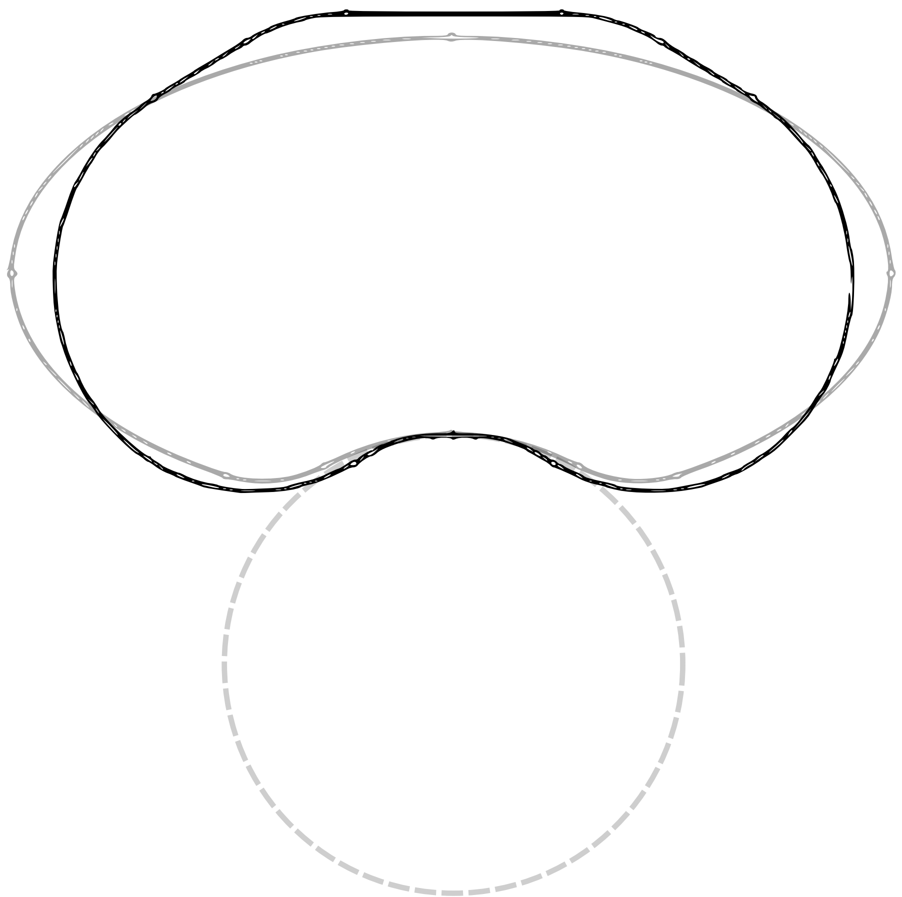

Figure 4.15: Overlay of 30 deg winged rod (black) over final kidney base shape (grey).

4.11 Kidney Shape

The longitudinal electric field at the tips of the rods for the original and revised geometries are shown in Figure 4.16, the improved field profile between the rods in the revised structure can clearly be seen.

The kidney shape has a dramatic effect, causing the equipotential lines across the centre of the beam pipe aperture to become linear. This is caused by the additional electrodes raising the area over which the electric field is flat. This can be seen in Figure 4.17.

The kidney-shaped rods keep the horizontal deflecting voltage uniform over a greater beam offset than the oval rods. This provides significant benefit as the variation over the first 15 mm is reduced to less than 0.1 %, however the variation increases to 3.74 % at an offset of 30 mm in the horizontal direction.

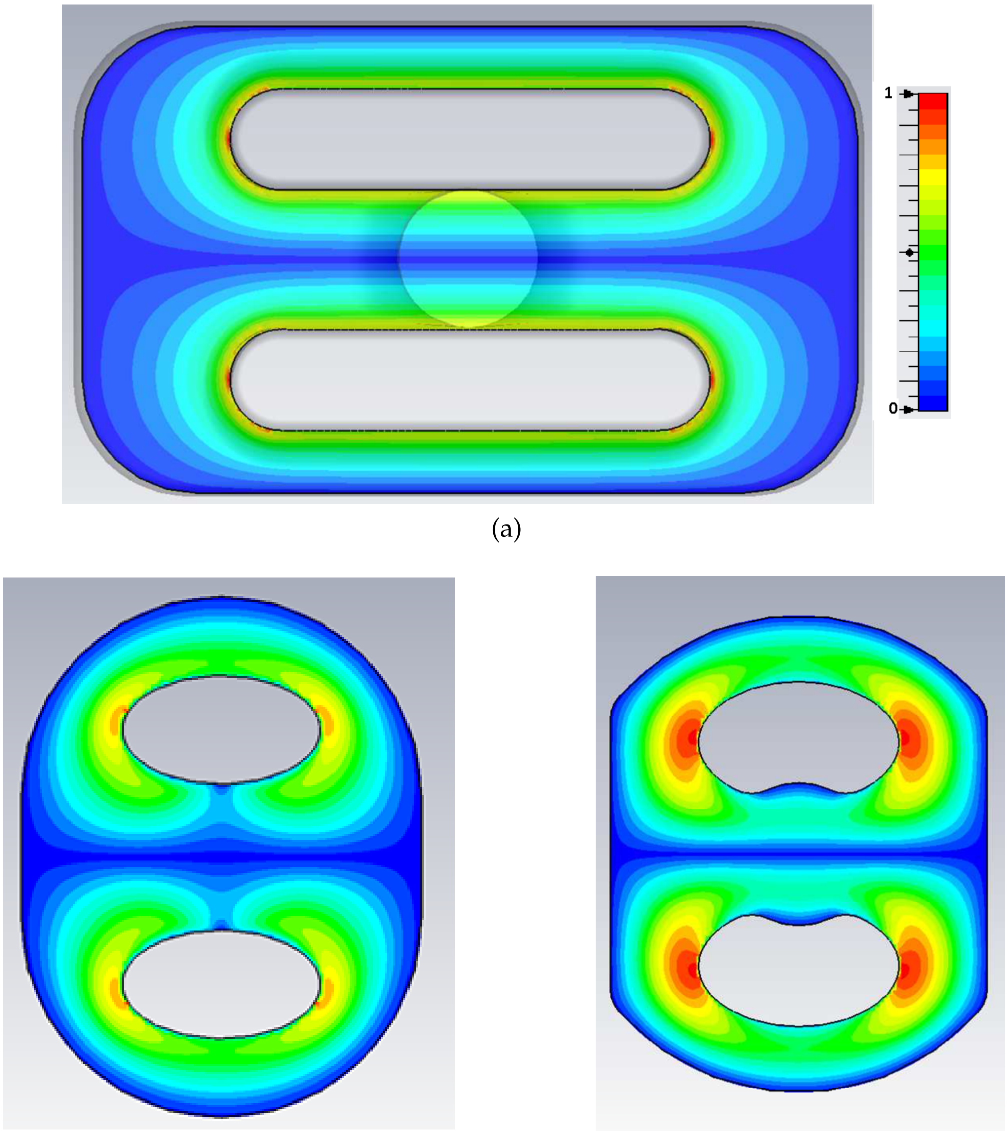

(a)

(b) (c)

Figure 4.16: Equipotential lines for plate-like rods a, oval rods b, and kidney-shaped rods c.

This should not be an issue as the beam should never be this far off-axis. The variation in the horizontal deflecting voltage at horizontal and vertical offsets are shown in figure 4.17.

The new kidney shape design was chosen as it allowed a good compromise between peak fields and flat deflecting voltage. The outside can required a slight redesign from a racetrack shape to that of a cut-off circle to allow the outer can to follow the profile of the rods and produce a uniform distance between the outer can and rod across the entire back surface of the rod hence avoiding high

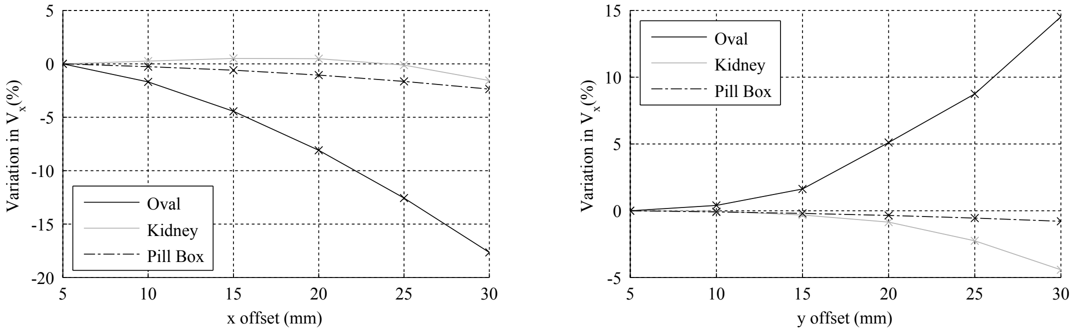

(a) (b)

Figure 4.17: Comparison of deflecting field between oval and kidney shaped rods and a pill box cavity as a function of horizontal offset.

surface magnetic fields. The large profile of the rod allowed increased rounding at the tip to further reduce any field enhancement effects, resulting in a slightly lower peak electric field.

The kidney shape has a peak electric field of 31.4 MV/m and a peak magnetic field of 63.3 mT at a deflecting voltage of 3 MV. The variation across the aperture is lower than that of a pillbox over small beam offsets. This structure has a R/Q of 912.

The kidney-shaped rods keep the deflecting voltage in both the horizontal and vertical directions uniform over a greater offset than the oval rods. This provides significant benefit as the variation over the first 15 mm is reduced to less than 0.1 %, however the variation increases to 3.74 % at an offset of 30 mm in the horizontal direction. This should not be an issue as the beam should never be this far off-axis.

4.12 Multipole components of new cavity

The multipole components of the new cavity with kidney-shaped rods were calculated. The comparison to simulation is shown in Figure 4.18 and good agreement is shown. This shape became known as the 'Aluminium' cavity as it was manufactured as an aluminium prototype for testing.

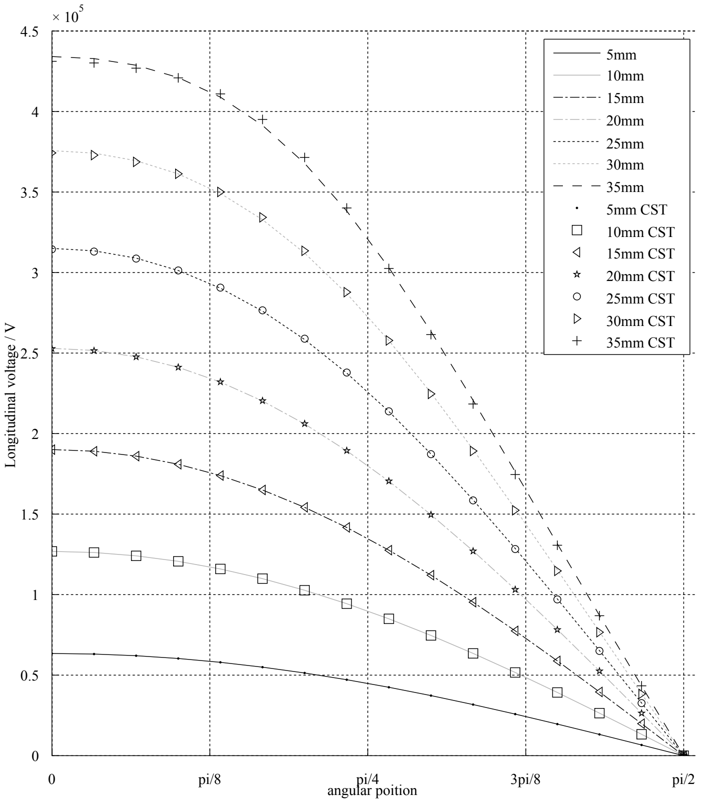

Figure 4.18: Fitting multipole measurements of 'Aluminium' cavity to CST.

During design and manufacture, some changes to the design were made to allow for a niobium prototype to be produced that could be machined with minimal expenditure on bulk niobium. . This design was named the 'Niowave' due to the company manufacturing it. As the Niowave cavity would be produced as a machine testable prototype that could be exposed to beam, the multipole components of this cavity were similarly calculated. This is shown in Figure 4.19

An alternative study was performed on the Niowave design as a comparison to other cavities proposed for the LHC upgrade using HFSS[76]. Although it gave good agreement with the HFSS calculation, it did not initially provide a good match with the CST data and required higher order terms to achieve acceptable agreement at larger offsets. The Niowave cavity required a $4^{th}$and 5^{th} term to be added to get good agreement above 25 mm. The comparison between

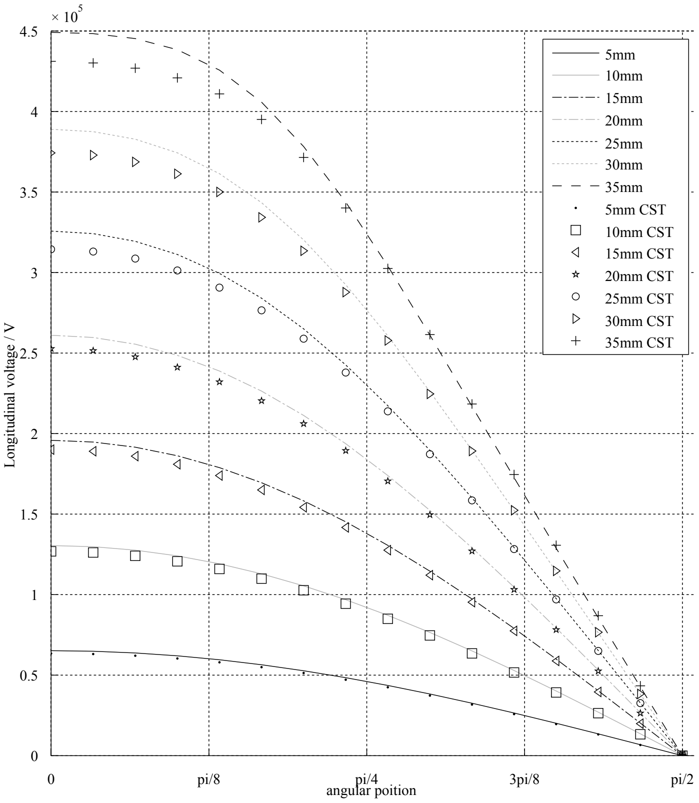

Figure 4.19: Higher order components for the 'Niowave' cavity

the Original, Aluminium, CST Niowave and HFSS Niowave are shown in Table 4.5.

Multipole component	Original	Aluminium	CST Niowave	HFSS Niowave
Dipole [a]	$1.36 \cdot 10^7$	$1.27 \cdot 10^7$	$1.30 \cdot 10^7$	$1.30 \cdot 10^7$
Sextupole [b]	$1.09 \cdot 10^9$	$-5.62 \cdot 10^7$	$1.18 \cdot 10^8$	$1.17 \cdot 10^8$
Decapole [c]	$1.22 \cdot 10^{12}$	$-1.47 \cdot 10^{11}$	$-1.89 \cdot 10^{11}$	$-1.90 \cdot 10^{11}$

Table 4.5: First three higher order components of the cavity designs

The multipole expansion shows good correlation to the values extracted from CST in all cases. Although in all cases at high offset, some discrepancy starts to appear, this misalignment can be attributed to a few possible effects. First, higher order terms above decapole would start to become expressed at such large offsets. Secondly, each higher order term has a proportionally less accurate field measurement in CST and a much higher mesh would be required. Thirdly, the Furrier transform had a sample size of 800 points, which limits the accuracy. Unfortunately the computing time to eliminate these discrepancies is disproportionate to the benefit.

The original cavity with oval rods has significantly larger sextupole and decapole components by an order of magnitude..

Both kidney shaped designs have very similar dipole components, however the Niowave cavity, that has smaller tips compared to the Aluminium cavity, has a positive sextupole instead of a negative one. The design difference between the two cavities is the size and shape of the tip of the rod. Thus between the two designs exists a shape that will have zero sextupole component.

The comparison between the Niowave cavity in CST and the HFSS model also shows very good agreement. Both the dipole and sextupole components are almost in perfect agreement. There is some discrepancy between the decapole component but both are still relatively close and it is expected that the inaccuracies mentioned earlier lead to this disagreement.

4.13 Summary

The uniformity of deflecting voltage required by the LHC was not initially met by the original oval shaped rods. Alternative methods of flattening the deflecting voltage were examined and a new shape was created. Parallel plates would provide a uniform mode, however they resulted in an unacceptable drop in R/Q and increased the size of the cavity beyond the limits that would allow the cavity to be rotated to enable vertical crossing. Focus electrodes were used to replicate the longer plate-like rods without compromising on the compact nature of the cavity. The electrodes allowed for the minimisation of multipole components that can adversely effect the dipole field.

The focus electrodes did not line up well with the geometry of the beam-pipe, and a new shape was created that followed the contour of the beam-pipe. The kidney shape provided all the advantages of the focus electrodes whilst following the same optimisation patterns as the oval shape.

The new cavity shape was designed with peak surface fields of 60.5 mT and 32.0 MM at 3 MV.

Parameter	Value
Full Gap	60 mm
Length	380.7 mm
Beam pipe radius	42 mm
Outer radius	140 mm
Beam pipe rounding	60 mm
Rod base and face rounding	20 mm
Tip rounding	20 mm
Tip width	110 mm
Tip breadth	70 mm
Mid width	72.5 mm
Mid breadth	125 mm
Base width	75 mm
Base breadth	140 mm
Emax @ 3MV	372.0 MV/m
Bmax @3MV	60.5 mT/MV/m
R/Q	912.67 Ω
Geometry factor	$62.8 \cdot 10^{-2}$

Table 4.6: Parameters for the final cavity.

This was made into an Aluminium test piece for further testing.

A second design for cold testing was machined out of niobium.

Chapter 5

Bead Pull

5.1 Introduction

To verify the simulated design of the cavity, an aluminum prototype was manufactured. This allowed for experimental verification of the 4RCC via bead pull.

It is possible to measure the electromagnetic properties of RF structures by perturbing the fields within them and measuring the response. By comparing the measured response to that of a theoretic response it is possible to characterise the RF structure.

A common perturbation technique that can characterise a cavity is a bead pull. This consists of a metal or dielectric object of known shape being pulled through the cavity by a thin wire. The wire is usually considerably smaller than the bead and made of a material that will not perturb the cavity significantly compared to the perturbation from the bead, in this case kevlar. The bead alters the frequency of the cavity as the local field patterns are disrupted by the change of local permeability and permittivity. The shift in frequency is proportional to the strength of the electric and magnetic fields.

Typically needles, disks and spheres are used, as the perturbation from these objects can be calculated reasonably easily. For modes with longitudinal electric fields, a needle is typically used as this interacts significantly more with the longitudinal electric field when pulled along the longitudinal axis. Transverse fields can be selected by using a disk. By using a dielectric object, only the electric fields can be measured allowing for the separation of the magnetic field.

5.2 Bead Pull Theory

By inserting a small metallic or dielectric object into a cavity it is possible to measure the perturbation in resonant frequency. The perturbation of the cavity frequency can be calculated from the perturbing objects disruption to the local permittivity and permeability, a new resonant frequency can then be measured and the shift, compared to the unperturbed cavity, calculated. The perturbation can then be used to calculate the fields of the cavity from the shift in frequency.

Assuming the perturbation is small, the effect of the perturbation has the following form. [78]

$$\frac{\omega-\omega_0}{\omega}=\frac{\int\left(\Delta\epsilon\mathbf{E}\cdot\mathbf{E}_0^*+\Delta\mu\mathbf{H}\cdot\mathbf{H}_0^*\right)\cdot dV}{\int\left(\epsilon_0\mathbf{E}\cdot\mathbf{E}_0^*+\mu_0\mathbf{H}\cdot\mathbf{H}_0^*\right)\cdot dV} \tag{5.1}$$

Where ω is the angular frequency, ϵ is the

In the case of small perturbations we can assume that : $\mathbf{E}\approx\mathbf{E}_0$, $\mathbf{H}\approx\mathbf{H}_0$ and $\omega\approx\omega_0$.

This allows for the simplification :

$$\frac{\omega-\omega_0}{\omega}=-\frac{\int\left(\Delta\epsilon\mathbf{E}\cdot\mathbf{E}_0^*+\Delta\mu\mathbf{H}\cdot\mathbf{H}_0^*\right)\cdot dV}{4W} \tag{5.2}$$

where W is the the total energy stored in the cavity.

This is then integrated to give :

$$\frac{\Delta f}{f_0} = \frac{1}{W}\left(\epsilon_0 \alpha_E E_0^2 + \mu_0 \alpha_m H_0^2\right) \tag{5.3}$$

where α_E is the the electric polarisability and α_M the magnetic polarisability of the object.

To profile the absolute electric and magnetic fields in the cavity, measurements are made on axis with both a dielectric and a metal bead. As the dielectric bead interacts with only the electric field it is possible to subtract this away from the metal profile to extract the magnetic field.

For a sphere the polarisability is given by

$$\alpha = -\pi a^3 \frac{\xi - 1}{\xi + 2} \tag{5.4}$$

where a is the radius of the sphere and ξ is the relative permeability μ_r or permittivity ϵ_r.

For a metal sphere where $\epsilon_r \rightarrow \infty$ and $\mu_r = 0$:

$$\alpha_E = -\pi a^3 \tag{5.5}$$

$$\alpha_M = \frac{1}{2}\pi a^3 \tag{5.6}$$

To calculate the electric field on axis the pure dielectric data can be used. As the shift in frequency can be either positive or negative the magnitude of the frequency shift must be used to avoid taking the root of a negative number.

$$|E| = \sqrt{\frac{|\Delta f|}{f_0 \frac{1}{W} \epsilon_0 \alpha_E}} \tag{5.7}$$

However for the magnetic field the frequency shift used must be adjusted to account for the electric field. Thus the magnetic frequency shift Δf_m can be calculated as:

$$\Delta f_m = (\Delta f_{Dia} \cdot \kappa) - |\Delta f_{metal}| \tag{5.8}$$

where the proportionality constant $\kappa = \frac{\xi - 1}{\xi + 2}$, Δf_{Dia} is the frequency shift due to the dielectric bead and Δf_{metal} is the shift due to the metal bead.

This allows for the magnetic field to then be calculated.

$$|B| = \sqrt{\frac{|\Delta f_m|}{f_0 \frac{1}{W} \mu_0 \alpha_M}} \tag{5.9}$$

To profile the transverse fields in the cavity, only the longitudinal electric field is of interest. To study the longitudinal field, E_0 was split into longitudinal and horizontal components E_t and E_z. [79]The assumption was made that the transverse effect would be significantly smaller than the longitudinal effect and could be neglected.

$$\frac{\Delta f}{f_0} = \frac{1}{W} \left(\epsilon_0 \alpha_{Ez} \left| E_z \right|^2 + \epsilon_0 \alpha_{Et} \left| E_t \right|^2 - \mu_0 \alpha_{mz} \left| H_z \right|^2 - \mu_0 \alpha_{mt} \left| H_t \right|^2 \right) \tag{5.10}$$

ı$|\ a$

The polarisability of the needle is calculated as α_E where $\beta = \frac{b}{a}$ with a being half the length of the needle and b being the radius of the needle. An example needle is shown in Figure 5.1.

$$\alpha_{Ez} = \frac{-\frac{2}{3}\pi a^3 (1-\beta^2)^{\frac{3}{2}}}{\ln \frac{1+(1-\beta^2)^{\frac{1}{2}}}{1-(1-\beta^2)^{\frac{1}{2}}} - 2(1-\beta^2)^{\frac{1}{2}}} \tag{5.11}$$

$$\alpha_{Mz} = \frac{-\frac{2}{3}\pi a^3 (1-\beta^2)^{\frac{3}{2}}}{\ln \frac{1+(1-\beta^2)^{\frac{1}{2}}}{1-(1-\beta^2)^{\frac{1}{2}}} - \frac{2(1-\beta^2)^{\frac{1}{2}}}{\beta^2}} \tag{5.12}$$

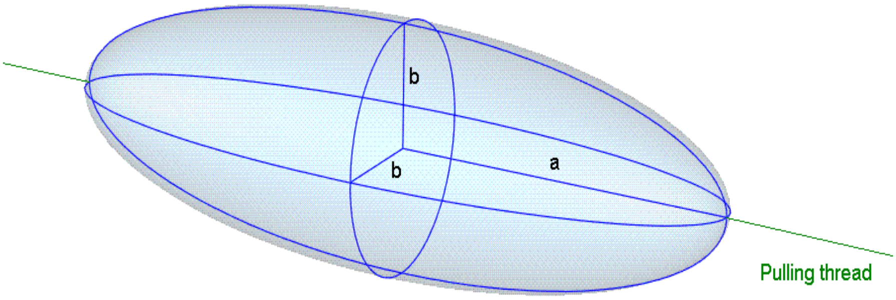

Figure 5.1: A stretched spheroid is used to represent a needle as the maths for a true cylinder requires extensive computation for little benefit. [79]

$$\alpha_{Et} = \frac{-\frac{4}{3}\pi a^3(1-\beta^2)^{\frac{3}{2}}}{\ln\frac{1+(1-\beta^2)^{\frac{1}{2}}}{1-(1-\beta^2)^{\frac{1}{2}}} - \frac{2(1-\beta^2)^{\frac{1}{2}}}{\beta^2}} \tag{5.13}$$

$$\alpha_{Mt} = \frac{-\frac{2}{3}\pi a^3(1-\beta^2)^{\frac{3}{2}}}{\ln\frac{1+(1-\beta^2)^{\frac{1}{2}}}{1-(1-\beta^2)^{\frac{1}{2}}} - \frac{2(1-\beta^2)^{\frac{1}{2}}(1-2\beta^2)}{\beta^2}} \tag{5.14}$$

Assuming that the effect of a needle on the transverse electric and magnetic field is small, the calculation can be simplified to:

$$\frac{\Delta f}{f_0} = \frac{1}{W}\epsilon_0\alpha_{E_z}E_z^2 \tag{5.15}$$

rearranging to get the electric field of the cavity,

$$|E_z| = \sqrt{\frac{|\Delta f|}{f_0\frac{1}{W}\epsilon_0\alpha_{E_z}}} \tag{5.16}$$

The shift in frequency can be calculated from the phase shift generated as the bead is pulled through the cavity for small $\Delta\theta$.

$$\Delta f = \frac{f_0}{2Q}\Delta\theta \tag{5.17}$$

which can then be integrated to get the voltage,

$$V_z \propto \int \left(\sqrt{\frac{|\Delta f|}{f_0}}\right) dz \tag{5.18}$$

$$= \int E_z dz \tag{5.19}$$

5.3 Aluminum Cavity

An aluminum prototype cavity was produced which could be tested using a bead pull technique to check the location of the modes within the cavity and ensure the fields were responding as designed.

The cavity was machined from bulk aluminum in three main sections, two identical end plates supporting two rods each and one outer can piece. The prototype was not intended for high power tests and as such only the inside surface was machined. The outside was left as part of the ingot, and was not machined to a thin surface as would be expected for a cold test.

The cavity setup is shown Figure 5.2. Coupling to the cavity was achieved via a pair of simple semi-rigid coax probes with loops in the central conductor. These were inserted through a series of probe holes that had been drilled in the outer can (not shown). A needle supported by a Kevlar wire was pulled through the cavity by the linear motor shown in Figure 5.2b. This provided a constant motion of 10 mm/s enabling the position withing the cavity to be obtained from the timing on the vector network analyzer (VNA). A self-tensioning system was used to ensure the Kevlar was kept taught by providing a constant resistance to the linear motor. The test rig consisted of a linear motor pulling a Kevlar string against a tensor unit, driven at a fixed speed. At each end of the rig a pair of stepper motors allowed the position of the Kevlar wire to be altered and aligned with the cavity in either the horizontal or vertical directions and are shown in Figure5.2a. The cavity is contained inside a mobile clean room to act as a pressure baffle against entry to the lab. The motors and network analyser are controlled through a LabView script that synchronises the linear motor and time domain data sampling.

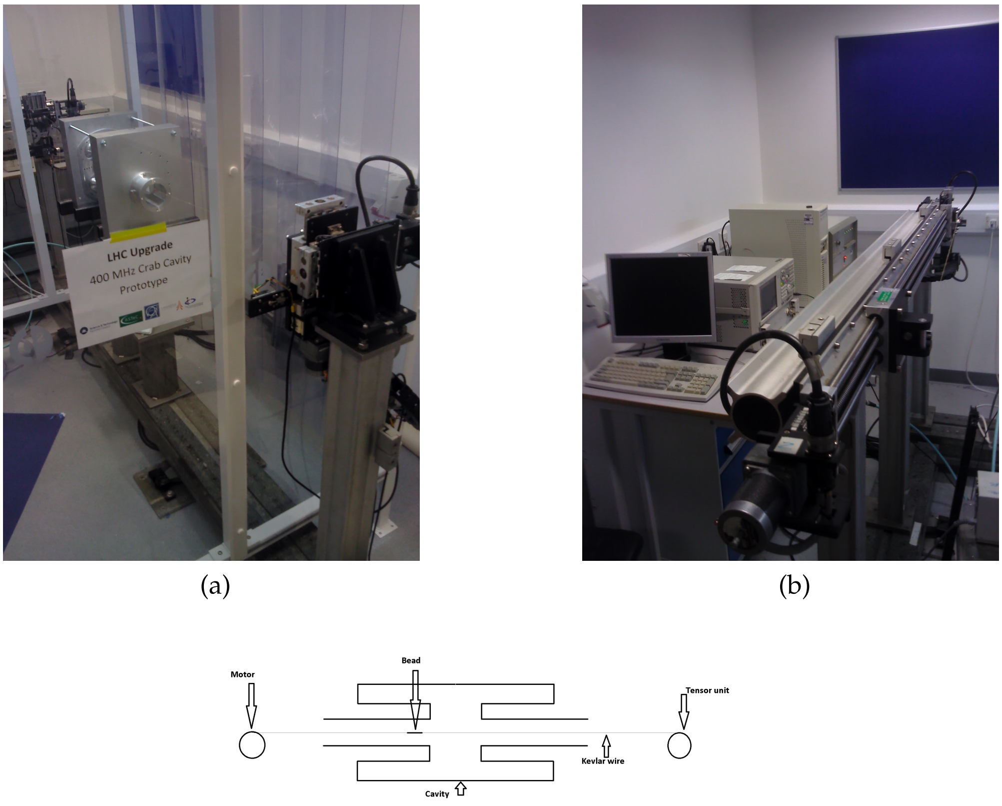

(a) (b)

(c)

Figure 5.2: Pictures of the beadpull setup

5.3.1 Needle Choice

By using the on axis measurement to correct transverse fields some of the error was reduced. Ideally just the longitudinal field will be picked up but as shown in Section 5.2 this is not the case due to the finite width of the needle required for threading.

$$\Delta f \propto \qquad f_1 E_z^2 + f_2 E_t^2 - f_4 B_\phi^2 \tag{5.20}$$

Where f_1, f_2 and f_4 is the susceptibility of the needle to longitudinal electric, transverse electric and transverse magnetic fields respectively[78].

The transverse fields were examined in CST and are shown in Figure 5.3.

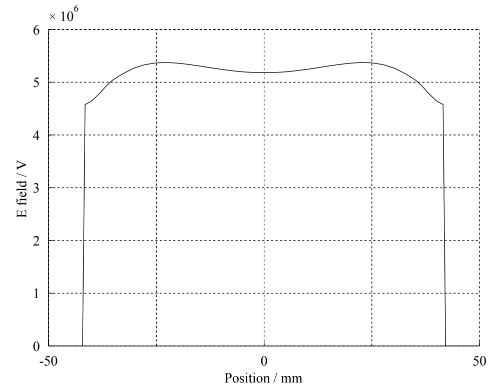

(a)

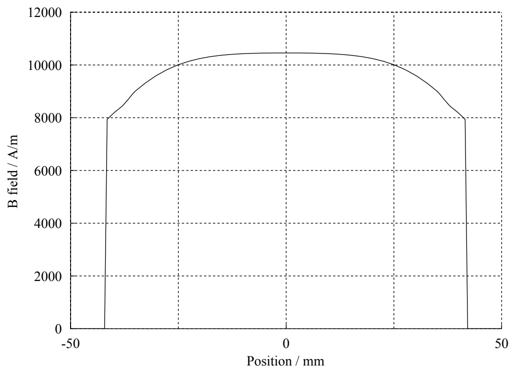

(b)

Figure 5.3: Transverse E field variation at electric field peak (a) and transverse B field variation at magnetic field peak (b) over the aperture at the longitudinal position of peak field.

As both fields show little variation across the main region of the aperture it was assumed that they could be treated as constant. A variation of 3.57 % was seen in the electric field and 4.23 % was seen in the magnetic field at 25 mm.

Taking the on axis measurement, where E_z should be zero, away from the off axis measurements, these errors can be reduced.

$$\Delta f \propto \qquad f_1 E_z^2 + \left(f_2\left(E_t^2 - E_{t0}^2\right) - f_4\left(B_\phi^2 - B_{\phi 0}^2\right)\right) \tag{5.21}$$

Where E_{t0} and B_{t0} are the on axis components.

The error produced by these transverse components can then be calculated from:

$$\%\,error = \qquad \frac{f_1 E_z^2 + \left(f_2\left(E_t^2 - E_{t0}^2\right) - f_4\left(B_\phi^2 - B_{\phi 0}^2\right)\right)}{f_1 E_z^2} \tag{5.22}$$

These errors were calculated using the peak field value taken from CST and compared to the transverse field, they are compared in table 5.1. By taking the on axis errors into consideration the the larger errors seen for small beads can be mitigated, this reduces the effect any longitudinal averaging could have.

Offset	Magnetic Error	Electric Error	Magnetic error with correction	Electric error with correction
10 mm	14.95 %	10.01 %	0.17 %	0.26 %
20 mm	3.64 %	2.72 %	0.24 %	0.26 %
30 mm	1.35 %	1.36 %	0.34 %	0.29 %
40 mm	0.49 %	0.98 %	0.39 %	0.42 %

Table 5.1: Comparison of errors with and without on axis correction

To compare the errors due to the variation of the longitudinal electric field over the needle length, the fields at a fixed offset, 10 mm, were taken from CST. The data was then averaged over possible rod lengths and the peak values of the electric field compared. If the averaging is suppressing data, the peak of the electric field will be lowered as the bead diminishes the peak. This is due to the perturbation of the rod being averaged across the entire rod length and thus the resolution of the peak field is diminished.

However the beads susceptibility to transverse fields increases as the bead becomes shorter. The ratio of the f_2 the transverse susceptibility is normalized to that of a 30 mm needle length.

Bead Length	Drop in Peak Field	Transverse Susceptibility
10 mm	0.15 %	9.31
30 mm	1.2 %	1
50 mm	4.78 %	0.36

Table 5.2: Comparison of drop in peak field due to averaging and transverse susceptibility of rod length.

The effect of averaging and the susceptibility to transverse fields is shown in Figure 5.2. A rod length of 30 mm is the best compromise between reduction in peak field due to averaging and susceptibility to transverse fields.

5.4 Comparison to CST

The first four modes of the cavity were checked against simulations in CST using spheres. Initially a metal sphere of diameter 11.1mm was pulled though the cavity, then a dielectric sphere of 10 mm was pulled though the cavity. As the dielectric sphere only interacts with the electric field, whilst the metal sphere interacts with both the magnetic and electric fields it is possible to subtract one from the other and obtain the independent fields.

5.4.1 Operating Mode

The operating mode of the cavity is of primary interest as this was the focus of the design. The electric field showed excellent agreement with the CST simulations lining up almost exactly. The magnetic field has considerable noise as it is taken from both the dielectric and metal data. However there is still reasonably good agreement with the CST data. The comparison between CST and beadpull data is shown in figure 5.4.

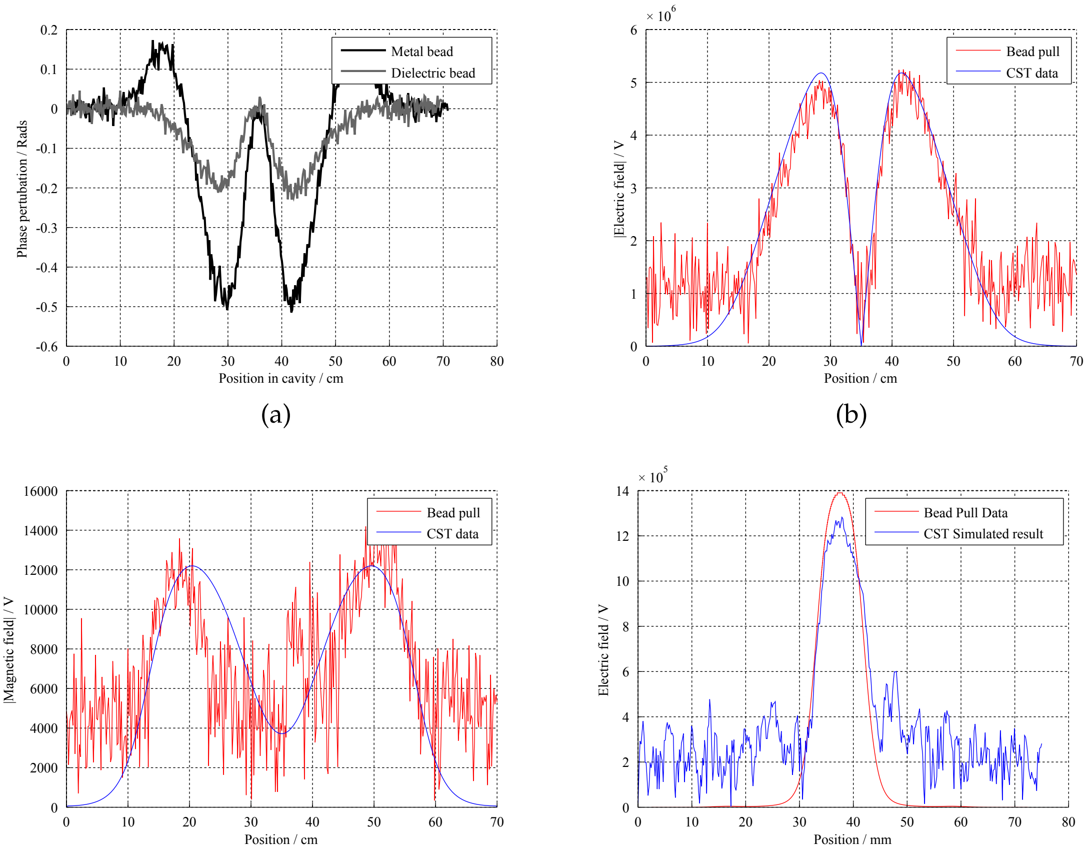

(a) (b) (c) (d)

Figure 5.4: The operating mode on axis for metal and dielectric spheres is shown in a. The comparison between the on axis electric field bead pull and CST at $U = 1\,\mathrm{J}$ is shown in b.The comparison between the on axis magnetic field bead pull and CST at $U = 1\,\mathrm{J}$ is shown in c. A comparison between CST and bead pull data for the longitudinal electric field is shown in d $U = 1\,\mathrm{J}$.

5.4.2 Lower order mode

The comparison between bead pull data and CST simulations is shown in Figure 5.5. The results show reasonable correlation to the simulation with the peak electric field where expected. However it is slightly lower than expected. The magnetic field was expected to be zero but due to the non zero noise offset seen in the longitudinal measurements a non zero value is returned. This non zero value consists of noise and is of the same level as the noise seen in higher order modes.

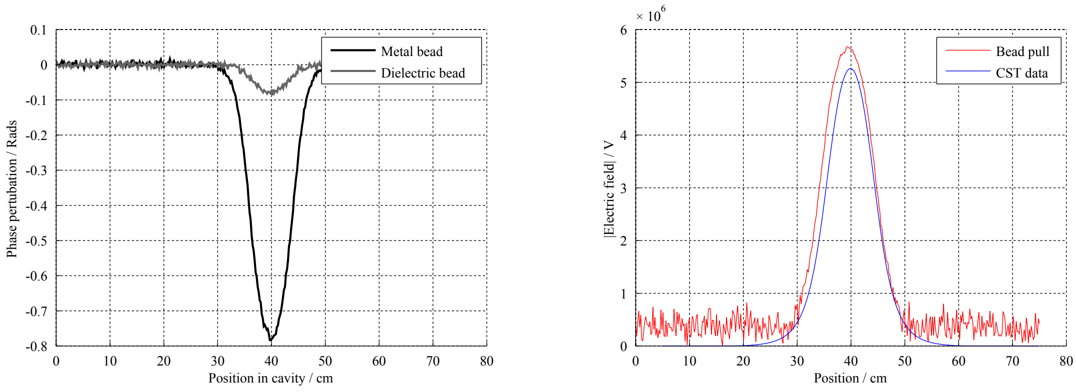

(a)

(b)

Figure 5.5: The lower order mode on axis metal and dielectric sphere is shown in a, the LOM electric field on axis compared to the calculated value from CST $U = 1\,\mathrm{J}$ is shown in b.

5.5 Bead Pull of Four Rod Cavity

Initial testing showed the bead pull set-up used, contained inherent errors in measurement. The needle used picked up a trace amount of transverse field.

Assuming the transverse components to be uniform over the aperture, by taking a measurement at the centre of the cavity where the E_z field should be zero the perturbation due to the transverse fields can be measured. This can be taken into consideration and accounted for in the processing of the data.

To account for this, the measured perturbation was split into $\frac{\Delta f_r}{f_0}$, the desired electric field, and $\frac{\Delta f_t}{f_0}$, the perturbation seen on axis due to the transverse fields. Figure 5.6a shows the raw unprocessed on axis data taken from the network analyser. This could then be cleaned up to reduce the noise via averaging over three points and normalized to zero and converted into a frequency shift, as seen in Figure 5.6b. The positive shift is due to the magnetic field while the negative shift is due to the electric field, thus the transverse perturbation $\frac{\Delta f_t}{f_0}$ is made up of both transverse electric and transverse magnetic components. If the on axis signal is further processed to acquire the electric field as for the off axis signals would the shift caused by the transverse fields can be clearly seen as four peaks as shown in Figure 5.6c. There should be no on axis field, as such this field would distort the results.

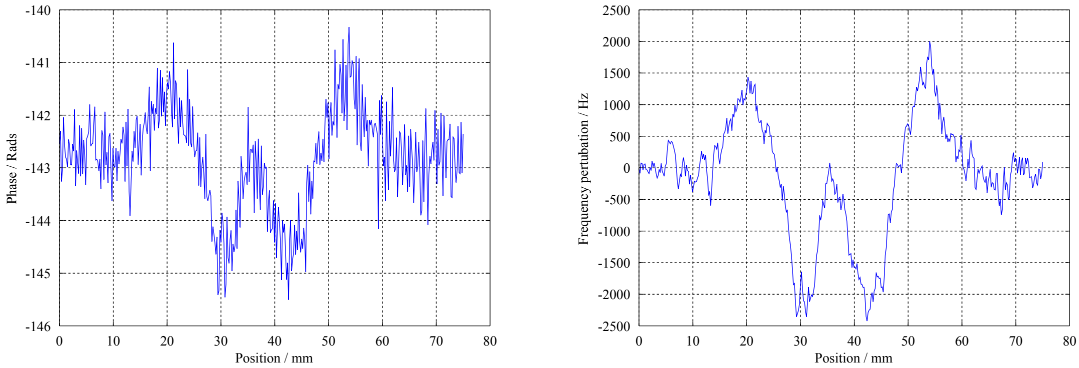

(a) Raw on axis data (b) Cleaned up on axis data

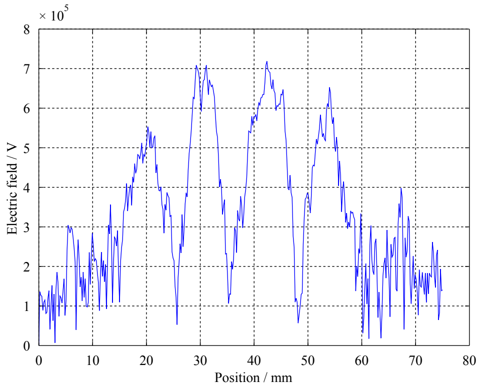

(c)

Figure 5.6: The raw on axis data is shown in a, the initial cleaning of the data is shown in b and the error due to the on axis electric and magnetic field error calculated from the measured frequency data if the on axis measurements id not accounted for is shown in c.

Additionally a significant amount of noise was also observed. Some of this noise can be attributed to the vibration of the needle caused by the tensor unit accommodating for the movement of the needle, this also leads to slightly different results depending on the direction the bead is being pulled. The main cause of noise is the poor signal received from the network analyser. The output power from the network analyser was set at $-17\,\text{dBm}$ due to problems in the existing Labview code used on the bead pull rig. Combined with the poor coupling from the small semi-rigid coax couplers that were used for the measurements the signal for the operating mode was at $-47\,\text{dB}$. This placed the signal only ~ 20 dB above the background noise of the room. Figure 5.7 shows the relative power levels of the noise and signal. Increasing the power and using alternative coupler designs would reduce this noise significantly, however this was not an option at the time of testing due to the power level being hard coded into the testing software.

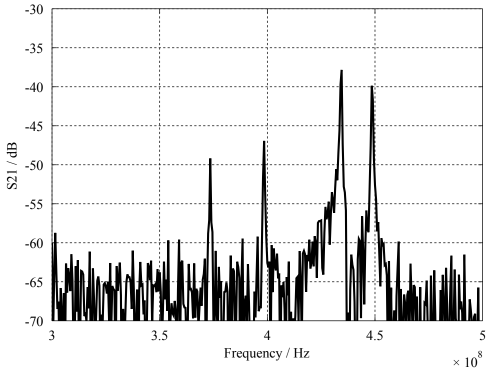

Figure 5.7: $S21$ Measurement of the Cavity

Due to the calculation taking the absolute value of the frequency shift, this results in a finite value of the voltage due to the noise when the field is integrated. This is most obvious at the start and end of each beadpull where the bead is in the beam pipe and should have no signal. V_{noise} is calculated by taking the difference in frequency shift for two identical runs and integrating to get a value. The noise signal used is shown in Figure 5.8.

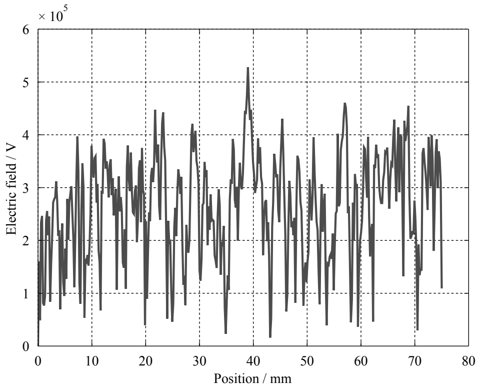

Figure 5.8: Noise measured by subtracting two identical measurements.

$$V_z \propto \int \left(\sqrt{\frac{|\Delta f|}{f_0} - \frac{|\Delta f_t|}{f_0}} \right) dz - V_{noise} \tag{5.23}$$

Where $|\Delta f|$is the total measured perturbation.

V_{noise} was calculated to have a value of $1.945 \cdot 10^5 V$

Figure 5.9a shows bead pull data for an off axis measurement. The central peak is the longitudinal electric field of the deflecting mode. The two smaller peaks to each side are the result of the transverse fields. As the transverse components depend weakly on their transverse position it is thus possible to account for the transverse fields at an offset by removing the transverse fields seen on axis. The expected value of the longitudinal measurement on axis is zero, as such, the on axis measurement can be assumed to be entirely transverse and equated to $\frac{\Delta f_t}{f_0}$.

Applying Equation 5.23, a clearer signal is achieved as seen in Figure 5.9b.

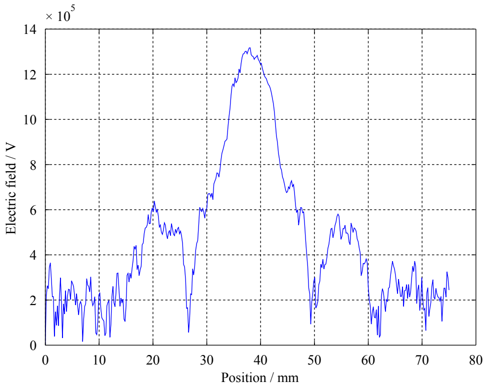

(a) Processed off axis data

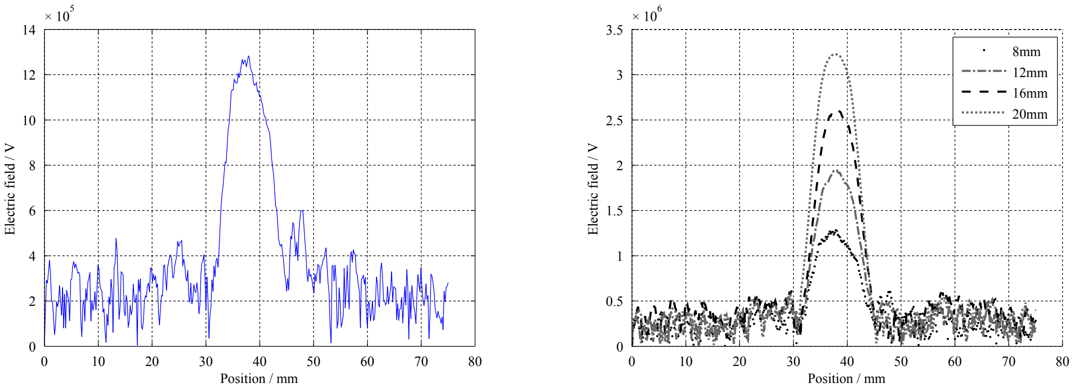

(b) Adjusted off axis data

(c) Four off-axis measurements.

Figure 5.9: Processing the off axis data and data ad various offsets.

Bead pulls were carried out to verify the designed field flatness. The measurements were carried out by pulling the chosen bead through the cavity at a constant speed of 1 cm/s. A network analyser was used to measure the perturbation in frequency caused by the bead. By using the perturbation the frequency shift could be calculated at each point, the frequency shift could then be used to calculate the electric field at each location. This could then be numerically integrated, providing the longitudinal voltage.

Figure 5.9c shows the processed data as electric field at increasing offset. This can then be integrated to calculate the voltage.

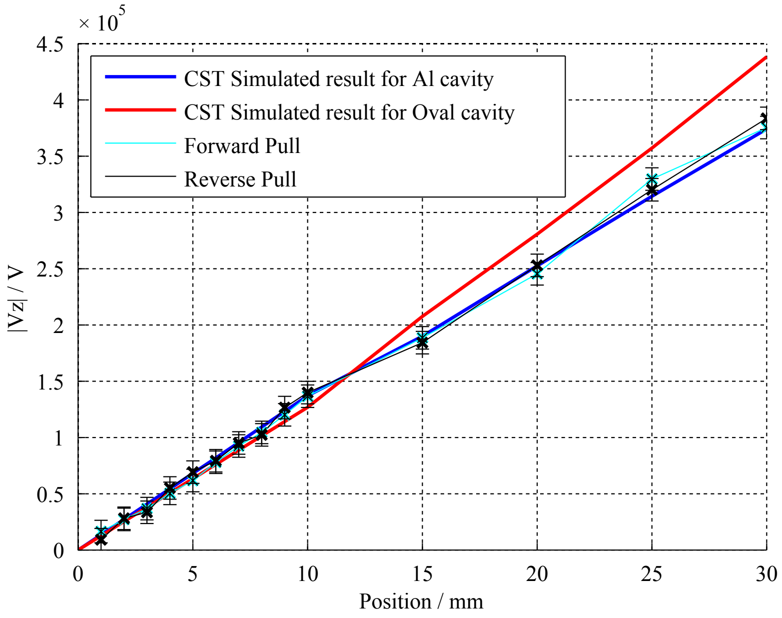

Figure 5.10: Comparison between simulation and bead pull measurements

Figure 5.10 shows the bead pull results against simulated results from CST. The bead pull measurements show good agreement with the results from CST that the longitudinal voltage is linearly dependent on the beam offset. This implies a uniform deflecting voltage across the aperture as desired.

The errors shows come from the statistical error in the Q that had a continual slight variation due to poor contacts from the couplers.

At small offset there is no appreciable difference in V_z between the two designs as any variation is too small to be measured well. This is due to the specified variation being in V_T which is a rate of change of V_z. At large offsets however this variation can be more easily measured. At an offset of 30 mm the bead pull measurement of transverse voltage variation is accurate to $\sim$ 2%.

5.6 Summary

The Aluminium cavity that was produced for experimentation provided measurements which confirmed the basic properties of the cavity and allowed for the fields within the cavity to be tested via bead-pull. Although significant noise was initially seen, through processing and adjustment taking on axis errors into count, useful measurements were able to be taken and compared to simulations from CST.

The cavity showed close agreement with the simulations despite errors calculated. The field uniformity lies within the error of the measurement and as such is assumed to be within tolerance as no major deviation was seen.

The fields of the cavity match well with the expected fields as calculated from CST for both the operating mode and the lower order mode. The good correlation with the expected results through bead pull implies the cavity is operating as designed. The bead pull can clearly tell the difference between the oval design and aluminium designs.

Chapter 6

Multipacting

6.1 Introduction

A major limiting factor in many RF cavities is multipacting. Multipacting is the build-up of unwanted electrons that absorb the RF power within the cavity system, which reduces the energy available to the beam and limits gradient[80, 81, 82]. The initial build up of electrons is caused by an exponential cascade of secondary electrons until a steady state of saturation is reached. The electron population is sustained by secondary emission of electrons from impacts with the surface.

Multipacting can thus be a 'show stopper' for a cavity design, as it can render the entire cavity unusable if it cannot be processed through. The LHC-4R crab cavity operates in a 400 MHz dipole like mode. Dipole cylindrical cavities at lower frequencies, below $\sim 1.5\,\mathrm{GHz}$, have been shown to exhibit multipacting in the iris region[81]. The LHC-4R crab cavity was examined for multipacting to ensure it did not multipact in the desired region of operation. Full 3D simulations using *CST Particle studio* were undertaken following a previously benchmarked procedure to look for multipacting in the cavity. The results of this study follow.

6.2 Theory of Multipacting

Multiactor was first seen between two surfaces supporting an RF field [83], but it was first categorized and shown to be a problem some years later[82].

Multipacting consists of the buildup of electrons within a system that is self-sustaining. The RF field provides the power that allows the osculation to perpetuate, while the repeated impacts with the surface or surfaces provide secondary electrons to increase the electron count. Initially this is often seen as an exponential build up. The process eventually saturates as the number of secondary electrons produced for every impact approaches unity. If the average number of electrons emitted is below unity, the total number of electrons in the system will decrease over time and the electron cloud will dissipate.

The secondary electrons produced from an initial incident electron can be generated in one of three ways:

- Back scattered or elastically-scattered electrons are those that are effectively reflected back off of the surface.
- Re-diffused are those that are absorbed into the surface of the material, but contain enough energy to break free from the surface a short time later.
- True secondaries are those that are produced from within the surface of the material by the incident electron and are usually accompanied by on of the other events.

The Ferman-Pivi model treats the back-scattered and re-defused electrons as single electron events, thus each incident electron can only produce a single electron as a secondary electron. The true secondaries are generally only involved in events where the number of secondary electrons is greater than one. Although this is not a true model of the electron behavior - a secondary electron could be generated, and escape, while the incident electron is trapped within the surface - the model was found to fit. This is shown in Figure 6.1. The number of electrons generated is known as the secondary emission yield (SEY).

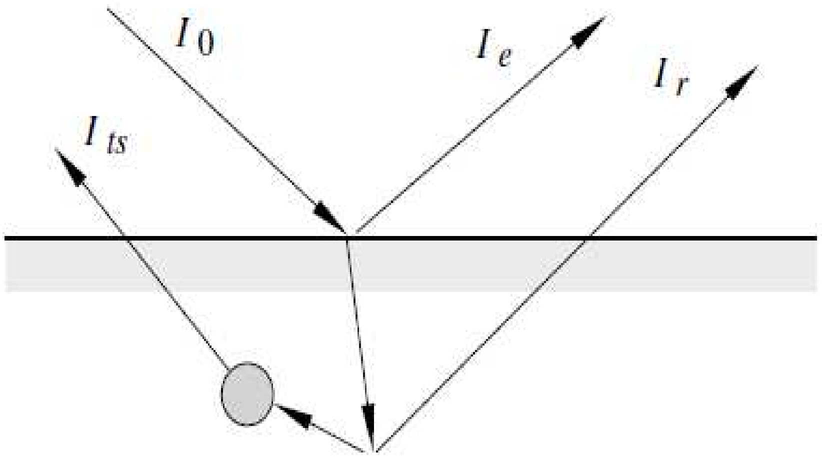

Figure 6.1: Sketch of the three different modes of interaction that can cause secondary electrons. The blob represents the formation of secondary electrons.[80]

The three modes of secondary generation are each probabilistic and based primarily on the incident energy, the incident angle has been shown to vary the exact number but has been shown to be insensitive to the angle of incident. The component make up of the total observable secondary electron yield is shown in Figure 6.2.

As well as the true secondaries varying with impact energy, the total number of secondary electrons for any given impact energy can also vary. Figure 6.3 shows the comparison between the number of secondaries produced for both stainless steel and copper. The initial high peak at one is due to the re-defused and elastically-scattered electrons. For copper, the second peak in average secondaries is between 2 and 3. Stainless steel has a far higher number of secondaries produced, although with lower probabality of being produced. This is important to the simulation and mathematical representation of multipacting as the upper bound on the number of secondary electrons produced must not cut off any important data.

For multipacting to take place, the electrons must cross the distance between the two surfaces in half an RF cycle or odd multiples of it, such that the returning electron will see the reverse field and be able to return to the initial emission site.

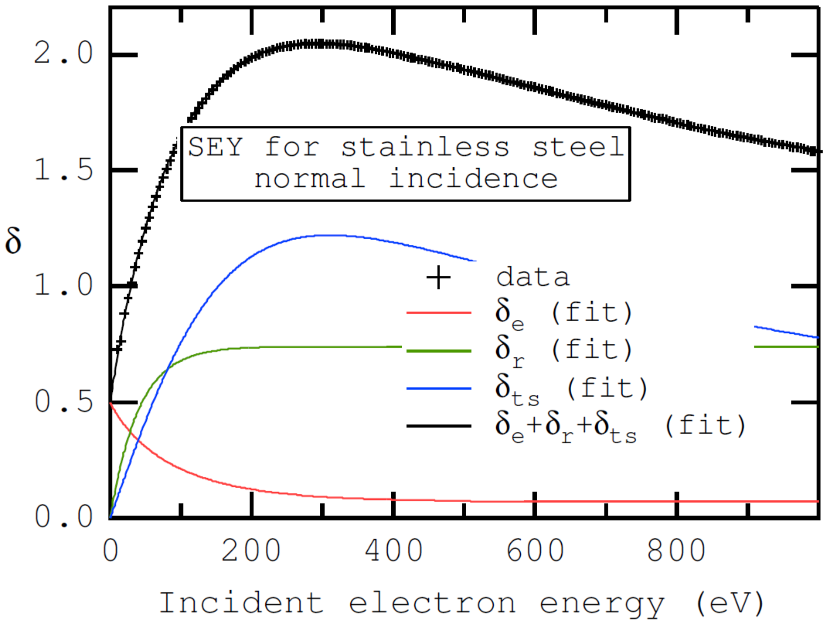

Figure 6.2: The probability of a secondary electron over a range of impact energies for stainless steel from the SLAC 304 rolled sheet cavity [80].

When several cycles of RF field are required between emission and impact this is known as 'higher order multipacting'.

The exact phase, amplitude and emission position are not needed as it has been shown that the effect is self focusing and will stabilize itself [82, 84]. This means that re-diffused or true secondary electrons that are slightly out of phase and position will still contribute to the build up of electrons, even though they are not released from the theoretical point of multipacting. This also aids with simulation as it allows for the initial seeding of electrons to be sparse but still cover the full range of phase space and emission site location across the surface of the cavity.

Multipactor can become a serious problem for SRF cavities as it can cause heating on the cavity wall, which will lead to a quench.

Multipactor has traditionally been seen on the equator of accelerating cavities [85]. This led to developments in the shape of the outer equator of accelerating cavities to suppress multipacting by decreasing the orbit of the electrons until they lack the energy to produce secondaries. The standard elliptical cell

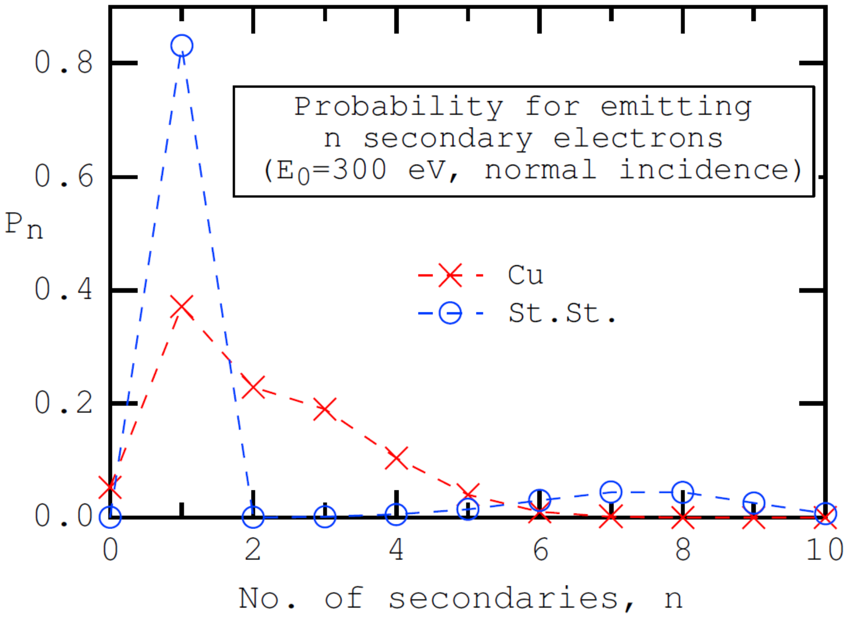

Figure 6.3: The variation in the number of secondary electrons emitted from the surface of copper and stainless steel at 300 ev [80].

design seen in most cylindrically symmetric cavities is partly due to this.

In deflecting cavities, the mode orientation does not allow for the equatorial multipacting. Instead, multipactor regions are found around the iris and beam pipe regions where high magnetic field is able to create electron orbits in an arc around the curved surface. This has been shown in many deflecting cavities. This was seen in the KEKB crab cavity and was processed through.[86]. Studies have shown that this effect is predictable as the orbits of the electrons depend on the local magnetic field and the frequency of the oscillation[81].

$$B_0 = \frac{\omega m \pi}{2e} \tag{6.1}$$

where B_0 is the magnetic field ω is the angular frequency , m is the mass of an electron and e is the charge on an electron.

Using 400 MHz as the frequency of the cavity, a magnetic field of 22.44 mT on the surface of the iris is expected to produce iris/beampipe aperture multipacting. For the 4RCC, the magnetic field resonance condition occurs at at approximately 2 MV deflecting voltage.

6.3 Simulation of Multipacting

To simulate multipacting within a chosen structure *CST Particle studio* can be used. It has been previously bench-marked on waveguide and cavities. CST particle tracking is used instead of particle in cell as it allows the fields to be calculated separately at high mesh and imported for tracking so the fields do not need to be re-run for every simulation. The initial fields were calculated at 200 lines per wavelength to ensure accurate fields near the surface and the tracking solver ran at 120 lines per wavelength.

To determine if multipacting is present, the number of electrons emitted from the surface of the cavity must be measured. Initially electrons are emitted over a large area. Electrons not involved in multipacting are absorbed within one or two cycles while the multipacting electrons quickly dominate. This is then compared to the total number of impacts that generated these electrons. By dividing the number of secondaries produced by the number of impacts, the average secondary emission yield ($< SEY >$) can be calculated.

$$< SEY >= \frac{number\, of\, secondaries}{number\, of\, impacts} \tag{6.2}$$

If the $< SEY >$ is greater than one then the total number of electrons within the cavity will grow and this will be an indicator of multipacting. The number of electron in the cavity ,n_e, increases as $n_e =< SEY >^{\#rf}$, where $\#rf$ is the number of RF cycles or impacts. If the $< SEY >$ falls below one then the number of electron will fall away to zero as each cycle reduces the total.

The solid object can then have SEY emission models applied to it to enable the statistical models described in section to be implemented. The previously calculated fields can be imported and be varied through phase and amplitude to enable a full sweep across all phases and up to and past the desired region of interest.

Faces within the shape can then be selected as sites for releasing electrons.

The level of seeding was adjusted so that there was approximately 1 electron per sq. cm . If the number is too high, the solver will take an unacceptable length of time to run. If the seeding is to low, the resonant trajectories will not be found. The seeding does not need to be too much as the resonant trajectories can start slightly off optimal position and will converge on to the optimal location over a few osculations.

Three different surface conditions of niobium have been used for simulation with different SEY:

- Wet treatment represents niobium that has been cleaned by high pressure water, this removes most particular surface contaminants.
- 300 deg bake-out is treated niobium that may have had a bake out to remove hydrogen and oxygen on the surface.
- The Ar discharge cleaned surface represents a cleaned niobium surface that has been processed. The nucleation sites for multipacting have been bombarded by ions and less likely to emit secondary electrons as the surface contaminants have been displaced. This is similar to an effect that multipacting itself can cause, where the surface is processed by secondary electrons, and can allow multipacting to be processed through by simply running the machine.

Multipacting can be identified as either hard or soft, depending on how its $< SEY >$ changes as the material is processed. For multipacting to be hard its $< SEY >$ will remain above one as its processed. However if, as processing takes place, the $< SEY >$ decreases below one the multipacting is said to be soft as it will die out. The initial surface of a cavity will have a high SEY. By cleaning, heating the surface or applying acid the surface SEY can be altered as contaminants are removed or added.

A full 3D eigen mode simulation was carried out with high mesh to establish the electromagnetic fields within the cavity using the basic vacuum cavity shape. A solid box is then draw around the cavity with the cavity shape removed from the structure. The remaining solid consists of the box of definable material with the vacuum shape of the cavity cut away internally.

6.4 Cavity Results

The cavity was simulated with three different surface emission models. First that of water-cleaned niobium, then with niobium treated with a 300 deg bake out (typical of many high gradient cavities), and finally that of Ar discharge cleaned cavity.

Each of the three different materials have a different peak average SEY coefficient for their emission models, these are shown in Table 6.1. Parameters taken from CST .

Model	Peak SEY	Peak SEY energy	SEY = 1
Wet treatment	2.80	230 eV	33eV
300 deg bake-out	1.49	300 eV	76eV
Ar discharge	1.25	342 eV	135eV

Table 6.1: Peak values for the emission models from $CST\, Particle\, studio$.

These different surfaces allow for the study of the effects of cleaning on the surface, as well as helping to understand if the multipacting will be soft or hard.

The results for wet-treated niobium are shown in Figure 6.4 and show how poorly cleaned niobium will readily multipact in the region of the iris in the expected manner.

The peak values for each phase were collected and plotted in Figure 6.7 for a simpler comparison.

The rapid increase in $< SEY >$ for wet treatment niobium can be attributed to the poorly cleaned surface. The rapid increase in $< SEY >$ leads to very long simulation runs, hence the study was stopped after a transverse voltage of 4.5 MV. The significantly lower $< SEY >$ for 300 deg bake-out shows the advantage that cleaning and simple processing can have on the cavity. This

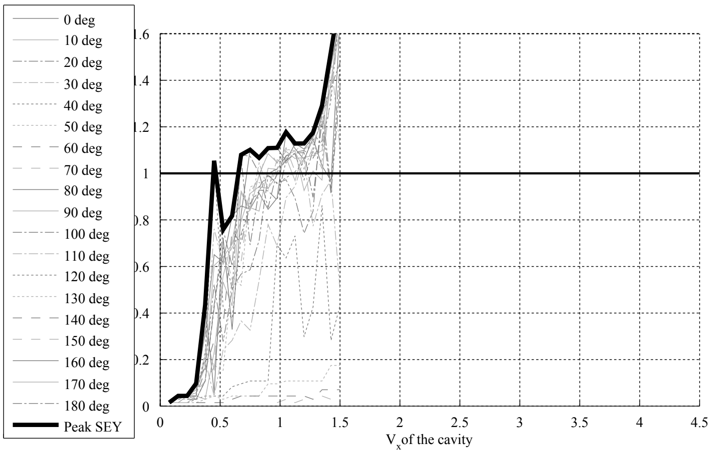

Figure 6.4: Average SEY for wet treatment niobium across all phases, up to a power level of 4.5 MV V transverse

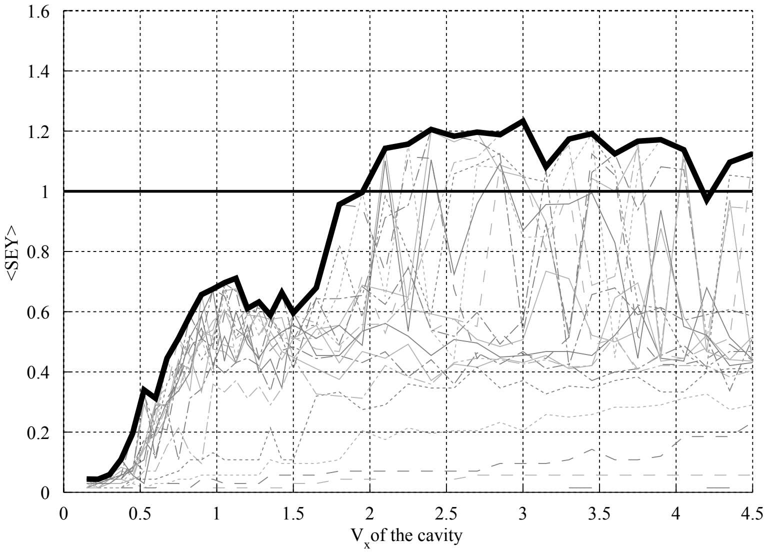

Figure 6.5: Average SEY for 300 deg bake-out niobium across all phases

has an $< SEY >$ that hovers around 1 after a transverse voltage of 1.9 MV is reached. No multipacting is seen for AR discharge cleaned, this suggests that the multipactor can be processed though and is thus 'soft'. The consistent values below 1 suggest that no hard multipacting will be seen in the cavity and although some soft multipacting may be seen around 2 MV $\mathbf{V}_t$ this should be processed though.

The LHC 4RCC appears to exhibit no hard multipacting in the region of operation, up to 4.5 MV, and some soft multipacting that simulations suggest can be processed through.

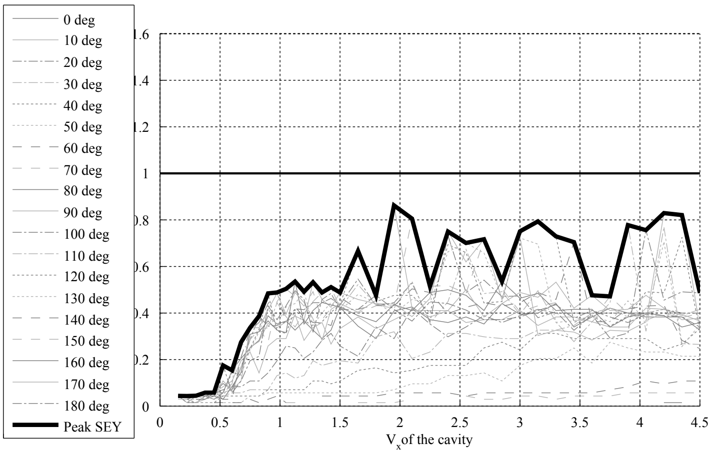

Figure 6.6: Average SEY for Ar discharge cleaned niobium across all phases

The multipacting was seen around the curvature of the iris region between the two rods. Figure 6.8 shows the initial location of the multipacting for the wet treatment. Figure 6.9 shows the same simulation some time later with the multipacting fully evolved and consisting of considerably more particles.

6.5 Conclusion

Multipacting is a serious issue for modern superconducting cavities that can result in cavity failures or designs not being commissioned. The design improvements made to elliptical cell cavities will not work for deflecting mode cavities as they have an alternative field configuration. Multipacting has been observed on the iris region and beam pipe of deflecting mode cavities in both numerical modelling and experimentation. This type of multipacting has shown to be a soft barrier that can be analytically predicted.

The 4RCC has been examined for multipacting in CST particle studio. Multipacting was predicted to appear at 22.44 mT surface field in the iris. Simulations showed that for an uncleaned surface multipacting happened almost immediately. For a surface that has undergone cleaning as a typical cavity would, multipacting was observed at $\sim$ 1.9 MV deflecting voltage on the beam pipe region, this corresponds to a surface field between $20 - 24$ mT. Simulating with

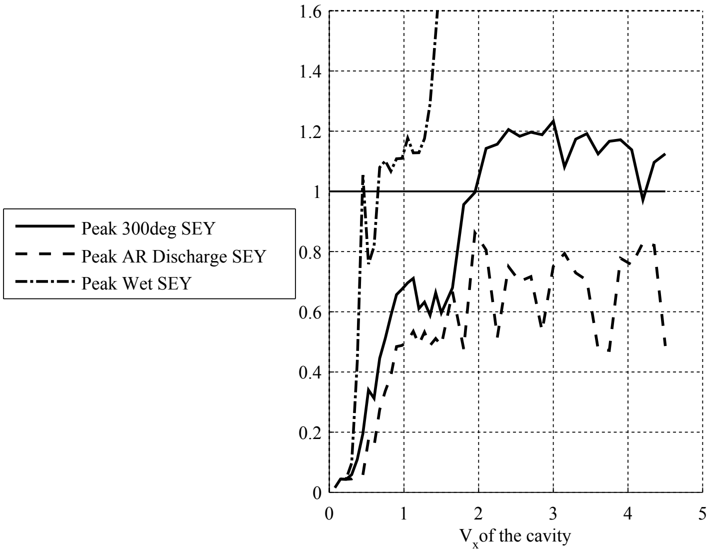

Figure 6.7: Average SEY for all models showing peak value across all phases at each power step.

a lower surface SEY, analogous to processing the cavity, the multipacting is no longer present. This matches the results of KEKB where the iris multipacting was processed though.

The electrons are accelerated by the electric field in this region. Figure 6.10 shows the electric field that oscillates and trajectory of the electrons in this region.

The four rod crab cavity shows some multipacting where expected on the beam pipe, however this appears to be soft and able to be processed through. Thus multipacting should not be a limiting factor for the four rod crab cavity.

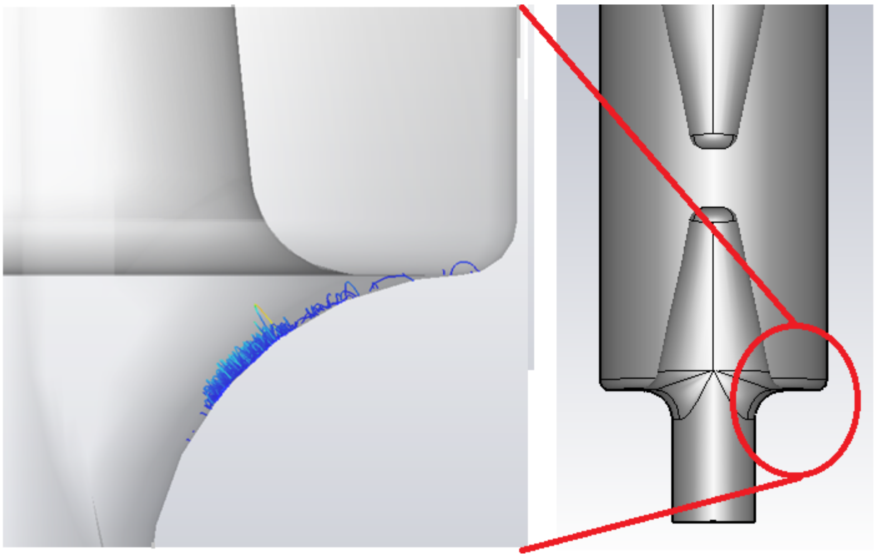

Figure 6.8: Initial multipacting region

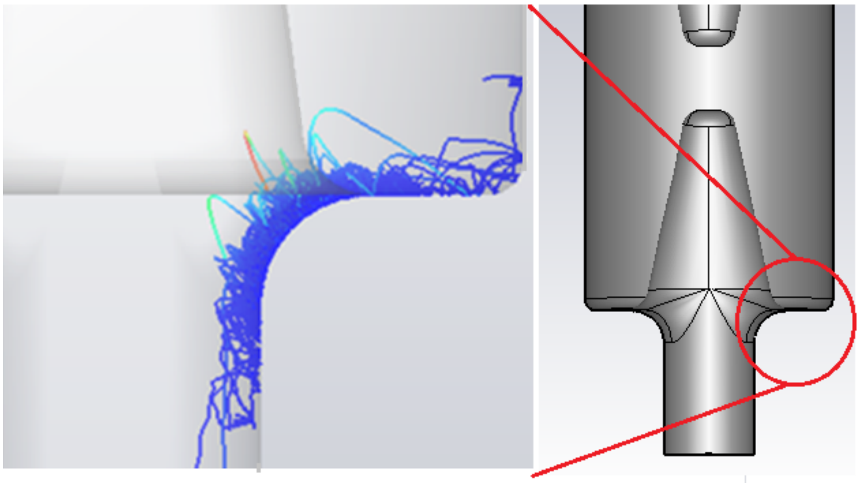

Figure 6.9: Multipacting on iris region some time later.

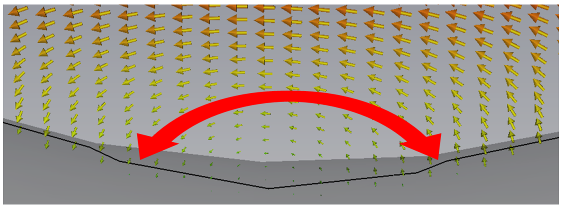

Figure 6.10: Electric field in the region of multipacting

Chapter 7

Design and manufacture issues.

7.1 Introduction

There are various potential methods of making superconducting cavities. Niobium will be used as it is the most versatile superconductor and used for nearly all superconducting cavities. The 4RCC can be split into 3 major pieces - the beam pipes, the outer can and the end plates with attached rods. These pieces need to be manufactured and assembled into the cavity.

The most common form of manufacture is to roll and press the desired shapes from flat sheet metal. This method is often preferred because while it has a high initial outlay for the construction of the dies, replicating the design only requires cavity material costs. However, this method can only produce shapes with positive draft. This is where the two profiles of the dies fit together and can be separated.

Another method to produce the desired shape is to machine the cavity from a solid block of material using a five-axis milling machine. In comparison to the pressing method described above, this method can produce more complicated designs with negative draft. However this method is considerably more expensive as a solid block of metal encompassing the entire shape must be used for each piece and each individual part requires extensive machining that is very expensive.

Any method of creating a cavity requires it to be made in separate sections that are then joined together. Once the pieces of the cavity have been formed they can then be welded together using an electron beam. This method is used as it allows the pieces to be joined in an inert atmosphere with minimal contamination to form a good vacuum seal [87].

For the 4RCC the beam pipes and outer can can easily be made by rolling sheet material to the correct shape. However the end plates and rods in their current form could not be made from dies.

As machining from bulk is very expensive a study was performed to see if slight alteration to the geometry would allow the cavity to be pressed.

7.2 Compound Round and Electron Beam Welding.

Splitting the end plate into multiple pieces requires them to be electron beam welded together. This will leave a weld seam and potential inhomogeneities in the weld area. Thus the weld location could become an issue. If the weld is too near the base of the rods, as would be preferable from the point of view of deep drawing, smaller pull outs are easier and less likely to go wrong. Then the weld would be located in a region of high magnetic field with high currents flowing across it. Any defects in the weld could then lead to heating and failure of the cavity at high power. However, if the weld is located further up the rod away from the high current area, the pull outs on the base plate would become unfeasibly long and defeat the purpose of having the welds in the first place.

An additional problem became apparent when examining the angle of weld for the second rod. Once the first rod is welded, the available space for the electron beam becomes limited, especially around the beam pipe. This results in an almost parallel weld which is highly problematic and is demonstrated in Figure 7.1.

An altered shape was proposed that allowed for welding from additional

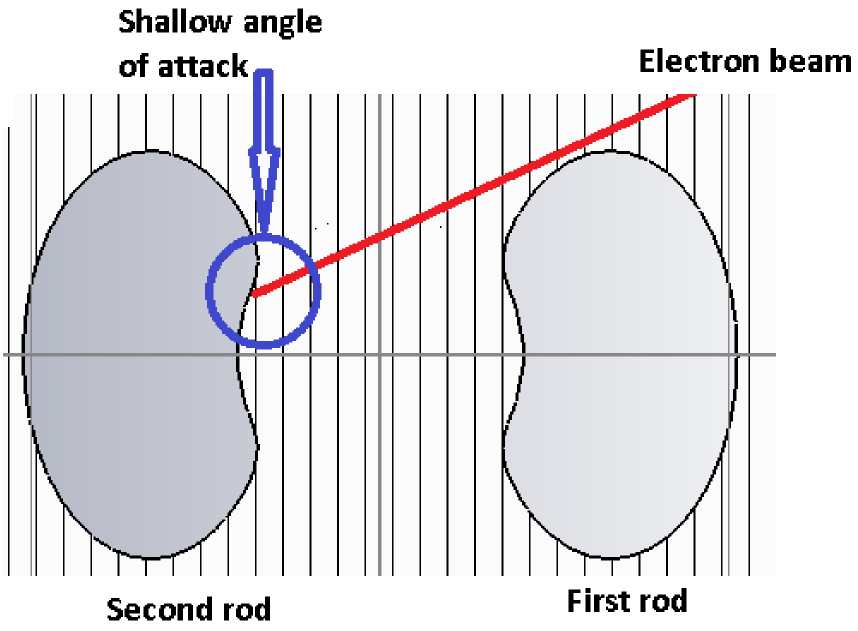

Figure 7.1: The shallow angle of attack that the second rod weld will experience after the first rod is welded in place.

directions, however the new pieces of niobium that would be needed to be created were even more complex. The surface fields were also unfavorable as the additional welding area at the base of the rod is in the area of peak magnetic field.

7.3 Deep Drawing and Compound Round

Deep drawing consists of forming the desired shape between two dies. Pressure is applied and the sheet material 'blank' is plastically deformed. Often this process can be carried out in several action to create more complex shapes. To create the base plate from a single sheet, the base plate would have to be deformed in most locations and several locations would require several deformations in more than one direction. By stacking the deformations, there is an increased risk the the niobium would tear rather than plasticity deform, thus ruining the part. The area that would experience the worst deformation would be the compound round at the base of the rods where they join the beam pipe.

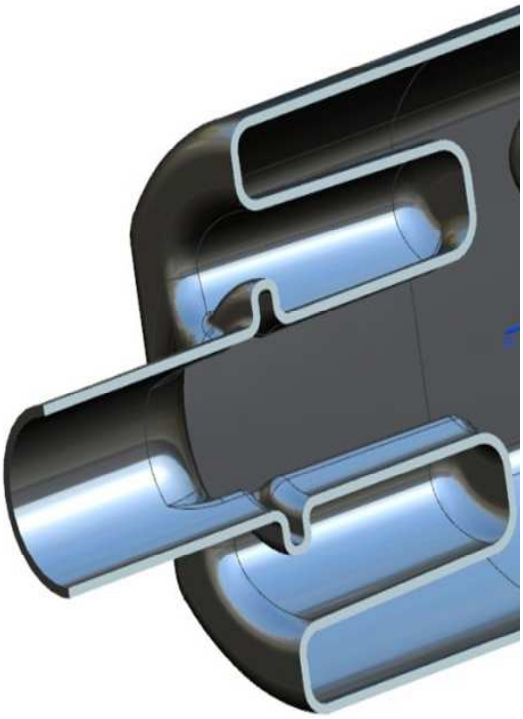

Figure 7.2: Altered shape proposed at the CC workshop

Through discussion with experts at JLAB the current shape was deemed difficult by deep drawing, thus other methods of construction were examined.

Design alterations were examined where the compound round was removed. To do this, the rods were moved apart and the rounding reduced so that they did not interfere with each other. Removing the kidney shape was also examined due to the additional deformation caused by the kidney shape. To regain some of the loss in transverse voltage the tips of the rods were angled in. Three different options are presented.

7.3.1 Kidney, No Compound Round

By moving the rods further apart, there was a slight decrease in the normalized transverse voltage, leading to higher surface fields. By decreasing the space available for the rod, the shape of the kidney becomes more elongated, resulting

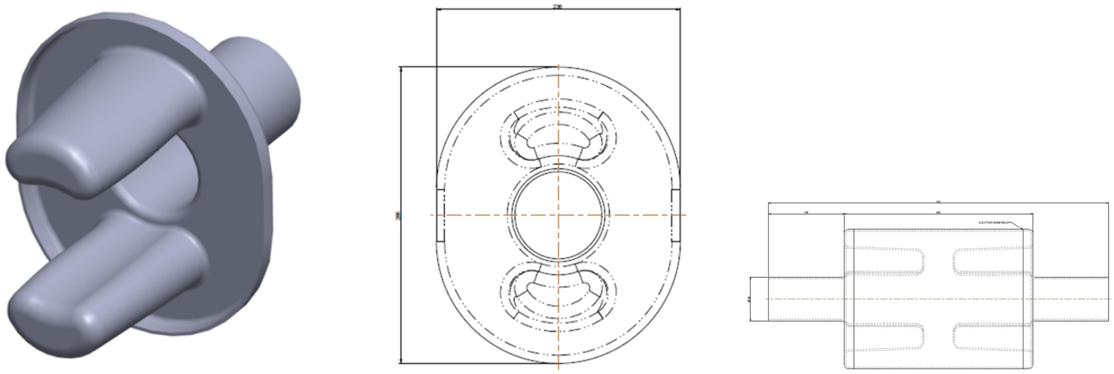

(a) (b) (c)

Figure 7.3: 3D picture of the altered shape a, end on schematic b and side on schematic c.

in tighter rounding. This sis shown in figure 7.3. As there is 103 mm between the edge of the beam pipe and the outer can, space is very limited. Approximately 25 mm is reserved for space between the outer can and the rod. This leaves $\sim$ 80 mm for the rod. The addition of rounding on both the base of the rod and the beam pipe to remove the double round reduced the space available for the rods by $\sim$ 10 %. The reduced rounding on the base of the rods increases the surface current density and correspondingly the peak surface magnetic field. The peak electric field is also increased by the reduced tip size.

7.3.2 No Kidney, No Compound Round

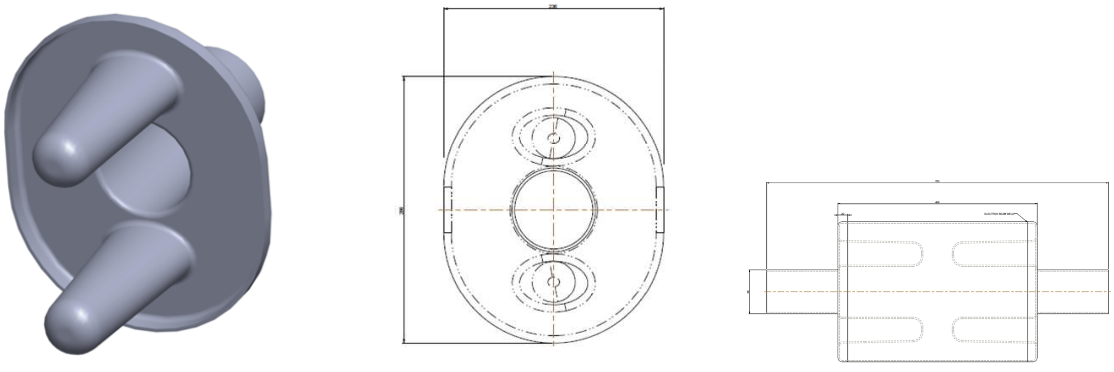

(a) (b) (c)

Figure 7.4: 3D picture of the altered shape a, end on schematic b and side on schematic c.

Similar to the kidney shape in Section 7.3.1, increasing the spacing between the rods reduces the normalized transverse voltage resulting in higher surface fields. The loss of the kidney shape reduces the surface to dissipate the surface current over even further, leading to an increased peak magnetic field. The shape is shown in figure 7.4. Without the kidney wings to shift the current path away from beam pipe, the rounding on the beam-pipe shares much of the peak magnetic field. The reduced tip size again leads to higher peak electric field.

7.3.3 Kidney, No Compound Round, Slanted Rods

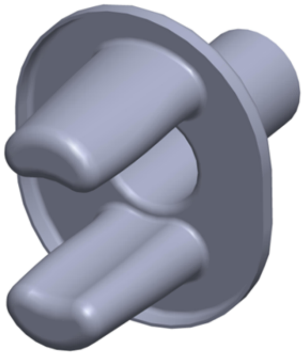

Figure 7.5: 3D picture of the altered shape with rods slanted towards each other.

By slanting the rods as shown in figure 7.5, some of the transverse voltage loss can mitigated, compared to the designs where the rods are perpendicular to the base plate but lack compound rounds. However, the reduced area for the base of the rods still results in higher peak magnetic field than the compound version.

7.4 Summary of Altered Shapes

The oval shape presents the worst surface fields - although it would be the easiest to manufacture, the surface fields are far too high.

The kidney-shaped rods offer better field profiles, but are still significantly worse than ideal. The shape should not prove particularly more difficult to manufacture than the oval rods.

Slanting the rods regains some of the lost transverse fields providing lower surface fields.

However, angled rods, which are the most feasible of the altered shapes, would require an extremely complicated deep drawing mechanism to avoid welds away from the high magnetic region at the base of the rods.

The decision was made after consultation with JLAB staff that had previous experience that to try and deep draw the cavity as one piece would be unfeasible.

Splitting the rods into additional pieces was considered. This would result in the base plate being manufactured separate from the rods and then electron beam welded together.

The decision to machine the structure from bulk niobium was made. The technology had been recently demonstrated with the on cell APS deflecting cavity. Although this increases the cost of each end plate in terms or niobium, instead of using dies that could be machined to the ideal shape. High precision can be attained though machining.

When deep drawing, the thickness of the cavity wall can sometimes vary in unforeseen and unsatisfactory ways. By machining the end plates of the cavity, the rods can be of uniform thickness along their length. If heating is an issue, the walls could be made thinner to help with heat transfer or support struts could be left in place to reduce microphonics or allow the tuning mechanism to spread force over the end in a more uniform way.

Thus the decisions was made to machine the end plates of the cavity from bulk large grain ingot niobium. This allowed for the complex geometry to be fully implemented.

7.5 Niobium Saving

During the mechanical design of the initial 4RCC prototype, it was noticed that a significant lump of niobium ingot was required for the base plates. As the base plates were to be machined from a solid block there will be significant wastage of material around the rods. This would add to the cost, as such an altered rod shape was proposed. The tips were narrowed to allow the rods to be rotated and intertwined in the gaps between each other. These blocks could them be cut apart to provide the two end plates with attached rods. This is shown in Figure 7.6.

The reduced tip size increases the peak electric field, however this was deemed acceptable for the prototype as it is not expected to undergo extensive high power testing. This shape was chosen to be built as a niobium cavity by Niowave. The prototype is shown in Figure 7.7, and was constructed with a 4 mm wall thickness. The cavity consisted of two end plates that supported the rods and were machined from bulk niobium, two beam-pipe sections from rolled sheet and an outer can again from sheet niobium. These were then electron beam welded together using niobium with an RRR > 200.

The cavity was tested by beadpull at Niowave with the operating mode at 400.032 MHz

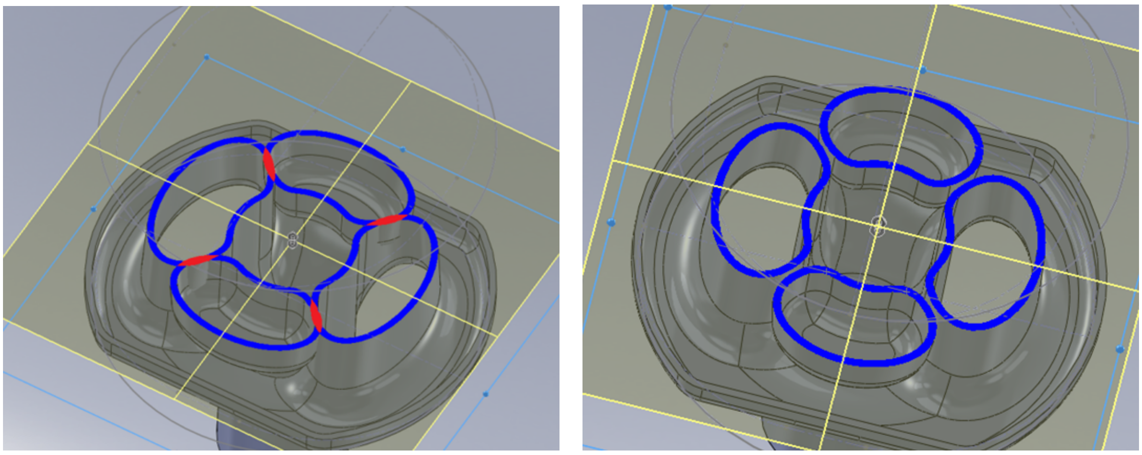

(a) The original shape with the tips overlapping with each other.

(b) The updated shape with narrower tips that saves on niobium usage and the financial cos, but increases the peak electric field.

(c) Interleaved rods of the cavity with gap between rods for cutting.

Figure 7.6: Altering the rod profile to allow niobium saving.

(a) Un-assembled niobium cavity

(b) E-beam welded niobium cavity

Figure 7.7: Pictures of the niobium cavity.

Chapter 8

Wakefields

In a traditional single cell elliptical accelerating cavity, the operating mode is the fundamental mode of the cavity, with all other modes being higher order modes, HOM's, with higher frequencies. For crab cavities we have the possibility of LOM's, SOM's and HOM's.

Within the four rod cavity there exist both a lower order mode (LOM) located at 375.18 MHz, and HOM's. The LOM is a by-product in nearly all normal deflecting cavities where the fundamental mode of the cavity is an accelerating mode. This mode is unwanted and must be damped so as not to interact with the beam as any beam power that is deposited in the cavity can cause beam instabilities. The HOM's similarly can result in unwanted disturbance to the beam profile and must be similarly damped.

All modes interact differently with the beam, the easiest way of comparing the interaction with the beam is to measure the R/Q of the mode. This is a direct relation to beam cavity interaction. The R/Q's of the modes up to 2.5 GHz are presented in Figure 8.1. The operating mode has a very high R/Q of 912.67 however, the LOM has a comparable R/Q of 124.34, which is similar to most accelerating cavities. This is due to the very compact nature of the cavity forcing all the fields and thus energy into the confined space of the beam pipe and thus beam. The first harmonics of the LOM and operating mode at 971.1 MHz and 1071.0 MHz respectively and are the $\frac{3\lambda}{4}$modes, also have sizeable R/Q's.

The TEM-like modes and their harmonics all follow the mode structure of wavelength given by the rod length l where $l = \frac{2n-1}{4}\lambda$ where n is the harmonic of the mode of the cavity. This results in the four configurations appearing in groups of increasing frequency.

The TE modes at lower frequencies treat the two inner conductors as a single entity and circulate around this inner conductor as if it was a coaxial system. This results in TE modes lower than a pillbox of the same size as they are only cut off at;

$$k_c = \frac{2}{a+b}$$

where a is the inner radius and b is the outer radius of the coaxial conductor. TM modes are pushed to higher frequencies near the beam-pipe cut-off as they are distorted by the rods.

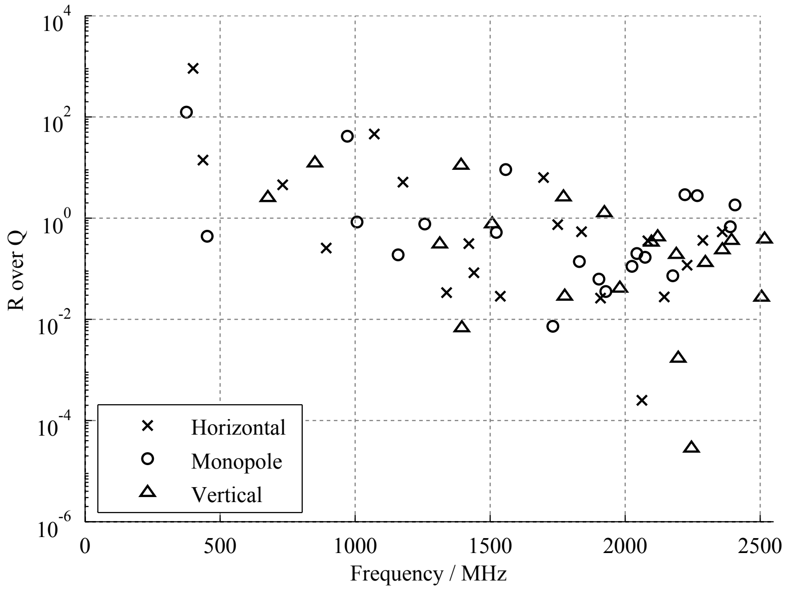

Figure 8.1: R/Q for modes within the cavity up to 2.5 GHz.

To ensure that the impedance of the cavity does not adversely effect the LHC a limit has been set on the extent to which a mode must be damped. A total impedance of 2.4 M ohms longitudinally and 1.5 M ohms/m transversely has been set [88]. To aid with tracking which modes are in need of significant damping the required Q of coupling has been calculated and is shown in Figure 8.2. The LOM is of particular note needing a Q of 1607, although a significant safety factor may be required. All other modes above the line of 10^4, highlighted, are in need of study and may require specific damping.

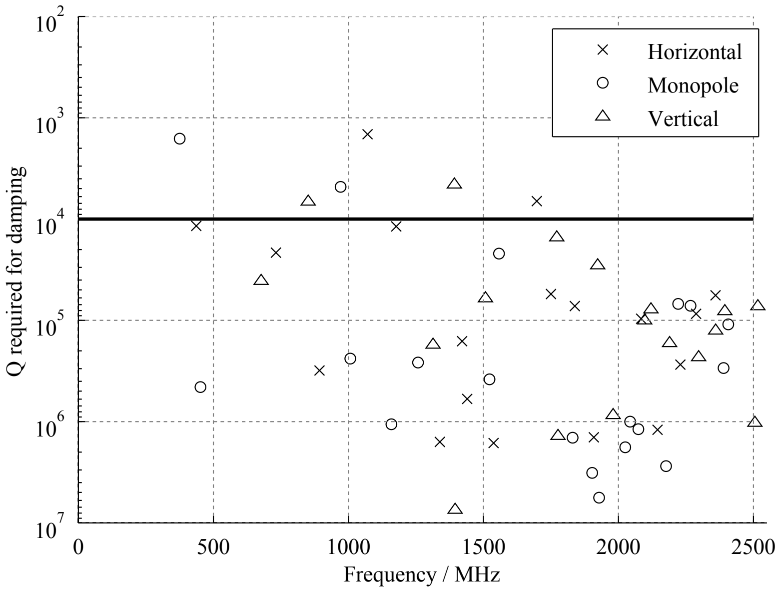

Figure 8.2: Q value required to sufficiently damp a mode.

8.1 Proposed LOM Coupler

To check the damping requirements of the LOM were achievable, a short study was carried out. Initial studies showed that a hook-like coupler would have to be inserted an infeasible way into the cavity. The decision to squash the cavity was made as this forced the magnetic fields, which the loop coupler is designed to intact with into a confined space. As the operating modes' magnetic field circles the rods, it is not perturbed significantly by this action.

Figure 8.3 shows how squashing the cavity causes a coupler with the same penetration to increase its coupling. Below 240 mm the squashing started to interfere with the peak field of the operating mode as the rods started to become to close to the outer can. Thus this value was set as a limit for the squashing, due to the exponential decay of the coupling this was deemed an acceptable trade off.

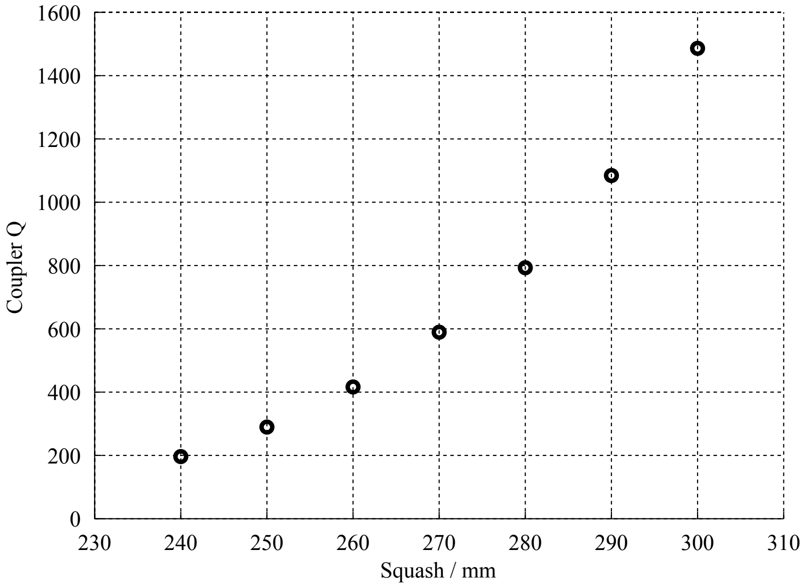

Figure 8.3: Coupler Q's for different cavity squashing.

The basic shape of the loop coupler is shown in Figure 8.4. Through further penetration of the coupler, a Q of ∼ 100 was achieved. This was deemed close enough to the impedance budget to be suitable for further development at a later date.

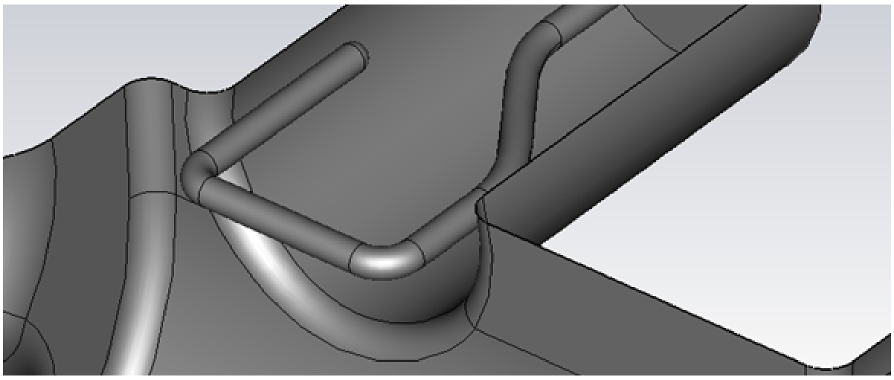

Figure 8.4: Initial idea for loop coupler.

8.2 Proposed Wave-Guide Coupler

An alternative coupler design consisting of ridged wave-guide was examined. Figure 8.5 shows the location of the wave-guide attached to the outer can of the cavity. Ridged wave-guide was used to reduce the profile compared to standard wave-guide. The coupling was achieved magnetically that geometrically excluded the operating mode. This is shown in Figure 8.6.

A $Q \sim 120$ was achieved with wave-guide coupling and this was deemed a viable option for future investigation.

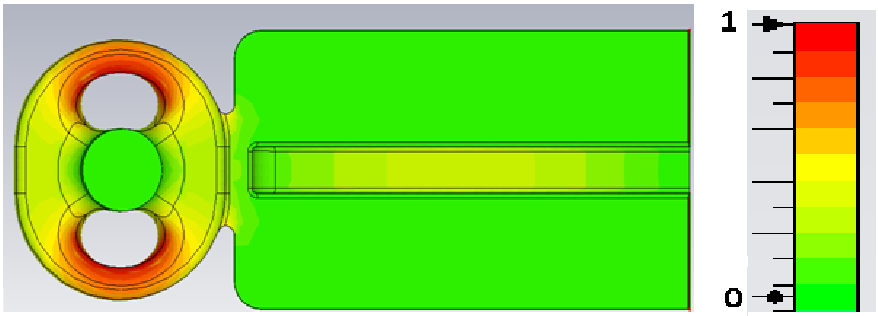

Figure 8.5: Magnetic surface fields with attached wave-guide, in arbitrary units.

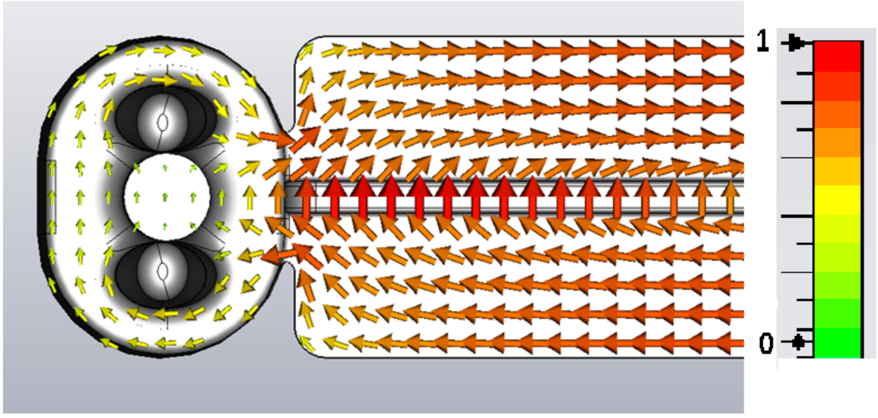

Figure 8.6: Magnetic fields of the LOM coupler, in arbitrary units.

8.3 Conclusion

The 4RCC has both a LOM and HOM's similar to an elliptical deflecting cavity, however it lacks a same order mode. The LOM is a monopole-like accelerating mode has a significantly high R/Q that required damping. A basic study showed that a simple hook-like coupler could achieve coupling with a low enough Q. The LOM coupler was positioned on the outer can such that it would geometrically exclude the operating mode.

Frequency	R/Q
375.2	124.4
400.0	912.7
436.6	14.0
452.1	0.4

Table 8.1: R/Q's for the first 4 modes of the cavity.

The wakefields pose no specific problem for the 4RCC as the main mode of interest can be strongly damped by a dedicated coupler that rejects the operating mode based on geometric orientation as well as any addition rejection designed into the coupler.

Chapter 9

Conclusion

For the LHC upgrade, a compact SRF crab cavity is required for the local upgrade scheme. This requires a novel shape as a standard eliptical vacity will not fit the space requiremnets.

A four rod design loosely based off of the CEBAF deflector was proposed and examined.

9.1 Design of Compact SRC Cavity

A compact crab cavity was optimized for low surface fields while fitting within the design space allowed for the LHC. This consisted of four $\frac{1}{4}\lambda$ resonators supporting a TEM wave. The LHC4R crab cavity in Chapter 4 fits all the current design specifications for the LHC, specifically that it fits within the limited space available - the cavity has a radius of 140 mm in the plane of the beam pipes.

The uniformity of deflecting voltage required by the LHC was not initially met by the original oval shaped rods. Alternative methods of flattening the deflecting voltage were examined and a new shape was created. Parallel plates would provide a uniform mode, however they resulted in an unacceptable drop in R/Q and increased the size of the cavity beyond the limits that would allow the cavity to be rotated to enable vertical crossing. Focus electrodes were used to replicate the longer plate-like rods without compromising on the compact nature of the cavity. The electrodes allowed for the minimisation of multipole components that can adversely effect the dipole field. A variation in the dipole field of less than 0.1 % at 15 mm was achieved.

The focus electrodes do not line up well with the geometry of the beam-pipe and a new shape was created that followed the contour of the beam-pipe. The kidney shape provided all the advantages of the focus electrodes whilst following the same optimisation pattens as the oval shape.

The new cavity shape was designed with peak surface fields of 60.5 mT and 32.0 MV at a deflecting voltage of 3 MV. This was made into an Aluminium test piece for further testing.

If the higher order components are non-zero, they can be offset against each other to minimize their effects at low offset. If a flatter field is required or specific higher order components require minimization, the rod faces can be altered to accommodate this.

The Aluminium cavity that was produced for experimentation provided measurements which confirmed the basic properties of the cavity and allowed for the fields within the cavity to be tested via bead-pull. Although significant noise was initially seen, through processing and adjustment taking on axis errors into count, useful measurements were able to be taken and compared to simulations from CST.

The cavity showed close agreement with the simulations despite errors calculated. The field uniformity lies within the error of the measurement and as such is assumed to be within tolerance as no major deviation was seen.

The fields of the cavity match well with the expected fields as calculated from CST for both the operating mode and the lower order mode. The good correlation with the expected results through bead pull implies the cavity is operating as designed.

Multipacting is a serious issue for modern superconducting cavities and can result in cavity failures or designs not being commissioned. The design improvements made to elliptical cell cavities will not work for deflecting mode cavities as they have an alternative field configuration.

The four rod crab cavity has been examined for multipacting in CST particle studio. Multipacting was predicted to appear at 22.44 mT surface field. Simulations showed that for an uncleaned surface multipacting happened almost immediately. For a surface that has undergone cleaning as a typical cavity would, multipacting was observed at $\sim 1.9\,\mathrm{MV}$ deflecting voltage on the beampipe region, this corresponds to a surface field between $20 - 24\,\mathrm{mT}$. Simulating with a lower surface SEY, analogous to processing the cavity, the multipacting is no longer present. This matches the results of KEKB where the iris multipacting was processed through.

The four rod crab cavity shows some multipacting where expected on the beam pipe however this appears to be soft and able to be processed through. Thus multipacting should not be a limiting factor for the four rod crab cavity.

Due to the high cost of niobium, a modified design was produced by Niowave to enable high power tests in a cryostat. This design altered the tips of the rods such that the two base plates could be made of a single piece of niobium. This results in higher peak electric fields, but a considerable saving in costs.

9.2 Comparison to Other Cavities

Other options are currently being developed for the LHC. The two main contenders are a quarter wave resonator design and a wave-guide like structure. A comparison of the main features on the cavities and the design presented here are shown in Table 9.1.

	Quarter Wave	Wave-guide	LHC4RCC
$R/Q(\Omega)$	345	323	915
E_{peak}(MV/m)	43	36	32.0
B_{peak}(mT)	61	55	60.5
V_z(MV)	0.12	0	0
$Z_{Dimention}$(mm)	$\sim$ 405	$\sim$ 620	500.7
$X_{Dimention}$(mm)	254.2	295	280
$Y_{Dimention}$(mm)	285	295	220
$V_{\perp}/m$ (MV/m)	7.41	4.84	5.99

Table 9.1: Comparison of main features of proposed compact cavities.

9.2.1 Quarter Wave Resonator

The quarter wave resonator is shown in Figure 9.1. This design is very compact but suffers from an asymmetrical design. This leads to an accelerating voltage that is not seen in in the other designs as well as significant quadrapole terms that are also not present in the other designs. The peak fields are the highest out of the proposed designs. Due to the simple nature of the cavity it is the easiest to make, although the cavities are not needed in large numbers.

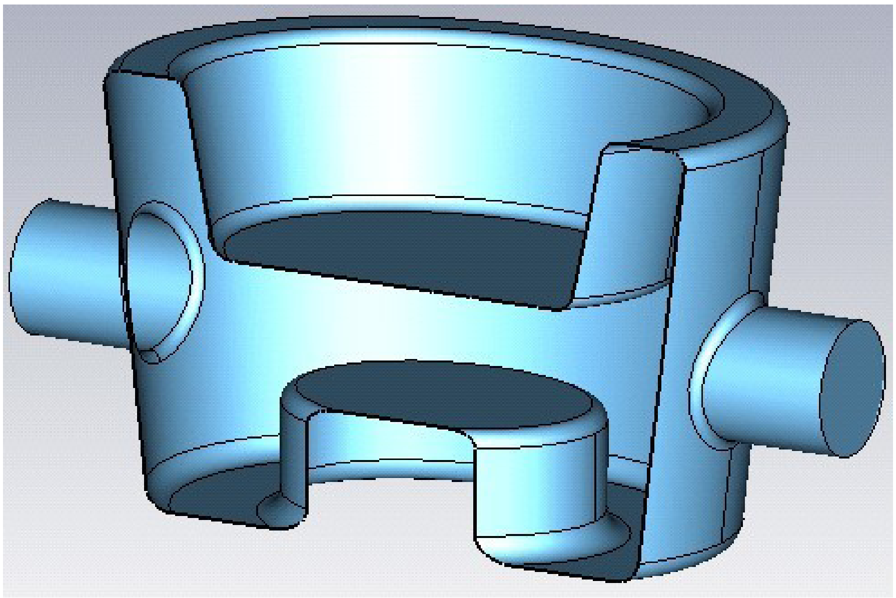

Figure 9.1: Proposed quarter wave resonator shape[89].

The R/Q spectrum is shown in Figure 9.2. The cavity has a good separation between the operating mode and the first HOM but has 10 modes above an R/Q of 10.

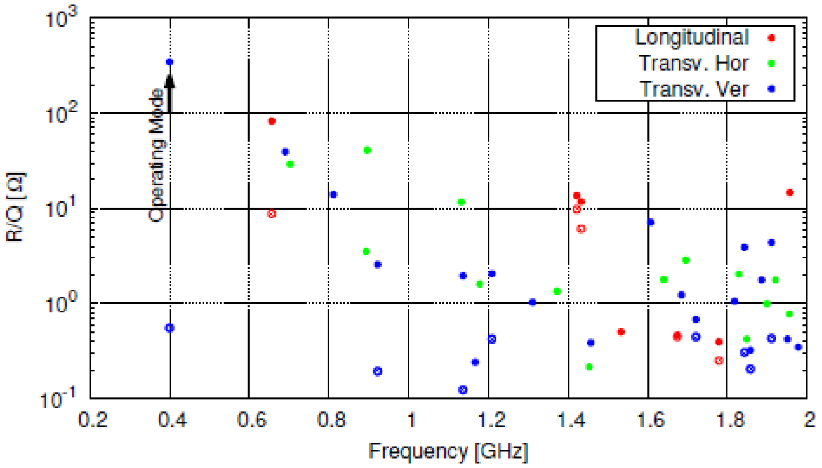

Figure 9.2: HOM profile of the quarter wave cavity[89].

9.2.2 Ridged Wave-Guide

The wave-guide resonator is shown in Figure 9.3. This design is the largest of the designs and current, only a gap of 4.5 mm exists vacuum to vacuum between the cavity and the opposing beam line. As the expected wall thickness of the cavities will be $\sim$ 4 mm and the opposing beam line needs a structure this will need further modification to fit.

The cavity is considerably longer than either of the other designs, by $\sim$ 60 %, which could become an issue if longitudinal space requirements become a factor in design considerations. As the couplers for this design are envisaged to be on the base plate, the cavity will retain its transverse compact nature. However, this will be at the expense of longitudinal space as this cavity has significantly lower transverse gradient. As up to six cavities may be needed on each side of the IP to provide the full 10 MV, this may be a consideration.

The structure has the lowest peak magnetic field at the cost of a slightly higher electric field. Though, as with the design of the four rod design, this has proven to be able to be exchanged for better electric field performance.

The HOM spectrum is shown in Figure 9.4. The cavity has a good separation between the operating mode and the first HOM and no LOM. However, this design has the highest number of HOM's above an R/Q of 10 at 13 modes.

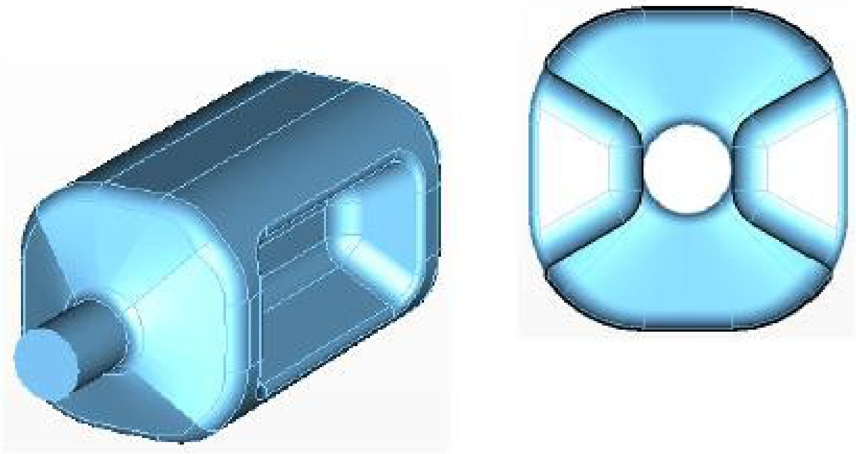

Figure 9.3: Proposed wave-guide resonator shape[90].

There is a HOM at $\sim$ 950 MHz that has an R/Q similar to the operating mode and will need to be strongly damped.

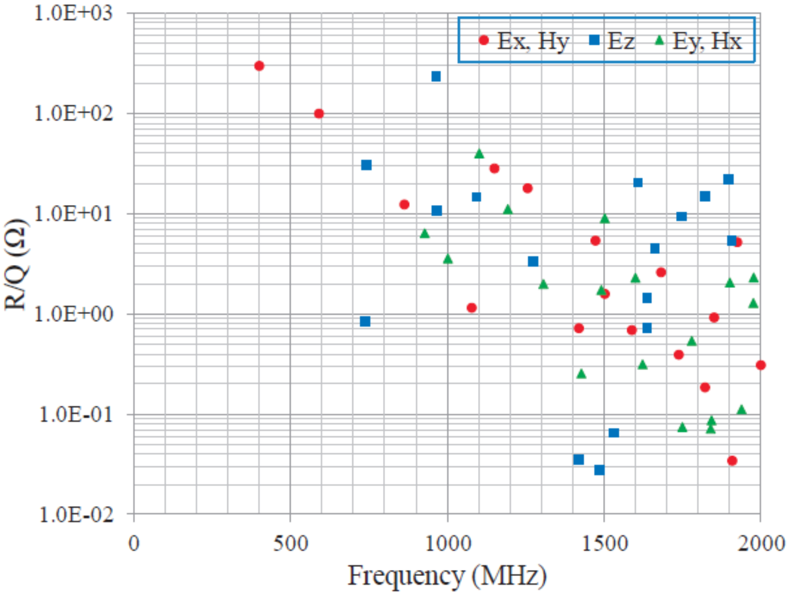

Figure 9.4: HOM profile of the ridged waveguide[90].

The exact manufacturing technique to be used has not been finalized, but all test versions so far have had a combination of stamped, rolled and machined parts. The final design is expected to be stamped as the ridges are altered in shape though the feasibility of this has yet to be demonstrated.

9.2.3 Four Rod Structure

The four rod structure is shown in Figure 9.5. This design is limited by the rods in the direction of deflection, but is highly compact in the alternate direction. The peak electric field is the lowest of the proposed designs with the second best peak magnetic field. The ratio between the peak electric and magnetic field can be altered slightly to lower the peak magnetic field at the cost of peak electric field.

This design has a much higher R/Q compared to the other designs, however if a lower value is required this can be reduced by altering the rod shape. The high R/Q allows for the cavity to have a high deflecting voltage relative to the stored energy of the cavity. However, this doesn't cause the LOM and HOM to have high R/Q's.

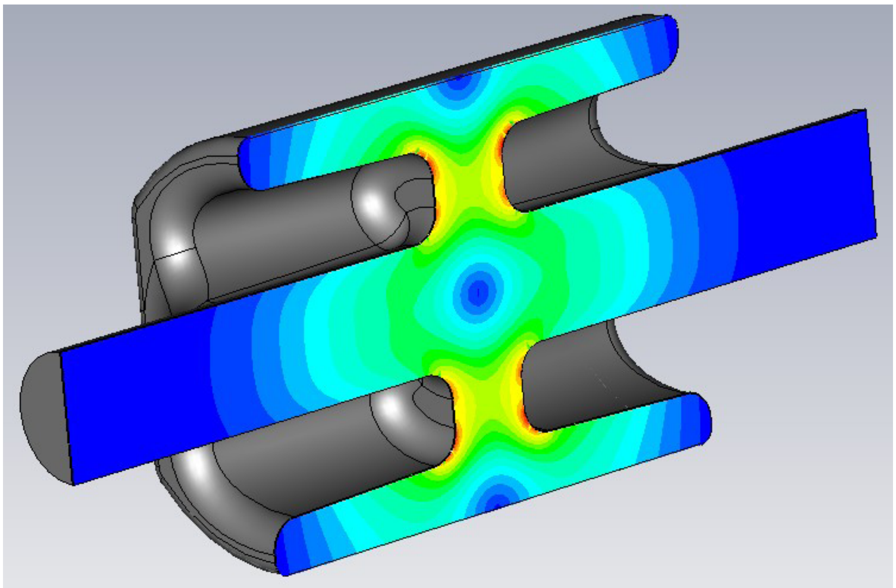

Figure 9.5: Proposed four rod resonator shape.

The higher order mode spectrum of the 4RCC is shown in Figure 9.6. The cavity has a LOM that is both significantly high and close to the operating mode. However, due to the location of the magnetic fields for this mode it is believed that it can be strongly damped while geometrically avoiding the operating mode. There are two HOM's close to the operating mode that have reasonably low R/Q's. There are a total of six modes with an R/Q above 10 .The

4RCC has the least populated HOM spectrum of the proposed designs which could prove advantageous if impedance budgets become critical.

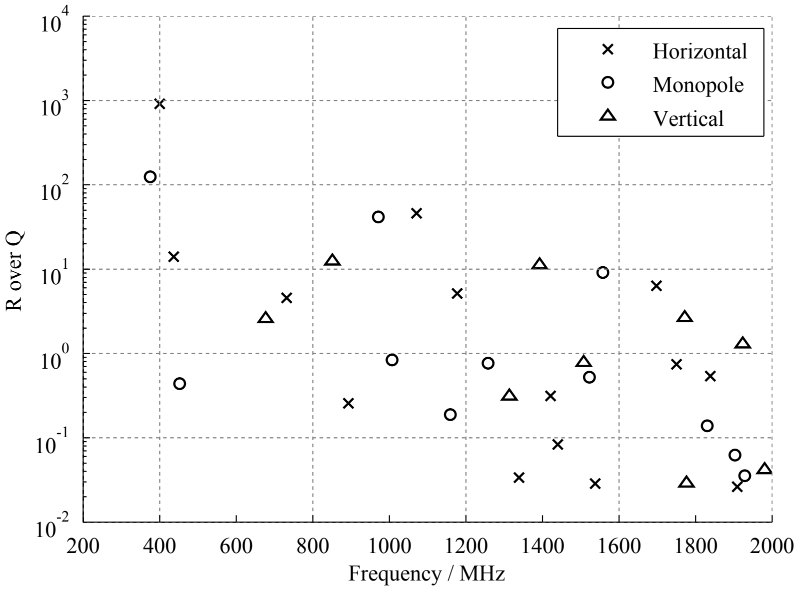

Figure 9.6: HOM profile of the 4RCC.

The necessity to machine the base plates of the cavity result in a relatively complex structure to manufacture. However as nearly all the geometry is located on the base plates assuming that they can be machined by a 5-axis milling machine, the cavity is no more complicated than the ridged waveguide.

9.2.4 Summary of LHC Upgrade Options

Of the three options currently available for the LHC upgrade, the quarter wave resonator is the poorest contender. Its asymmetrical shape and poor field performance result in the other two designs being more susceptible in the current design environment. The wave-guide like resonator and the four rod shape are both equal contenders in the design. Both have very low surface fields and no longitudinal component. The wave guide like structure does need some modification to fit within the design envelope currently as there is not enough room for the opposing beam line. Though this will likely be remedied in the next design update.

9.3 Future Work

The structure constructed throughout this thesis is only the initial RF design. Considerable further work is needed for the structure to become a completed unit able to be fully integrated within the LHC.

9.3.1 Elimination of Sextupole Components

The current design provides a flat deflecting voltage across the centre of the aperture. However there are still some sextupole components that offset against the decapole components. If the decapole components are viable at larger values then the design could be altered to completely remove the sextupole component at the expense of slightly higher multi-pole components of higher orders. This design change may be preferential, though consultation with CERN is required.

9.3.2 Vertical Testing of Structure

The niobium prototype produced by Niowave has been designed to be cold tested. This will allow high power tests of the cavity shape to ensure the cavity can operate at the design gradient. Some soft multipacting was predicted around the iris region, and the discovery and processing through of this would confirm the simulations. The choice to machine the cavity from a single block of niobium and still be able to achieve the required gradient rather than the standard pressed shape would be good to confirm.

9.3.3 Couplers

The initial vertical tests of the cavity will require couplers to be designed and manufactured. These must fit within the ports added to the Niowave shape. The cavity will require at least one import coupler, one LOM coupler and one HOM coupler. Additional couplers may be required or may be integrated with the aforementioned couplers. These need complete RF designs, thermal studies and to be checked for multipacting.

9.3.4 Thermal and Mechanical Considerations

The cavity structure needs to be analysed for both mechanical and thermal properties. The RF fields within the cavity will generate some heating, either via impurities or general thermal instabilities. If the cavity cannot dissipate this heat into the helium bath, a quench could happen. Unfortunately the thermal conductivity of niobium is less than ideal, thus thin walls are desirable. However, the cavity will be under vacuum relative to pressures potentially up to 2 Bar at times, for example during cool down. To ensure the cavity does not plastically deform and become buckled during these pressure changes, the mechanical stability must be investigated and the shape potentially altered to stop this. As the rods are being machined out of bulk, the insides of the cones can have material left in strategic places to act as stiffening ribs. However, the outer can which currently contains a large flat area will not be able to do this and may require a new shape or stiffening ribs. Any stiffening ribs added must avoid the opposing beam line which may add further complications.

9.3.5 Tuning

The frequency of the cavities may shift during cool down as the niobium contracts or the cavity may need to be shifted off resonance, during the ramp for example, so that it does not interact with the beam. To enable the cavity frequency to be altered, either to shift the cavity back onto, or away from, resonance, a method of tuning the cavity in situ. The current envisioned tuning setup would consist of squashing the cavity in the longitudinal direction as this alters the capacitance at the ends of the rods and thus the frequency of the cavity.

This would require a calliper arrangement that could apply force to the end plates of the cavity and elastically squash it. As the outer can is effectively a cylinder shape that is mechanically very strong in compression, some modification may be required. Adding in a deformable ridge on the outer can in an area where there are no fields would be the first area of study.

9.3.6 LOM and HOM Frequencies

The current design of the cavity has a LOM with a high R/Q and two close by HOM's. Ideally, there would be no LOM in the cavity and all of the HOM's would be at considerable higher frequencies as this would allow for simpler coupler designs and low wakefields. During the design of the current cavity, little attention was paid to the HOM's and the LOM was only studied in regard to achieving good coupling to remove it. By altering the outer can shape or the rod profiles it may be possible to shift the frequencies of the other modes to more desirable locations.

9.3.7 Test in SPS

The Niowave cavity could be placed in the SPS at CERN to test the cavity with a high current beam. This would allow further conformation of the cavity's viability to act as the crab cavity for the HL-LHC project. A test in the SPS will also allow the effects of emmittance growth to the studied.

The SPS will allow the crab cavity to be tested with beam as the LHC cannot be used as a trial run and conformation of the crab cavity is essential before tests in the LHC are carried out.

9.3.8 Cryomodule

The crab cavity will be operating at superconducting temperatures and will need an associated cryomodule to fit it into the existing cryo system in place at CERN. This module must contain the helium jacket to maintain the helium bath around the cavity, gas return for any boiled off helium and input for fresh helium. This must all be contained within any vacuum vessels, magnetic shielding and intermediate liquid nitrogen cooling. Input and damping couplers along side tuners and any electronic monitors must also be included and will penetrate though several of these layers. As it is unknown if two or three cavities will be used in the final design, the cryomodule design must be adaptable to the ever-changing requirements of the LHC.

9.3.9 Low Level RF

The cavities require very strict timing between the kicks they give to a bunch as it travels around the ring. The crabbing cavities must all have the correct phase such that the full 10 MV of defecting voltage is delivered to the beam as required. The anti-crab cavities must similarly have the correct phasing to ensure all the rotation is removed. This requires a dedicated control system to maintain the crab cavities at their correct phase and power.

9.4 Other Applications

As well as the crab cavity for the LHC upgrade, there are other projects that require compact deflecting cavities that a modified 4RCC could be used for.

The CEBAF experiment is undergoing an upgrade to 12 GeV and is in need of new deflectors to the current normal conducting ones. The 4RCC is based directly off of this design and only relatively small modifications would be required to alter the design to replace its spiritual forefather[90].

In addition to the 12 GeV upgrade, an electron-light ion collider (ELIC) that would utilise crab cavities is also being built at JLab. Although, this design calls for a 1.5 GHz crab cavity[91].

The Project X deflector has similar requirements to the LHC crab system, though it needs more transverse kick. The project calls for 10 MV of kick from one cavity operating at approximately 400 MHz. A similarly large aperture is required. The 4RCC could be modified slightly to provide the requested performance [92].

All three projects are close to the design requirements of the LHC that the 4RCC could be modified to fulfil the needs of each.

Bibliography

[1] L.R. Evans. *The Large Hadron Collider: A Marvel of Technology*. Fundamental sciences. EPFL Press, 2009. ISBN 9782940222346. URL `http://books.google.co.uk/books?id=tl8fLB1viQcC`.

[2] Max Klein. The large hadron electron collider project. *Prog. High Energy Phys.*, 3(arXiv:0908.2877):236, Aug 2009. Comments: DIS09 Conference Contribution.

[3] F Bertinelli, N Catalan Lasheras, P Fessia, C Garion, S Mathot, A Perin, C Scheuerlein, S Sgobba, H ten Kat, J P Tock, A Verweij, and G Willering. Towards a consolidation of lhc superconducting splices for 7 tev operation. (CERN-ATS-2010-144):4 p, Jun 2010.

[4] D. Boussard, E. Chiaveri, E. Haebel, H. P. Kindermann, R. Losito, S. Marque, V. Rodel, and M. Stirbet. The lhc superconducting cavities. In *Proceedings of the 1999 IEEE Particle Accelerator Conference. 29 Mar - 2 Apr 1999, New York, New York. 18th IEEE Particle Accelerator Conference, p.946-948*, pages 946–948, New York, 1999. IEEE.

[5] Georges Aad et al. Observation of a new particle in the search for the standard model higgs boson with the atlas detector at the lhc. *Physics Letters B*, 2012.

[6] S Khalil. Search for supersymmetry at lhc. *CONTEMPORARY PHYSICS*, 44(3):193–201, MAY-JUN 2003. ISSN 0010-7514. doi: 10.1080/0010751031000077378.

[7] Nima Arkani-Hamed and Neal Weiner. Lhc signals for a superunified theory of dark matter. *Journal of High Energy Physics*, 2008(12):104, 2008. URL `http://stacks.iop.org/1126-6708/2008/i=12/a=104`.

[8] Savas Dimopoulos and Roberto Emparan. String balls at the lhc and beyond. *Physics Letters B*, 526:393–398, 2002. URL `http://www.sciencedirect.com/science/article/pii/S0370269301015258`.

[9] Eberhard Keil. The large hadron collider lhc. oai:cds.cern.ch:316527. *Snowmass 96*, (LHC-Project-Report-79. CERN-LHC-Project-Report-79):5 p, Oct 1996. revised version submitted on 2004-08-19 11:10:07.

[10] R Garoby, S Gilardoni, B Goddard, K Hanke, M Meddahi, and M Vretenar. Plans for the upgrade of the lhc injectors. oai:cds.cern.ch:1382976. In *Proceedings of IPAC2011, San Sebastian, Spain*, number CERN-ATS-2011-185, page 3 p, Sep 2011.

[11] Lutz HEIN and Alessandra LOMBARDI. Update of the linac4-psb transfer line. Technical Report sLHC-Project-Note-0028. CERN-sLHC-Project-Note-0028, CERN, Geneva, Dec 2010.

[12] O S Bruning, F Zimmermann, and M Klein. The lhec project development beyond 2012. oai:cds.cern.ch:1470607. Technical Report CERN-ATS-2012-230, CERN, Geneva, May 2012.

[13] O Dominguez and F Zimmermann. Luminosity optimization for a higher-energy lhc. oai:cds.cern.ch:1382045. (EuCARD-CON-2011-052):3 p, Sep 2011.

[14] Frank Zimmermann. Hl-lhc: Parameter space, constraints, and possible options. oai:cds.cern.ch:1346545. *EUCARD contributions*, (EuCARD-CON-2011-002):317–330, 2011.

[15] Lucio Rossi. The fp7-hilumi design study and hl-lhc project. 1st hilumi lhc / larp collaboration meeting, Nov 2011.

[16] O Bruning. Do we really need the lhc luminosity upgrade?. do we really need the lhc luminosity upgrade? or, which performance can we get without an upgrade? In *Proceedings of Chamonix 2011 workshop on LHC Performance*, pages 291–301, 2011.

[17] Frank Zimmermann. Lhc: The machine. In *SLAC Summer Institute 2012*, 26 July 2012. URL `http://www-conf.slac.stanford.edu/ssi/2012/Presentations/Zimmermann.pdf`.

[18] Ulrich Zimmermann, Frank ; Dorna. Progress of beam-beam compensation schemes. *2nd CARE-HHH-APD Workshop on Scenarios for the LHC Luminosity Upgrade, Arcidosso, Italy,*, pages pp.55–73, 31 Aug - 3 Sep 2005. URL `http://cdsweb.cern.ch/record/978341/files/p55.pdf`.

[19] Q. Xu, T. Nakamoto, T. Ogitsu, K. Sasaki, A. Terashima, K. Tsuchiya, A. Yamamoto, E. Todesco, A. Kikuchi, and T. Takeuchi. Conceptual design of a large-aperture dipole magnet for hl-lhc upgrade. *Applied Superconductivity, IEEE Transactions on*, 22(3):4901404, june 2012. ISSN 1051-8223. doi: 10.1109/TASC.2011.2180293.

[20] R de Maria. Layout design for final focus systems and applications for the lhc interaction region upgrade. oai:cds.cern.ch:1064704. Technical Report LHC-PROJECT-Report-1051. CERN-LHC-PROJECT-Report-1051, CERN, 2007. revised version submitted on 2007-12-13 16:58:30.

[21] G. Dissertori, D. Luckey, F. Nessi-Tedaldi, F. Pauss, R. Wallny, et al. A visualization of the damage in lead tungstate calorimeter crystals after exposure to high-energy hadrons. *Nucl.Instrum.Meth.*, A684:57–62, 2012.

[22] Tatiana Libera Rijoff, Ralph Steinhagen, and Frank Zimmermann. Simulation studies for lhc long-range beam-beam compensators. oai:cds.cern.ch:1450938. *3rd International Particle Accelerator Conference 2012*, (CERN-ATS-2012-074):3 p, May 2012.

[23] K Hara and Y Ikegami. Silicon strip detectors for atlas at the hl-lhc upgrade. *2nd International Conference on Technology and Instrumentation in Particle Physics*, Aug 2012.

[24] F G Oakham. Atlas upgrade for the hl-lhc. Presentation, Jan 2012.

[25] Mercedes Minano and S. Marti. *Irradiated Silicon Detectors for HL-LHC: Characterization and Simulations. oai:cds.cern.ch:1470353*. PhD thesis, Valencia U., 2012. Presented 18 Jul 2012.

[26] J.-P. Koutchouk G. Sterbini. A luminosity leveling method for lhc using an early separation scheme. April 2, 2007. URL `http://cern-ab-bblr.web.cern.ch/cern-ab-bblr/Meetings/leveling.pdf`.

[27] T. Pieloni. Leveling scenarios: present and future prospectives. 2nd Joint HiLumi LHC-LARP Annual Meeting, 14-16 November 2012.

[28] R De Maria and S D Fartoukh. A proposal for the optics and layout of the hl-lhc with crab cavities. oai:cds.cern.ch:1381534. (CERN-ATS-2011-107):3 p, Sep 2011.

[29] R. B. Palmer. Simulation studies for the lhc long-range beam-beam compensators. *SLAC-PUB-4707*, 1988. URL `http://www.slac.stanford.edu/cgi-wrap/getdoc/slac-pub-4707.pdf`.

[30] T. Abe, T. Agho, K. Akai, M. Akemoto, A. Akiyama, M. Arinaga, K. Ebihara, K. Egawa, A. Enomoto, J. Flanagan, S. Fukuda, H. Fukuma, Y. Funakoshi, K. Furukawa, T. Funiya, K. Hara, T. Higo, S. Hiramatsu, H. Hisamatsu, H. Honma, T. Honma, K. Hosoyama, T. Ieiri, N. Iida, H. Ikeda, M. Ikeda, S. Inagaki, S. Isagawa, H. Ishii, A. Kabe, E. Kadokura, T. Kageyama, K. Kakihara, E. Kako, S. Kamada, T. Kamitani, K. Kanazawa, H. Katagiri, S. Kato, T. Kawamoto, S. Kazakov, M. Kikuchi, E. Kikutani, K. Kitagawa, H. Koiso, Y. Kojima, I. Komada, T. Kubo, K. Kudo, N. Kudo, K. Marutsuka, M. Masuzawa, S. Matsumoto, T. Matsumoto, S. Michizono,

K. Mikawa, T. Mimashi, S. Mitsunobu, K. Mori, A. Morita, Y. Morita, H. Nakai, H. Nakajima, T.T. Nakamura, H. Nakanishi, K. Nakanishi, K. Nakao, S. Ninomiya, Y. Ogawa, K. Ohmi, S. Ohsawa, Y. Ohsawa, Y. Ohnishi, N. Ohuchi, K. Oide, M. Ono, T. Ozaki, K. Saito, H. Sakai, Y. Sakamoto, M. Sato, M. Satoh, K. Shibata, T. Shidara, M. Shirai, A. Shirakawa, T. Sueno, M. Suetake, Y. Suetsugu, R. Sugahara, T. Sugimura, T. Suwada, O. Tajima, S. Takano, S. Takasaki, T. Takenaka, Y. Takeuchi, M. Tawada, M. Tejima, M. Tobiyama, N. Tokuda, S. Uehara, S. Uno, Y. Yamamoto, Y. Yano, K. Yokoyama, M. Yoshida, S. Yoshimoto, K. Yoshino, E. Perevedentsev, and D.N. Shatilov. Beam operation with crab cavities at kekb. In *Particle Accelerator Conference, 2007. PAC. IEEE*, pages 1487 –1489, june 2007.

[31] K Hosoyama, K Akai, K Ebihara, T Furuya, H Hara, K Hara, T Honma, A Kabe, Y Kojima, S Mitsunobu, Y Morita, H Nakai, K Nakanishi, K Okubo, M Ono, K Sennyu, Y Yamamoto, and T Yanagisawa. Development of the kek-b superconducting crab cavity. *11th European Particle Accelerator Conference*, page 5 p, 2008.

[32] K. Hosoyama, K. Hara, A. Kabe, Y. Kojima, Y. Morita, et al. Crab cavity development. *SRF 2005*, 2005.

[33] Y Funakoshi, T Abe, K Akai, M Akemoto, A Akiyama, M Arinaga, K Ebihara, K Egawa, A Enomoto, J Flanagan, S Fukuda, H Fukuma, K Furukawa, T Furuya, K Hara, T Higo, S Hiramatsu, H Hisamatsu, H Honma, T Honma, K Hosoyama, T Ieiri, N Iida, H Ikeda, M Ikeda, S Inagaki, S Isagawa, H Ishii, A Kabe, E Kadokura, T Kageyama, K Kakihara, E Kako, S Kamada, T Kamitani, K Kanazawa, H Katagiri, S Kato, T Kawamoto, S Kazakov, M Kikuchi, E Kikutani, K Kitagawa, H Koiso, Y Kojima, I Komada, T Kubo, K Kudo, N Kudo, K Marutsuka, M Masuzawa, S Matsumoto, T Matsumoto, S Michizono, K Mikawa, T Mimashi, S Mitsunobu, T Miura, K Mori, A Morita, Y Morita, H Nakai, H Nakajima, T T Na-

kamura, H Nakanishi, K Nakanishi, K Nakao, S Ninomiya, M Nishiwaki, Y Ogawa, K Ohmi, Y Ohnishi, S Ohsawa, Y Ohsawa, N Ohuchi, K Oide, M Ono, T Ozaki, E Perevedentsev, K Saitô, H Sakai, Y Sakamoto, M Satoh, M Sato, D N Shatilov, K Shibata, T Shidara, M Shirai, A Shirakawa, T Sueno, M Suetake, Y Suetsugu, R Sugahara, T Sugimura, T Suwada, T Tajima, S Takano, S Takasaki, T Takenaka, Y Takeuchi, M Tawada, M Tejima, M Tobiyama, N Tokuda, S Uehara, S Uno, Y Yamamoto, Y Yano, K Yokoyama, Ma Yoshida, Mi Yoshida, S Yoshimoto, and K Yoshino. Performance of kekb with crab cavities. In *EPAC08*, page 5 p, 2008.

[34] I Ben-Zvi, R Calaga, R Assmann, Oliver Sim Brüning, O Brunner, Edmond Ciapala, U Dorda, R Garoby, Jean-Pierre Koutchouk, T Linnecar, R Tomás, Joachim Tückmantel, Y Sun, F Zimmermann, T Peterson, N Solyak, V Yakovlev, B Rimmer, H Wang, K Hosoyama, N Kota, A Morita, Y Morita, K Oide, A Seryi, Z Li, L Xiao, G Burt, and P A McIntosh. Lhc crab cavities. Presentation, 2009.

[35] R. Calaga. Lhc crab cavities. Chamonix10, Jan 29, 2010.

[36] W. K. H. Panofsky and W. A. Wenzel. Some considerations concerning the transverse deflection of charged particles in radio frequency fields. *Review of Scientific Instruments*, 27(11):967, nov 1956. ISSN 0034-6748. doi: 10.1063/1.1715427.

[37] M.J. Browman. Using the panofsky-wenzel theorem in the analysis of radio-frequency deflectors. *Proceedings of the 1993 Particle Accelerator Conference,*, 2:800 – 802, 1993.

[38] *oai:cds.cern.ch:603056. CAS - CERN Accelerator School: Intermediate Course on Accelerator Physics*, Geneva, 2006. CERN, CERN.

[39] Yi-Peng Sun, Ralph Assmann, Javier Barranco, Rogelio Tomás, Thomas Weiler, Frank Zimmermann, Rama Calaga, and Akio Morita. Beam dy-

namics aspects of crab cavities in the cern large hadron collider. *Phys. Rev. ST Accel. Beams*, 12:101002, Oct 2009. doi: 10.1103/PhysRevSTAB.12.101002. URL `http://link.aps.org/doi/10.1103/PhysRevSTAB.12.101002`.

[40] H Padamsee. *Designing superconducting cavities for accelerators*. 2004.

[41] P. B. Wilson & H.A. Schwettman. Superconducting accelerators. *IEEE*.

[42] Giovanna Vandoni. Heat transfer. Presentation, 2004.

[43] Hasan Padamsee. *RF Superconductivity for Accelerators*. Jhon Wiley & sons, Inc., 1998.

[44] D. P. Pritzkau, G. B. Bowden, A. Menegat, and R. H. Siemann. Possible high power limitations from rf pulsed heating. In *American Institute of Physics Conference Series*, volume 474 of *American Institute of Physics Conference Series*, pages 387–398, May 1999. doi: 10.1063/1.59027.

[45] B Barwick, C Corder, J Strohaber, N Chandler-Smith, C Uiterwaal, and H Batelaan. Laser-induced ultrafast electron emission from a field emission tip. *New Journal of Physics*, 9(5):142, 2007. URL `http://stacks.iop.org/1367-2630/9/i=5/a=142`.

[46] *oai:cds.cern.ch:503603. CAS - CERN Accelerator School on Superconductivity and Cryogenics for Accelerators and Detectors*, Geneva, 2004. CERN, CERN.

[47] M Bahte, F Herrmann, and L N Lipatov. Magnetization and susceptibility measurements on niobium samples for cavity production. *Part. Accel.*, 60: 121–134, 1998.

[48] P. Bernard & H. Lengeler. New disk-loaded waveguides for the cern separator. *CERN 70-26*, 1970.

[49] C. Leeman & C. G. Yao. A highly effective deflecting structure. *Linear Accelerator conference*, 1990.

[50] E. Keil H. Lengler B.W. Montague & W.W. Neale P. Bramham, R.D. Fortune. Deflecting cavity design. *Phys. Letters*, 15:290, 1965.

[51] G.Burt. Rf deflecting mode cavities lecture ii issues and cavity designs. *RF for Accelerators CAS 2010*, 2010.

[52] H. Lengeler & V. Vaghin P. Bernard, P. Lazeyras. Particle separation with two and three cavity rf separators at cern. *CERN 68-29*, 1968.

[53] J. R. Aggus, W. Bauer, S. Giordano, H. Hahn, and H. J. Halama. Superconducting niobium deflectors. *Nuclear Science, IEEE Transactions on*, 20(3): 95 –97, june 1973. ISSN 0018-9499. doi: 10.1109/TNS.1973.4327051. URL `http://ieeexplore.ieee.org/stamp/stamp.jsp?tp=&arnumber=4327051`.

[54] A. Citron H. Schopper. Superconducting particle separator,. *Letter of intent to the Electronics experimental committee, CERN*, 1968. URL `http://cdsweb.cern.ch/record/1046302/files/CM-P00066155.pdf`.

[55] W. Bauer. Design study of a superconducting deflecting cavity. *IEEE Xplore*, 18:181–185, 1971.

[56] W. Bauer, A. Citron, G. Dammertz, H. C. Eschelbacherx, H. Lengeler, H. Miller, E. Rathgeber, and H. Diepers. Rf-tests on deflecting cavities for a superconductinig particle separator. *Nuclear Science, IEEE Transactions on*, 20(3):59 –62, june 1973. ISSN 0018-9499. doi: 10.1109/TNS.1973.4327043. URL `http://ieeexplore.ieee.org/stamp/stamp.jsp?tp=&arnumber=4327043`.

[57] W. Bauer, A. Citron, G. Dammertz, M. Grundner, L. Husson, H. Lengeler, and E. Rathgeber. Status of the cern-karlsruhe superconducting rf particle separator. *Nuclear Science, IEEE Transactions on*, 22(3):1144 –1147, june 1975. ISSN 0018-9499. doi: 10.1109/TNS.1975.4327831. URL `http://ieeexplore.ieee.org/stamp/stamp.jsp?tp=&arnumber=4327831`.

[58] S. Giordano H. Hahn H. J. Halama J. Aggus, W. Bauer. Experimental investigation of a superconduction niobium x-band deflecting cavity and suggestions for the design of the deflectors for a superconducting rf beam separator at nal. Technical report, Brookhaven National Laboratory, 1973.

[59] J. R. Aggus, W. Bauer, S. Giordano, H. Hahn, and H. J. Halama. Investigation of a superconducting niobium x x2010;band deflecting cavity. *Applied Physics Letters*, 24(3):144 –146, feb 1974. ISSN 0003-6951. doi: 10.1063/1.1655128. URL `http://www.osti.gov/bridge/servlets/purl/4419447-rIFrlS/4419447.pdf`.

[60] A. Krycuk. Construction of the cebaf rf separator. *PAC03*, 1993.

[61] D.M. Pozar. *Microwave Engineering*. Wiley, 2004. ISBN 9780471448785. URL `http://books.google.co.uk/books?id=4wzpQwAACAAJ`.

[62] P. Lorrain. *Electromagnetic Fields&waves 3e*. W.H. Freeman & Company, December 1987.

[63] J. R. Delayen & H. Wang. New compact tem-type deflecting and crabbing rf stucture. *Physical Review Special Topics- Accelorators and Beams*, 12, 2009.

[64] K. Hosoyama A. Kabe Y. Kojima Y. Morita, K. Hara. Vertical cold test of the crab cavity with a co-axial beam pipe. *SRF 01*.

[65] A.Honma A.Kabe Y.Kojima Y.Morita H.Nakai K.Nakanishi K.Akai K.Ebihara T.Furuya S.Mitsunobu M.Ono Y.Yamamoto K.Hosoyama, K.Hara. Construction and commisioning of kekb superconducting crab cavities. *Proceedings of SRF2007, Peking Univ., Beijing, China*, 2007. URL `http://accelconf.web.cern.ch/accelconf/srf2007/PAPERS/MO405.pdf`.

[66] A. Kabe K. Hosoyama, K. Hara. Superconducting crab cavity for kekb. *APAC 98*, .

[67] A. Kabe Y. Kojima K. Hosoyama, K. Hara. Fabricataion of a full scale crab cavity for kekb. *Proc 1997 workshop on RF superconductivity*, .

[68] ILAN BEN-ZVI. The quarter wave resonator as a crab cavity. LHC-CC10, 4th LHC Crab Cavity Workshop.

[69] J. R. Delayen. Compact superconducting cavities for deflecting and crabbing applications. In *Proceedings of SRF2011,*, 2011. URL `http://accelconf.web.cern.ch/accelconf/SRF2011/papers/thioa03.pdf`.

[70] G.Burt B.Hall D.R. Brett, R.B. Appleby. Particle trajectories in a 4 rod crab cavity.

[71] CST. Cst studio.

[72] Dassault Systemes. Solidworks.

[73] Erk Jensen Rama Calaga, Ed Ciapala. Crab cavities for the lhc luminosity upgrade. In *Proceedings of Chamonix 2012 workshop on LHC Performance*, 2012. URL `http://indico.cern.ch/getFile.py/access?contribId=6&resId=0&materialId=1&confId=103203`. Project Document, version 20Aug10.

[74] Richard G. Forbes. Some comments on models for field enhancement. *Ultramicroscopy*, 95:57–65, 2003.

[75] Dr. Erk Jensen (CERN) Rama Calaga (BNL). Field quality and nonlinearity of deflecting mode. Dec 2010. URL `http://indico.cern.ch/getFile.py/access?contribId=37&sessionId=8&resId=0&materialId=slides&confId=100672`.

[76] J Barranco Garcia, R Calaga, R De Maria, M Giovannozzi, A Grudiev, and R Tomás. Study of multipolar rf kicks from the main deflecting mode in compact crab cavities for lhc. oai:cds.cern.ch:1459579. Technical Report CERN-ATS-2012-120, CERN, Geneva, May 2012.

[77] Hans-H Braun. Basics of rf beam diagnostics lecture at the cockcroft institute. Presentation.

[78] L.C. Maier, Jr. and J.C. Slater. Field Strength Measurements in Resonant Cavities. *Journal of Applied Physics*, 23:68–77, January 1952. doi: 10.1063/1.1701980.

[79] Anton Labanc. Electrical axes of tesla-type cavities: Theoretical background, development of measurement equipment, measurement results. Technical Report DESY-TESLA-2008-01, DESY, Hamburg, Jan 2008.

[80] M. A. Furman and M. T. F. Pivi. Probabilistic model for the simulation of secondary electron emission. *Phys. Rev. ST Accel. Beams*, 5:124404, Dec 2002. doi: 10.1103/PhysRevSTAB.5.124404. URL `http://link.aps.org/doi/10.1103/PhysRevSTAB.5.124404`.

[81] G. Burt and A. C. Dexter. Prediction of multipactor in the iris region of rf deflecting mode cavities. *Phys. Rev. ST Accel. Beams*, 14:122002, Dec 2011. doi: 10.1103/PhysRevSTAB.14.122002. URL `http://link.aps.org/doi/10.1103/PhysRevSTAB.14.122002`.

[82] J.R.M. Vaughan. Multipactor. *Electron Devices, IEEE Transactions on*, 35(7): 1172 –1180, jul 1988. ISSN 0018-9383. doi: 10.1109/16.3387.

[83] P. T. Farnsworth. Television by electron image scanning. *J Franklin Inst.*, vol. 218:pp.: 411–444, 1934.

[84] A.C. Dexter B. Hall J.D.A. Smith Cockcroft Institute Lancaster UK P. Goudket STFC/DL/ASTeC Daresbury Warrington Cheshire UK G. Burt, R.G Carter. Benchmarking simulations of multipactor in rectangular waveguides using cst-particle studio. In *SRF2009*, 2009.

[85] P Yla-Oijala. Electron multipacting in tesla cavities and input couplers. *Part. Accel.*, 63:105–137, 1999.

[86] Y. Morita et.al. Multipacting in the crab cavity. *Proceedings of the 11th Workshop on RF Superconductivity, Lübeck/Travemünder,Germany*, 2003.

[87] W . Bauer. Fabrication of niobium cavities. srf 80, 1980.

[88] Private comunication with R. Calaga.

[89] R Calaga, S Belomestnykh, I Ben-Zvi, and Q Wu. A quarter wave design for crab crossing in the lhc. *Conf. Proc.*, C1205201(CERN-ATS-2012-115): WEPPC027. 3 p, May 2012.

[90] J. R. Delayen S. U. De Silva. Design and development of superconducting parallel-bar deflecting/crabbing cavities*. *Proceedings of IPAC2012, New Orleans, Louisiana, USA*, 2012.

[91] J. Delayen J. Grames A. Hutton G. Krafft R. Li L. Merminga M. Poelker B. Yunn Y. Zhang Jefferson Lab Newport News VA 23606 USA C. Montag Brookhaven National Laboratory Upton NY 11973 USA Ya. Derbenev, A. Bogacz. Elic at cebaf. *Proceedings of 2005 Particle Accelerator Conference, Knoxville, Tennessee*, 2005.

[92] G (CERN) et al Arduini. 5th lhc crab cavity workshop,. *LHC-CC11 Workshop Summary Report*, 2012.